2015

Electronic transport properties of carbon nanotubes: the impact of atomic charged impurities

Ryuichi Tsuchikawa
University of Central Florida

ELECTRONIC TRANSPORT PROPERTIES OF CARBON NANOTUBES: THE IMPACT OF ATOMIC CHARGED IMPURITIES

by

RYUICHI TSUCHIKAWA
Bachelor of Science in Physics, University of Central Florida, 2009

A dissertation submitted in partial fulfillment of the requirements
for the degree of Doctor of Philosophy
in the Department of Physics
in the College of Sciences
at the University of Central Florida
Orlando, Florida

Spring Term
2015

Major Professor: Masa Ishigami

ABSTRACT

Even changing one atom in nanoscale materials is expected to alter their properties due to their small physical sizes. Such sensitivity can be utilized to modify materials' properties from bottom up and is essential for the utility of nanoscale materials. As such, the impact of extrinsic atomic adsorbates was measured on pristine graphene and a network of carbon nanotubes using atomic hydrogen, cesium atoms, and dye molecules. In order to further quantify such an atomic influence, the resistance induced by a *single* potassium atom on metallic and semiconducting carbon nanotubes was measured for the first time. Carbon nanotubes are sensitive to adsorbates due to their high surface-to-volume ratio. The resistance arising from the presence of extrinsic impurity atoms depends on the types of nanotubes. *Metallic* carbon nanotubes are resilient to a long-ranged, Coulomb-like potential, whereas *semiconducting* carbon nanotubes are susceptible to these impurities. The difference in the scattering strength originates from the chirality of carbon nanotubes, which defines their unique electronic properties. This difference had not directly measured experimentally because of the issue of contact resistance, the difficulty of chirality identification, and the uncertainty in the number of impurity atoms introduced on carbon nanotubes.

We synthesized atomically clean, long (>100 μm) carbon nanotubes, and their chirality was identified by Rayleigh scattering spectroscopy. We introduced potassium atoms on the nanotubes to impose a long-range, Coulomb potential and measured the change in resistivity, excluding the contact resistance, by plotting the resistance as a function of the carbon nanotube length. The

flux of potassium atoms coming onto the nanotubes was monitored by quartz crystal microbalance, and the scattering strength of a single potassium atom was deduced from the change in resistivity and the density of potassium atoms on the nanotubes. We found that the scattering strength of potassium atoms on semiconducting nanotubes depends on the charge carrier type (holes or electrons). Metallic nanotubes were found to be less affected by the presence of potassium atoms than semiconducting nanotubes, but the scattering strength showed a large dependence on Fermi energy. These experimental results were compared to theoretical simulations, and we found a good agreement with the experiments. Our findings provide crucial information for the application of carbon nanotubes for electronic devices, such as transistors and sensors.

This thesis is dedicated to my parents
for their support on my academic journey

ACKNOWLEDGMENTS

First I would like to thank Dr. Masa Ishigami, Dr. Eduardo Mucciolo, Dr. Robert Peale, and Dr. Artem Masunov for being my dissertation committee members. My advisor Dr. Masa Ishigami introduced me to a frontier of graphene research when I joined his lab as an undergraduate student. As an advisor, he taught me not only how to carry out experiments but also how to take care of myself. He allowed me to take my time to understand physics and develop laboratory skills. I am glad and proud of myself for his giving me the carbon nanotube project. It was challenging, but I learned many things from the project. I thank him for having me as a research assistant for the most of my graduate study, and I feel privileged to take care of his cat, Mikan, whenever he goes out of town.

I also would like to thank Dr. Mucciolo for providing a great theoretical support in the nanotube project. His insight and knowledge in physics helped me understand physics in depth through discussion, as well as taking his classes. Dr. Peale and Dr. Masunov are kind enough to be my committee members. I appreciate Dr. Peale for being hard on me during my dissertation proposal and Dr. Masunov for teaching me a computational side of physics. I would like to thank Dr. James Hone at Columbia University for the supply of carbon nanotubes. I also thank the physics department stuff members for taking care of a lot of things outside the physic research.

Amin Ahmadi, Dr. Mucciolo's student, contributed a lot of theoretical work to this project. We always had good discussion on carbon nanotubes, along with some informal conversation on old Japanese cultures.

My fellow graduate students in the lab, Jyoti Katochi, Christian Smith, Mike Lodge, and Cameron Glasscock were good support for me. Especially Jyoti and her husband Simran were always available for support whenever I was stressed out. I always tried to scare her by sneaking up on her, but I only succeeded a few times (somehow she was able to sense my presence). Simran and I were always telling each other, "Go home!" since we were working a lot. Christian was good help especially for computer issues, which I am not good at. We are occasionally communicating in Japanese. Mike Lodge was actually in the same class when I was an undergraduate student. I thought he was a very quiet guy, but I was wrong. Our communication always starts with a Japanese joke of "Gets," and it still remains a big mystery why he wanted to turn my cell phone upside down. Cameron was helping me with machining things from time to time.

The undergraduate students in the lab, Daniel Heligman, Brandon Blue, and Qing Wang were a good support as well. Especially Daniel Heligman contributed a lot of his time to the device fabrication. Though he was calling me every five minutes for help, eventually he became more independent. I was able to rely on him for the delicate nanotube device fabrication. Brandon checked the grammatical things on my thesis, and Qing Wang was always a happy person in the lab to cheer me up when I was stressed out.

I thank Zhengyi Zhang at Columbia University for supplying carbon nanotubes and taking care of me when I stayed in New York city for one month to synthesize carbon nanotubes. The food we ate in the china town was excellent. She is a good cook and made lunch every day when she came down to UCF for two month to do her measurements.

I also thank my roommate Allen. His house is very nice and close to UCF. Moving to his house was a blessing to me, and I appreciated his spiritual influence. My discipleship group members at the church were also great spiritual support. Though it was hard to get up early in the morning every Tuesday, it was worth it, and I learned a lot about how to live as a follower of Jesus Christ. I especially thank Aubrey for his dedication to disciplining me. I also would like to thank Dave and Ted. They gave me an opportunity to reach out to international students.

I want to thank Jessica Machecek for encouraging each other and joking around on stupid things. I was able to make a balance between work and life. We need to go back to Knightro's again to be bloated.

Finally, I thank my parents. I feel bad that I did not talk to them as often as I should. Without their help, I would not be able to come to this point of academic achievement.

TABLE OF CONTENTS

LIST OF FIGURES

LIST OF TABLES

LIST OF ACRONYMS

AFM	Atomic force microscope
APS	ammonium persulfate
CNT	carbon nanotube
CVD	chemical vapor deposition
DCE	dichloroethane
DOS	density of states
hBN	hexagonal boron nitride
HF	hydrogen floride
HMDS	hexamethyldisilazane
IPA	isoprophylalcohol
KOH	potassium hydroxide
MIBK	methyl isobutyl ketone
MMA	methyl methacrylate
PDMS	polydimethylsilozane
PMMA	poly methyl methacrylate
QCM	quartz crystal microbalance
SEM	scanning electron microscope
STO	strontium titanate
UV	ultra violet

CHAPTER 1: INTRODUCTION

Carbon nanotubes were discovered for the first time in 1991 by Iijima with a transmission electron microscope [1]. This discovery was assisted by the research in carbon fibers. The discovery of C_{60} in 1985 [2] suggested researchers that the size of C_{60} be related to the narrowest carbon fibers, i.e., carbon nanotubes. Experimental realization of carbon nanotubes sparked a whole new field of research, and a vast amount of theoretical and experimental studies on carbon nanotubes have been reported since then. Even decades after the discovery, carbon nanotubes are still an active area of research, along with graphene, a two-dimensional sheet of graphite, found for the first time in 2004 by mechanically exfoliating graphite [3].

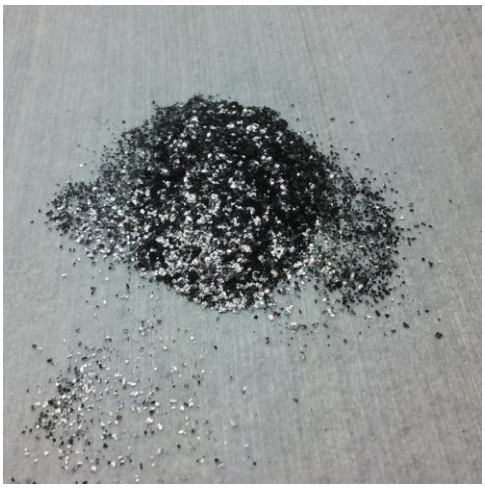

Figure 1.1: An image of graphite flakes. Graphite is made of a stack of graphene. Carbon nanotubes and C_{60} are conceptually constructed from graphene by forming a tubular shape and buckyball, respectively.

Various applications of carbon nanotubes have been realized [4] owing to their outstanding thermal [5, 6], electrical [7] conductivity, and elastic mechanical strength [8]. The electronic properties of carbon nanotubes especially have promising commercial applications for electronic devices: transparent and flexible transistors have been demonstrated using carbon nanotubes [9-11], and the techniques for a low-cost, print fabrication of these transistors were developed [12-14]. The high thermal conductivity of carbon nanotubes allows computers to dissipate heat efficiently [15], and the high current density makes it possible to use carbon nanotubes as an alternate material for efficient electric cables [16, 17]. Carbon nanotubes can also be used to add electrical conductivity to rubber [18] and extra mechanical strength to ceramic [19, 20] or cement [21]. Due to their nanoscale size, carbon nanotubes have been used for medical applications [22]. For example, non-invasive tracking of a blood flow in a brain [23] and artificial retinas [24] have been reported, utilizing the optical response of carbon nanotubes.

One of the important applications of carbon nanotubes is electronic sensors. Their mechanical robustness and high surface-to-volume ratio make carbon nanotubes ideal for sensors to detect gases, such as hydrogen [25, 26], oxygen [27], ammonia [28-30], carbon monoxide [31], nitrogen dioxide [32], and chemical vapors [33, 34]. The possibility of using nanotubes as pH sensors is also demonstrated [35-37]. The pressure sensors are another application of an unique combination of mechanical and electronic properties [38]. Carbon nanotubes are used for sensing bio-molecules, such as glucose [39, 40], tyramine [41], protein [42, 43], DNA [44-46], and viruses [47-49]. Carbon nanotube sensors are often functionalized by adding particles or molecules either covalently or non-covalently. The sensing mechanism is explained by a charge

transfer from an analyte into nanotubes, charge-carrier scattering on bio-molecules, Schottky effect, or defects in nanotubes [50, 51]. The detection time of these sensors is usually much faster than conventional optical methods, and the sensing level can be as good as a single bio-molecule detection [52, 53].

CHAPTER 2: ELECTRONIC PROPERTIES OF GRAPHENE AND CARBON NANOTUBES

2.1 Electronic properties of graphene

The electronic properties of carbon nanotubes are derived from their parental material – graphene. Carbon nanotubes are formed conceptually by rolling graphene into a tubular shape. For this reason, the electronic properties of graphene are discussed first. Those of carbon nanotubes are readily derived by applying a periodic boundary condition to graphene.

2.1.1 Hybridization of valence electrons in carbon atom

The Hamiltonian of an atomic carbon has eigenstates $|n,l,m\rangle$. Two of the six electrons in a carbon atom are in the *1s* state ($|1,0,0\rangle$) with the electron spin up and down. They are strongly bound to the atomic nucleus and do not participate in the formation of chemical bonds. The rest of the electrons are in the *2s* states ($|2,0,m\rangle$) and the *2p* states ($|2,1,m\rangle$). The linear combination of the eigenstates in the *2p* states forms an orthogonal basis in L^2 (angular momentum operator).

$$
\begin{aligned}
|p_x\rangle &= \tfrac{1}{\sqrt{2}}(|1,1,-1\rangle - |1,1,1\rangle) \\
|p_y\rangle &= \tfrac{i}{\sqrt{2}}(|1,1,-1\rangle + |1,1,1\rangle) \\
|p_z\rangle &= |1,1,0\rangle
\end{aligned}
\tag{2.1}
$$

The four valence electrons $2s$, $2p_x$, $2p_y$, $2p_z$, can be hybridized to create covalent bonds to neighboring carbon atoms in molecules and crystals. In a planar structure, $2s$, $2p_x$, and $2p_y$ have the same mirror symmetry and hybridize to form three sp^2 orbitals, as shown in Figure 2.1. Connecting the sp^2 orbitals between carbon atoms forms strong σ-bonds. The resulting two-dimensional sheet of carbon atoms has a honeycomb lattice structure, and it is called *graphene*. The remaining $2p_z$ orbitals at each carbon site in graphene form weak π-bonds. It is this π-bonds that are responsible for the electronic properties of graphene.

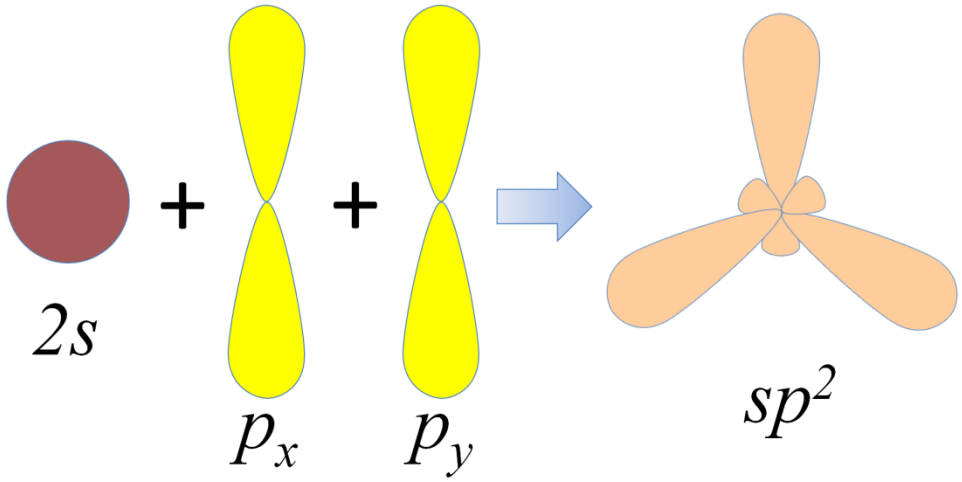

Figure 2.1: Schematic of sp^2 orbitals.

2.1.2 Unit cell and first Brillouin zone of graphene

The honeycomb structure is basically a two-dimensional, triangular Bravais lattice with a two-atom basis, i.e., there are two equivalent carbon atoms, *A* and *B*, in a unit cell. The lattice

constant is $a = \sqrt{3}a_{cc}$ = 0.246 nm, where a_{cc} = 0.146 nm is the carbon-to-carbon distance. The primitive vectors, $\boldsymbol{a}_1$ and $\boldsymbol{a}_2$, can be chosen as in Figure 2.2.

$$\boldsymbol{a}_1 = \left(\frac{\sqrt{3}a}{2}, \frac{a}{2}\right), \qquad \boldsymbol{a}_2 = \left(\frac{\sqrt{3}a}{2}, -\frac{a}{2}\right) \tag{2.2}$$

Then, using the condition, $\boldsymbol{a}_i \cdot \boldsymbol{b}_j = 2\pi\delta_{ij}$, the reciprocal vectors, $\boldsymbol{b}_1$ and $\boldsymbol{b}_2$, are defined as

$$\boldsymbol{b}_1 = \frac{2\pi}{a}\left(\frac{1}{\sqrt{3}}, 1\right), \qquad \boldsymbol{b}_2 = \frac{2\pi}{a}\left(\frac{1}{\sqrt{3}}, -1\right) \tag{2.3}$$

The first Brillouin zone forms a hexagonal shape with vertices located at $\frac{2\pi}{a}(0, \pm\frac{2}{3})$ and $\frac{2\pi}{a}(\pm\frac{1}{\sqrt{3}}, \pm\frac{1}{3})$.

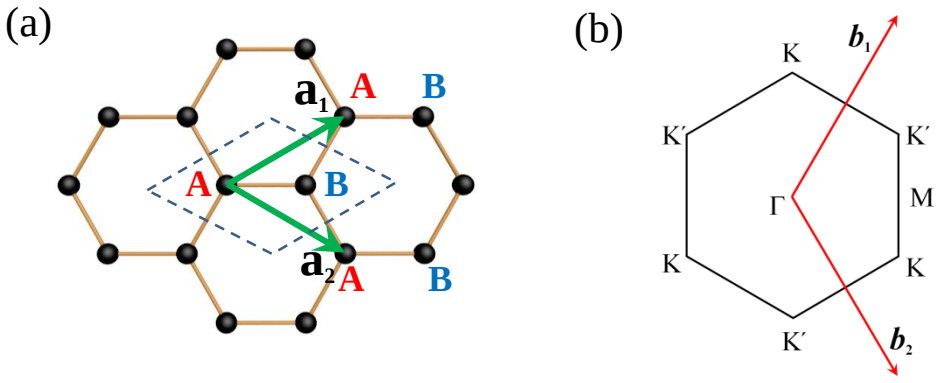

Figure 2.2: Primitive vectors and reciprocal vectors. (a) The area in the dashed line is a unit cell. (b) Reciprocal space. ***K*** and ***K'*** points are located at vertices of the hexagonal first Brillouin zone.

2.1.3 Tight-binding approximation

The electronic band structure of graphene is derived by tight-binding approximation. It assumes that the overlap of atomic wave functions between each atomic site is small. Thus, each atomic wave function satisfies the Schrödinger equation, $H_{atom}\Psi_n = E_n\Psi_n$, where *n* denotes the atomic orbitals. The periodic lattice or crystal Hamiltonian for a *single* electron is then

$$
\begin{aligned}
H &= \frac{\hbar^2}{2m_0}\nabla_{\boldsymbol{r}}^2 + \sum_i U_{atom}\,(\boldsymbol{r} - \boldsymbol{R}_i) \\
&= \left(-\frac{\hbar^2}{2m_0}\nabla_{\boldsymbol{r}}^2 + U_{atom}(\boldsymbol{r})\right) + \left(\sum_i U_{atom}(\boldsymbol{r} - \boldsymbol{R}_i) - U_{atom}(\boldsymbol{r})\right) \\
&= H_{atom} + \left(U_{periodic} - U_{atom}\right) \\
&= H_{atom} + \Delta U(\boldsymbol{r}), \qquad \Delta U(\boldsymbol{r}) < 0
\end{aligned}
\tag{2.4}
$$

where $U_{periodic}$ and U_{atom} are the periodic potential of the crystal and the potential of a single atom, respectively. The difference of the potentials, $\Delta U(\boldsymbol{r})$, is negative because the potential is attractive to electrons. This shows that the full crystal Hamiltonian can be constructed by adding a correction term, $\Delta U(\boldsymbol{r})$, to the atomic Hamiltonian. If the atomic wave functions are confined at each atomic site and do not leak to neighboring sites, they will all satisfy the full crystal Hamiltonian

$$
H\Psi_n(\boldsymbol{r} - \boldsymbol{R}_i) = E_n\Psi_n(\boldsymbol{r} - \boldsymbol{R}_i) \tag{2.5}
$$

where $\boldsymbol{R}_i$ represents the coordinates of each atomic site. Therefore, the *N* linear combination of these *degenerate* atomic orbitals is also the eigenstates of the full Hamiltonian. In order for this linear combination to satisfy Bloch condition of a periodic potential, it needs to be in the form (with normalization factor $1/\sqrt{N}$, where *N* is the number of atomic sites),

$$\Psi_{n\boldsymbol{k}}(\boldsymbol{r}) = \frac{1}{\sqrt{\mathrm{N}}}\sum_i \mathrm{e}^{i\boldsymbol{k}\cdot\boldsymbol{R}_i}\Psi_n(\boldsymbol{r}-\boldsymbol{R}_i) \implies |\Psi_n(\boldsymbol{k})\rangle = \frac{1}{\sqrt{N}}\sum_i \mathrm{e}^{i\boldsymbol{k}\cdot\boldsymbol{R}_i}\big|\varphi_{n,i}\rangle \qquad (2.6)$$

If, instead, atomic wave functions are allowed to leak slightly to nearest neighbor sites, i.e., both $\Delta U(\boldsymbol{r})$ and $\Psi_{\mathrm{n}}(\boldsymbol{r})$ are small but finite away from the atomic site, $\big|\varphi_{n,i}\rangle$ is no longer the eigenstates of the full Hamiltonian because the matrix elements, $\langle\varphi_{n,i\pm1}\big|H\big|\varphi_{n,i}\rangle = \langle\varphi_{n,i\pm1}\big|\Delta U_i\big|\varphi_{n,i}\rangle \equiv -\gamma, (\gamma > 0)$ is non-zero. However, the above *N* linear combination is still eigenstates of the full Hamiltonian in the basis set of atomic orbitals, $\big|\varphi_{n,i}\rangle$, and this leads to

$$\begin{aligned} H|\Psi_n(\boldsymbol{k})\rangle &= \frac{1}{\sqrt{N}}\sum_i e^{i\boldsymbol{k}\cdot\boldsymbol{R}_i}H\big|\varphi_{n,i}\rangle \\ &= \frac{1}{\sqrt{N}}\left[\sum_i E_n e^{i\boldsymbol{k}\cdot\boldsymbol{R}_i}\big|\varphi_{n,i}\rangle - \gamma e^{i\boldsymbol{k}\cdot\boldsymbol{R}_i}\big|\varphi_{n,i+1}\rangle - \gamma e^{i\boldsymbol{k}\cdot\boldsymbol{R}_i}\big|\varphi_{n,i-1}\rangle\right] \\ &= \left(E_n - \gamma e^{i\boldsymbol{k}\cdot(\boldsymbol{R}_{i+1}-\boldsymbol{R}_i)} - \gamma e^{i\boldsymbol{k}\cdot(\boldsymbol{R}_{i-1}-\boldsymbol{R}_i)}\right)|\Psi_n(\boldsymbol{k})\rangle \end{aligned} \qquad (2.7)$$

in the case of two nearest neighbor atoms.

For the case of graphene, there are two carbon atoms (*A* and *B*) in a unit cell. In order to calculate the π-bonds arising from the p_z orbitals, let the p_z orbital states at site *A* and *B* be $P_A(\boldsymbol{r} - \boldsymbol{r}_A)$ and $P_B(\boldsymbol{r} - \boldsymbol{r}_B)$. The orbital wave function in a unit cell is then the linear combination of the two wave functions at the sub-lattice *A* and *B*,

$$P(\boldsymbol{r}) = c_A P_A(\boldsymbol{r} - \boldsymbol{r}_A) + c_B P_B(\boldsymbol{r} - \boldsymbol{r}_B), \qquad |c_A|^2 + |c_B|^2 = 1 \tag{2.8}$$

The eigenstates of the full crystal Hamiltonian is now,

$$\Psi_{\boldsymbol{k}}(\boldsymbol{r}) = \frac{1}{\sqrt{N}} \sum_i e^{i\boldsymbol{k}\cdot\boldsymbol{R}_i} [c_A P_A(\boldsymbol{r} - \boldsymbol{r}_A - \boldsymbol{R}_i) + c_B P_B(\boldsymbol{r} - \boldsymbol{r}_B - \boldsymbol{R}_i)]$$

$$\equiv c_A \tilde{P}_A(\boldsymbol{k}, \boldsymbol{r}) + c_B \tilde{P}_B(\boldsymbol{k}, \boldsymbol{r})$$

$$\Longrightarrow \quad |\Psi(\boldsymbol{k})\rangle = c_A \left|\tilde{P}_A(\boldsymbol{k})\right\rangle + c_B \left|\tilde{P}_B(\boldsymbol{k})\right\rangle \tag{2.9}$$

The energy dispersion is found by calculating $\langle\Psi(\boldsymbol{k})|H|\Psi(\boldsymbol{k})\rangle = \varepsilon(\boldsymbol{k})\langle\Psi(\boldsymbol{k})|\Psi(\boldsymbol{k})\rangle$. For convenience, regard the states of the two sub-lattices at *A* and *B* as two bases. Then, the Hamiltonian can be written as a 2 × 2 matrix with its elements given by $H_{ij} = \left\langle \tilde{P}_i(\boldsymbol{k}) \middle| H \middle| \tilde{P}_j(\boldsymbol{k}) \right\rangle$, and the overlap matrix elements are given by $S_{ij} = \left\langle \tilde{P}_i(\boldsymbol{k}) \middle| \tilde{P}_j(\boldsymbol{k}) \right\rangle$. The energy dispersion, $\varepsilon(\boldsymbol{k})$, is found by solving the secular equation,

$$|H - \varepsilon(\boldsymbol{k})S| = 0 \tag{2.10}$$

Setting $H_{AA} = H_{BB} \equiv 0$ as an energy reference, and assuming that the overlap of atomic orbitals is negligible ($S_{AB} = S_{BA} = 0$), the equation (2.10) is reduced to be

$$\varepsilon(\boldsymbol{k}) = \pm\sqrt{|H_{AB}|^2} \tag{2.11}$$

Taking only the nearest-neighbor atoms, H_{AB} is evaluated as

$$\begin{aligned} H_{AB} = H_{AB}^* = \frac{1}{N}\Bigg[& \sum_{\boldsymbol{R}_i} \int d\boldsymbol{r}\, P_A^*(\boldsymbol{r} - \boldsymbol{r}_A - \boldsymbol{R}_i) H P_B(\boldsymbol{r} - \boldsymbol{r}_B - \boldsymbol{R}_i) \\ & + e^{i\boldsymbol{k}\cdot\boldsymbol{a}_1} \sum_{\boldsymbol{R}_i} \int d\boldsymbol{r}\, P_A^*(\boldsymbol{r} - \boldsymbol{r}_A - \boldsymbol{R}_i) H P_B(\boldsymbol{r} - \boldsymbol{r}_B - \boldsymbol{R}_i + \boldsymbol{a}_1) \\ & + e^{i\boldsymbol{k}\cdot\boldsymbol{a}_2} \sum_{\boldsymbol{R}_i} \int d\boldsymbol{r}\, P_A^*(\boldsymbol{r} - \boldsymbol{r}_A - \boldsymbol{R}_i) H P_B(\boldsymbol{r} - \boldsymbol{r}_B - \boldsymbol{R}_i + \boldsymbol{a}_2) \Bigg] \\ = & \int d\boldsymbol{r} P_A^*(\boldsymbol{r} - \boldsymbol{r}_A) H P_B(\boldsymbol{r} - \boldsymbol{r}_B) \\ & + e^{i\boldsymbol{k}\cdot\boldsymbol{a}_1} \sum_{\boldsymbol{R}_i} \int d\boldsymbol{r}\, P_A^*(\boldsymbol{r} - \boldsymbol{r}_A) H P_B(\boldsymbol{r} - \boldsymbol{r}_B + \boldsymbol{a}_1) \\ & + e^{i\boldsymbol{k}\cdot\boldsymbol{a}_2} \sum_{\boldsymbol{R}_i} \int d\boldsymbol{r}\, P_A^*(\boldsymbol{r} - \boldsymbol{r}_A) H P_B(\boldsymbol{r} - \boldsymbol{r}_B + \boldsymbol{a}_2) \Bigg] \\ = & -\gamma\left(1 + e^{i\boldsymbol{k}\cdot\boldsymbol{a}_1} + e^{i\boldsymbol{k}\cdot\boldsymbol{a}_2}\right) \end{aligned} \tag{2.12}$$

Here the transition amplitude or transfer energy between nearest neighbor atoms is defined as

$$-\gamma = \int d\boldsymbol{r} P_A^*(\boldsymbol{r} - \boldsymbol{r}_A) H P_B(\boldsymbol{r} - \boldsymbol{r}_B) = \int d\boldsymbol{r}\, P_A^*(\boldsymbol{r} - \boldsymbol{r}_A) H P_B\left(\boldsymbol{r} - \boldsymbol{r}_B + \boldsymbol{a}_{1,2}\right) \qquad (2.13)$$

The energy dispersion is then calculated to be

$$\varepsilon(\boldsymbol{k}) = \pm\sqrt{|H_{AB}|^2} = \pm\gamma\sqrt{3 + 2\cos\boldsymbol{k}\cdot\boldsymbol{a}_1 + 2\cos\boldsymbol{k}\cdot\boldsymbol{a}_2 + 2\cos\boldsymbol{k}\cdot(\boldsymbol{a}_2 - \boldsymbol{a}_1)}$$

$$= \pm\gamma\sqrt{1 + 4\cos\frac{\sqrt{3}k_x a}{2}\cos\frac{k_y a}{2} + 4\cos^2\frac{k_y a}{2}} \qquad (2.14)$$

This shows symmetric forms for holes and electrons, but this approximation is only valid near the Fermi energy. The symmetry breaks down at higher energy due to deviation from the approximation, i.e., a non-zero overlap matrix and the inclusion of second nearest neighbors.

The Hamiltonian can be simplified in the vicinity of $\boldsymbol{K}$ and $\boldsymbol{K}'$ point by the *k-p* approximation, which expands the wave function in the form of $\Psi_{k=K+q} = e^{i\boldsymbol{q}\cdot\boldsymbol{r}} u_{\boldsymbol{K}}(\boldsymbol{r})$ ($q \ll K$), with $u_{\boldsymbol{K}}(\boldsymbol{r})$ satisfying a Bloch equation. The Hamiltonian in this approximation becomes

$$H = \hbar v_F \begin{pmatrix} 0 & q_x - iq_y \\ q_x + iq_y & 0 \end{pmatrix} \qquad (2.15)$$

where $v_F = \frac{\sqrt{3}a\gamma}{2\hbar}$. Equation (2.15) is analogous to the Dirac Hamiltonian $\hbar v_F \boldsymbol{\sigma}\cdot\boldsymbol{k}$. The eigenstates of the Hamiltonian are given by spinors,

$$\begin{pmatrix} b_1 \\ b_2 \end{pmatrix} = \frac{1}{\sqrt{2}} \begin{pmatrix} \pm e^{-i\frac{\theta_q}{2}} \\ e^{\frac{i\theta_q}{2}} \end{pmatrix} \tag{2.16}$$

with $\theta_{\boldsymbol{q}} = \tan^{-1}\left(\frac{q_y}{q_x}\right)$, angle measured from *y*-axis, and the ± sign is for $E = \pm\hbar v_F|\boldsymbol{q}|$. The spinor eigenstates are called *pseudospins*, in contrast to physical spins. Pseudospins are coupled to the direction of propagation (either parallel or anti-parallel).

2.2 Energy dispersion of carbon nanotubes

The energy dispersion of carbon nanotube is obtained by applying a periodic boundary condition in the circumferential direction. The structure of carbon nanotubes is specified by the diameter of the tube and the chiral angle measured from zigzag direction. The chiral vector or *chirality* is defined as

$$\boldsymbol{C}_h = n\boldsymbol{a}_1 + m\boldsymbol{a}_2 \tag{2.17}$$

Carbon nanotubes are rolled up in the direction of the chiral vector, and the magnitude of the chiral vector is the circumference of the carbon nanotube. Therefore, the diameter of nanotube is

$$d = \frac{|\boldsymbol{C}_h|}{\pi} = \frac{a}{\pi}\sqrt{n^2 + nm + m^2} \tag{2.18}$$

The electronic band structure of carbon nanotubes is obtained by applying a periodic boundary condition on the circumference of nanotubes

$$\Psi_{\boldsymbol{k}}(\boldsymbol{r}+\boldsymbol{C}_h) = e^{i\boldsymbol{k}\cdot\boldsymbol{C}_h}\Psi_{\boldsymbol{k}}(\boldsymbol{r}) = \Psi_{\boldsymbol{k}}(\boldsymbol{r}) \tag{2.19}$$

This leads to the condition

$$\boldsymbol{k}\cdot\boldsymbol{C}_h = 2\pi j \quad \Longrightarrow \quad k_x\frac{\sqrt{3}a}{2}(n+m) + k_y\frac{a}{2}(n-m) = 2\pi j \tag{2.20}$$

where j is an integer. Substituting equation (2.20) into (2.14) gives a nanotube electronic band structure;

$$E_j^{\pm}(k) = \pm\gamma\sqrt{1+4\cos\left(\frac{2\pi j}{n+m}-\frac{n-m}{n+m}\frac{ka}{2}\right)\cos\left(\frac{ka}{2}\right)+4\cos^2\left(\frac{ka}{2}\right)} \tag{2.21}$$

In the vicinity of $\boldsymbol{K}$ point, $\boldsymbol{k} = \boldsymbol{K}+\boldsymbol{q} = (\boldsymbol{b}_1-\boldsymbol{b}_2)/3+\boldsymbol{q} = \left(q_x, 4\pi/3a+q_y\right)$, the boundary condition (2.19) becomes

$$e^{i\boldsymbol{q}\cdot\boldsymbol{C}_h}e^{i2\pi(n-m)/3}\Psi_{\boldsymbol{k}}(\boldsymbol{r}) = \Psi_{\boldsymbol{k}}(\boldsymbol{r}) \tag{2.22}$$

When the chirality satisfies the condition $n-m = 3l$ (l: integer), the boundary condition (2.22) is simplified to

$$e^{i\boldsymbol{q}\cdot\boldsymbol{C}_h}\Psi_{\boldsymbol{k}}(\boldsymbol{r}) = \Psi_{\boldsymbol{k}}(\boldsymbol{r}) \quad \Longrightarrow \quad \boldsymbol{q}\cdot\boldsymbol{C}_h = 2\pi j \tag{2.23}$$

with *j* an integer. In this case, the lowest-energy state is given by $j = 0$, passing through the Dirac point in the graphene energy dispersion. The conduction band and the valence band then touch at Fermi energy, forming *metallic* carbon nanotubes. The first sub-band of metallic nanotubes in the vicinity of the Dirac point is

$$E_{j=0}^{\pm}(q) = \pm\frac{\sqrt{3}a\gamma q}{2} \tag{2.24}$$

When $n - m = 3l \pm 1$, the boundary condition becomes

$$\boldsymbol{q}\cdot\boldsymbol{C}_h \pm \frac{2\pi}{3} = 2\pi j \implies q_\perp = \frac{2\pi}{|\boldsymbol{C}_h|}\left(j \pm \frac{1}{3}\right) \tag{2.25}$$

where $q_\perp$ is the wavevector in the circumferential direction. The energy dispersion then becomes

$$E_j^{\pm}(q_\parallel) = \pm\frac{\sqrt{3}a\gamma}{2}\sqrt{\left(\frac{2\pi}{|\boldsymbol{C}_h|}\right)^2\left(j \pm \frac{1}{3}\right)^2 + q_\parallel^2} \tag{2.26}$$

where $q_\parallel$ is a wavevector parallel to the tube axis. The energy in the equation (2.26) has a finite energy gap between conduction and valence bands, forming *semiconducting* carbon nanotubes. The boundary conditions for metallic and semiconducting nanotubes are shown in Figure 2.3.

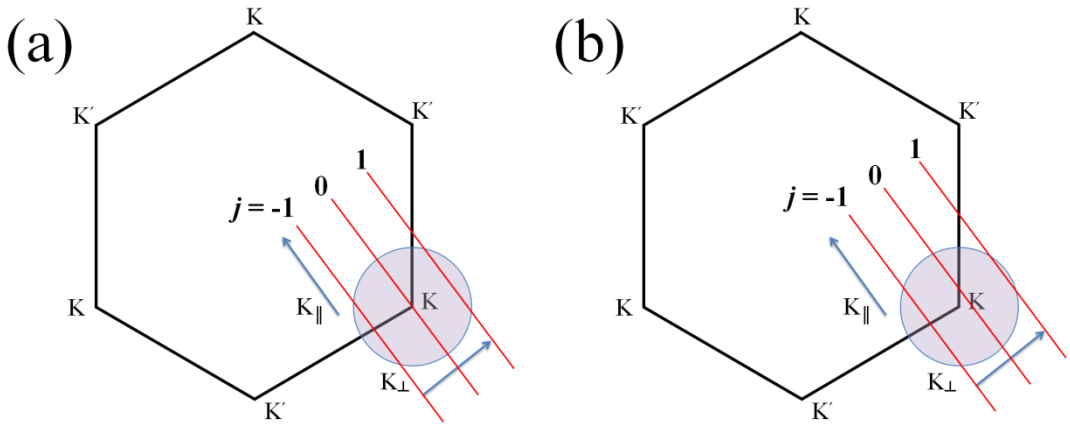

Figure 2.3: Quantized states in the reciprocal space of graphene from the boundary condition. The red lines represent the allowed states. (a) Metallic carbon nanotubs. $j = 0$ passes through the Dirac point. (b) Semiconducting nanotubes. $j = 0$ does not pass through the Dirac point, thus forming a band gap.

CHAPTER 3: SYNTHESIS AND CHARACTERIZATION OF GRAPHENE AND CARBON NANOTUBES

There are many different methods to make graphene and carbon nanotubes. High quality samples are usually limited to small quantity, and it is time consuming to produce them. Large quantity samples, on the other hand, can be produced quickly but contain atomic defects that degrade the quality of the samples. Since it is impossible to introduce every synthesis method, only selected synthesis methods are discussed in this chapter. The optical spectroscopy to characterize the quality of graphene and carbon nanotubes concludes this chapter.

3.1 Methods for monolayer graphene production

3.1.1 Mechanical exfoliation of graphene (adhesive tape method)

Mechanically exfoliating a piece of graphite with adhesive tape is the simplest method to produce monolayer graphene [3]. In this method, a small piece of graphite flake is placed on a strip of adhesive tape (Figure 3.1). The graphite is thinned down by repeating the process of attaching the tape to the graphite and peeling off a piece of graphite layers. Eventually, layers of thin graphite pieces, though not monolayer graphene yet, are formed on the tape. It is important to keep the freshly exfoliated surface of graphite from the tape adhesives during this process. The tape is then placed face down on a small substrate, and the non-adhesive side of the tape is rubbed with a pair of plastic tweezers. The tape is peeled off after rubbing the tape for

approximately 1 minute. The yield of monolayer graphene is low with this method, and our statistical study shows that the yield does not depend on the rubbing time, the number of exfoliation times, the peeling-off speed or peeling-off direction.

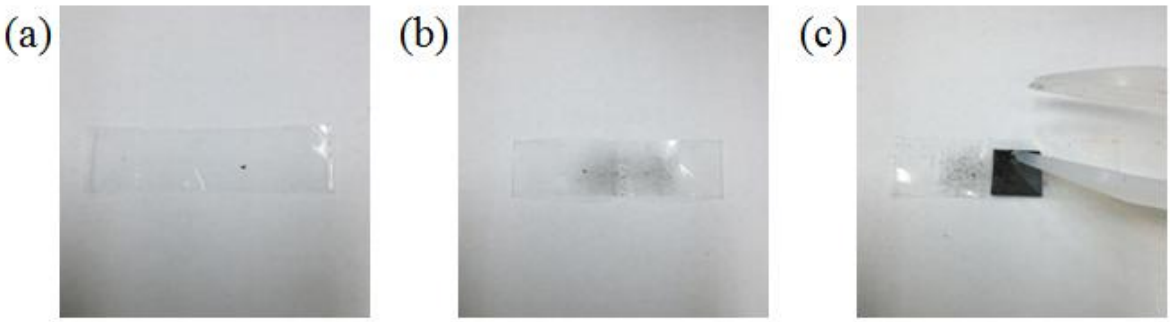

Figure 3.1: Graphene mechanical exfoliation process with adhesive tape. (a) A piece of graphite is placed on adhesive tape. (b) The graphite is exfoliated. Thinner graphite pieces spread in the middle of the tape. (c) The adhesive tape is placed face down on a substrate and is rubbed with a pair of plastic tweezers.

The target substrate is cleaved out of a doped silicon wafer with 280 nm thick of thermally grown oxide layer. The cleaved substrate must be prepared clean beforehand. The cleaning process is as follows: soak substrates in piranha solution (sulfuric acid : hydrogen peroxide = 3:1 by volume) for at least 10 minutes and place them in a bath of de-ionized water (DI water) for 5 minutes. Then, sonicate in isopropyl alcohol (IPA) for 1 minute to get rid of dust particles and blow-dry with compressed air or nitrogen gas.

Monolayer graphene can be found with an optical microscope. Typically, one finds many flakes of different colors on the surface as in Figure 3.2a. Yellow flakes are thick graphite, and the color changes to green, blue, purple, and pink as the graphite becomes thinner. This color change

is the result of the optical contrast imposed by the layer of 280 nm oxide. Pieces of undefined edges are adhesive residues from the tape. Gold markers are pre-patterned on the substrate for the purpose of recoding the graphene location. These gold markers are fabricated using electron beam lithography or photolithography, which is discussed in Chapter 4.

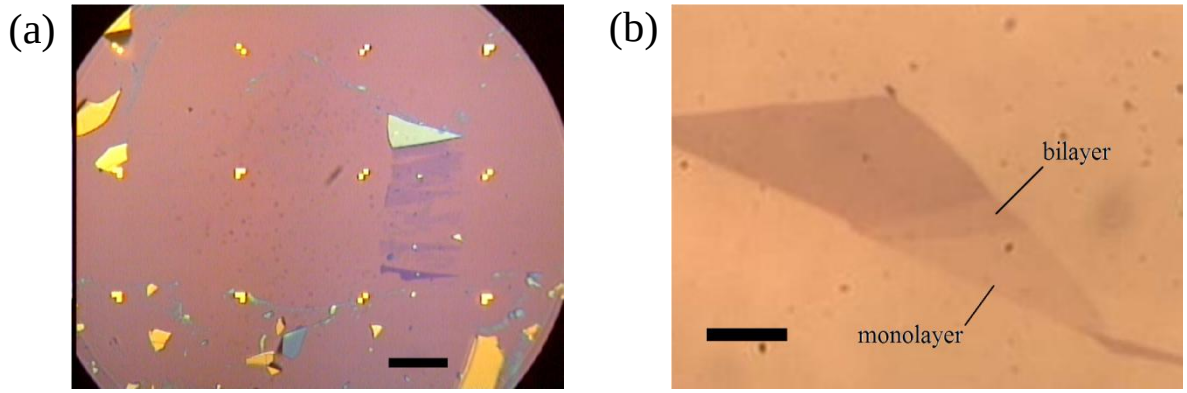

Figure 3.2: Optical images of graphene on a SiO_2/Si substrate with 280 nm of oxide layer. (a) Purple pieces are a few-layer graphene, and yellow and light green ones are thick graphite. Gold markers are present on the substrate for bookkeeping graphene locations. The scale bar is 30 μm. (b) Monolayer graphene attached to bilayer graphene. The scale bar is 10 μm. The bilayer graphene has slightly darker color.

Figure 3.2b is an optical image of monolayer graphene. Even though graphene is one-atom layer thick, it becomes visible because of the optical contrast. The best contrast is achieved when the thickness of the oxide layer is 280 nm. Substrates with different oxide thickness may not have sufficient optical contrast that human eyes can perceive. Monolayer graphene appears light pick on 280 nm of oxide layer, and bilayer graphene is slightly darker than monolayer graphene.

It is possible to distinguish monolayer graphene from bilayer graphene by the color, but the precise identification of the number of layers has to wait for Raman spectroscopy, which is

discussed in section 3.3.4. It is not recommended to rely solely on the color of graphene to identify the number of layers.

3.1.2 Mechanical exfoliation of graphene (non-adhesive tape method)

Monolayer of graphene can be exfoliated alternatively without adhesive tape if a razor blade and Kish graphite are used. Kish graphite is a large crystal of graphite and has more ordered stacking of layers in a larger size than regular graphite. Figure 3.3 shows the process of mechanical exfoliation by a razor blade. First, a very thin layer of Kish graphite is peeled off with a fine pair of tweezers. When placed, it sticks on a substrate. The thin layer of graphite needs to appear flat without having different domains, and it is crucial to have a clean surface on the substrate to make the thin graphite piece stick. Once the thin graphite is stuck, scratch it off with a razor blade. The most of the thin graphite is scratched off, but some pieces of graphite/graphene stay on the surface.

The advantage of this method is that the surface is devoid of adhesive residue, the size of graphene is larger, and the scratching process can be applied repeatedly until monolayer graphene is found. However, it is time consuming to stick thin graphite pieces, and graphene produced this way may be attached to a large piece of graphite. Moreover, there is a risk of scratching the oxide layer down to the doped silicon underneath, causing a gate leakage during the device fabrication.

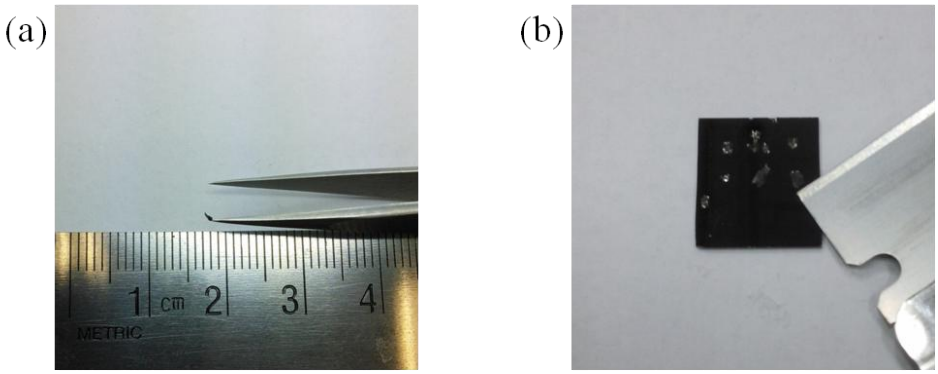

Figure 3.3: (a) Thin flake of graphite peeled off from Kish graphite at the tip of tweezers. (b) The thin flakes of graphite are stuck on a clean SiO_2/Si substrate. A razor blade is used to scratch off the graphite pieces.

Artificial bilayer graphene is created several times when a part of monolayer graphene is folded onto itself during the scratching process (Figure 3.4). Graphite has the Bernal AB stacking structure, where the second layer is rotated by 60 degrees. The stacking of this artificial bilayer graphene is, however, non-AB stacking, and interesting features are studied in Raman spectroscopy [55, 56].

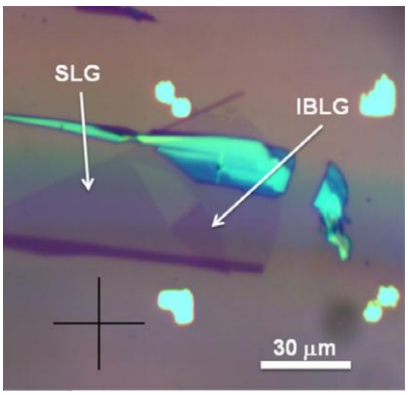

Figure 3.4: Folded bilayer graphene (incommensurate bilayer graphene).

3.1.3 Chemical vapor deposition (CVD)

Though mechanically produced graphene is clean and defect-free, it takes time and patience to find monolayer graphene. Furthermore, the size is small (10 μm × 10 μm at most), and the yield is low. For the fast, large-scale graphene production, chemical vapor deposition (CVD) method is routinely used in laboratories [57-59]. The CVD method is a bottom-up synthesis technique: the gas that contains carbon atoms, such as methane, is decomposed on a supporting metal film (usually copper) at elevated temperature, and graphene forms on the surface of the film.

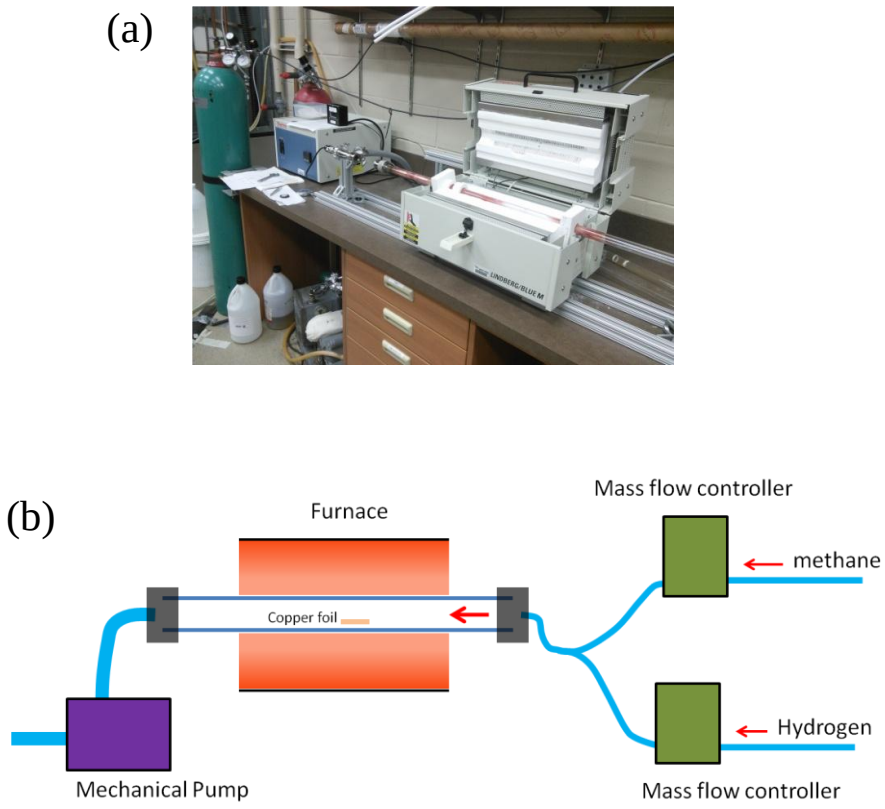

Figure 3.5: (a) CVD graphene synthesis setup. (b) Schematic of the synthesis setup. A flow of argon and hydrogen are mixed before they are flown into the furnace. The quartz tube is evacuated by a mechanical pump located down the stream.

Figure 3.5 shows the setup of CVD synthesis. Before the synthesis, a copper foil is flattened and treated with 5.4 wt% nitric acid for 90 seconds, followed by triple rinsing with DI water and blow-drying with nitrogen gas. The copper foil is placed in the middle of the quartz tube, and the tube is evacuated by a mechanical pump down to < 30 mTorr. A flow of 2 sccm hydrogen is then introduced into the quartz tube to keep the pressure at around 70 mTorr while pumping with the mechanical pump. The furnace is gradually heated up to 1050 °C at the rate of 20 °C /min. Once the temperature reaches 1050 °C, the copper foil is annealed for 1 hour to increase the domain size. To grow graphene, 25.4 sccm of methane is flown into the tube with the total pressure of 420 mTorr. After 45 minutes of synthesis, the methane flow is stopped, and the furnace is moved away from the copper foil for the rapid cooling.

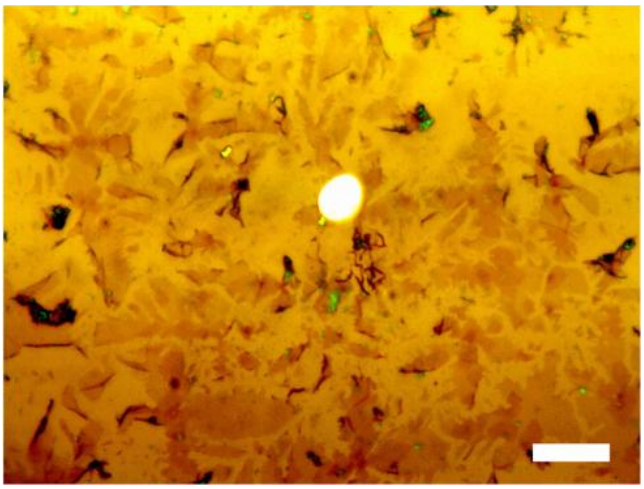

Figure 3.6: An optical image of CVD graphene. The scale bar is 10 μm. Multiple patches of small graphene are formed.

The CVD grown graphene is shown in Figure 3.6. The quality of CVD graphene is not as good as mechanically exfoliated graphene. The degradation of quality is related to the formation of

domains in graphene. Within each domain, crystal structure is maintained, but domains with different orientations are stitched together to form grain boundaries, at which large electrical resistance arises.

CVD grown graphene needs to be transferred from the copper support to a different substrate. Figure 3.7 shows this transfer process. First, the graphene-grown copper foil is spin-coated with 495 PMMA A4 at 5000 rpm and baked at 185 °C for 10 minutes. The same spin-coating process is repeated to have thicker PMMA film. The copper foil is wet-etched with 1 wt% ammonium persulfate (APS) solution overnight. The PMMA film floats on the solution when copper is dissolved. The floating PMMA film is transferred to a new APS solution to dissolve copper completely. After 2 hours, the film is placed on ultrapure water overnight to dilute the residual APS solution on the film. The film is transferred to new ultrapure water, and the floating PMMA/graphene is scooped out on a target substrate.

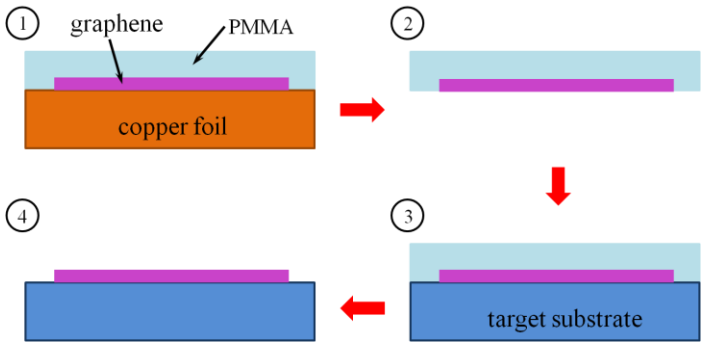

Figure 3.7: Schematic of the graphene transfer process. Copper is etched with an APS solution. It is necessary to dilute residual solution in order to have better graphene quality.

3.2 Growth of carbon nanotubes

Carbon nanotubes are routinely synthesized in many laboratories. The most common growth technique is a chemical vapor deposition (CVD) method. Carbon nanotubes grow from catalyst particles on a substrate in a flow of reaction gas(es) at elevated temperature. Three parameters i.e., catalyst, reaction gas, and growth temperature, need to be controlled in order to have optimal growth results. For instance, the diameter of carbon nanotube is correlated to the size of the catalyst particles, and the cleanliness of carbon nanotubes depends on the reaction gases and reaction temperature. In this section, three CVD growth techniques are discussed.

3.2.1 A network of carbon nanotubes (iron catalyst)

A network of carbon nanotubes grows when catalysts are deposited randomly on a substrate. The 150 μg/mL of a catalyst solution (iron particles) is prepared by dissolving ferric (III) nitrate nonahydrate in isopropyl alcohol [60]. The density of the nanotube network is determined by the concentration of the catalyst solution. A growth substrate (1 cm × 1 cm in size) is cleaved out from a doped silicon wafer with 500 nm of a thermally grown oxide layer. The clean substrate is then dipped in the catalyst solution for 10 seconds, rinsed in hexanes for 10 seconds, and blow-dried with nitrogen gas.

The growth setup is similar to that for CVD graphene synthesis, except for the mechanical pump. The growth substrate is placed in a quartz tube, and temperature is raised to 900 °C in 40 minutes in 1700 sccm of argon flow. Once 900 °C is reached, the temperature is kept at 900 °C for 10

minutes in the same flow of the gas. After 10 minutes of annealing, nanotubes are synthesized in a flow of hydrogen, methane, and ethylene (2000 sccm, 1300 sccm, and 60 sccm, respectively) in 10 minutes at the same temperature.

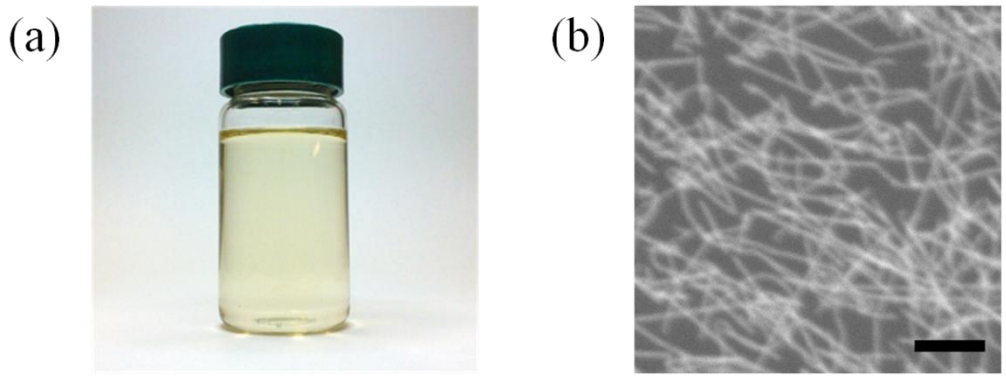

Figure 3.8: (a) Ferric (III) nitrate nonahydrate catalyst solution. (b) A SEM image of a network of carbon nanotubes. The scale bar is 10 μm. The acceleration voltage of the SEM is 1 kV.

The outcome of the growth is checked by a scanning electron microscope (SEM). Figure 3.8b shows an SEM image of a network of carbon nanotubes. Imaging just one carbon nanotube can be challenging, but it is easier to image a network of nanotubes because it behaves as a conducting film. The diameter of nanotube in SEM images appears an order of magnitude larger than the actual size. This is because the nanotube becomes visible by charging the substrate underneath the nanotubes.

3.2.2 Network of carbon nanotubes (cobalt catalyst)

Another method to grow a network of carbon nanotubes uses cobalt as a catalyst [61]. Figure 3.9 shows the setup of the synthesis. First, 0.5 nm thick of cobalt is deposited on a substrate by electron beam evaporation. The substrate is placed in a quartz tube and annealed in a flow of 520-sccm argon and 65-sccm hydrogen at 850 °C for 1 hour. For the synthesis, the same flow of gases is switched to bubble through ethanol in ice bath for 10 minutes. After the synthesis, the furnace is cooled down to room temperature in the original flow of argon and hydrogen without ethanol.

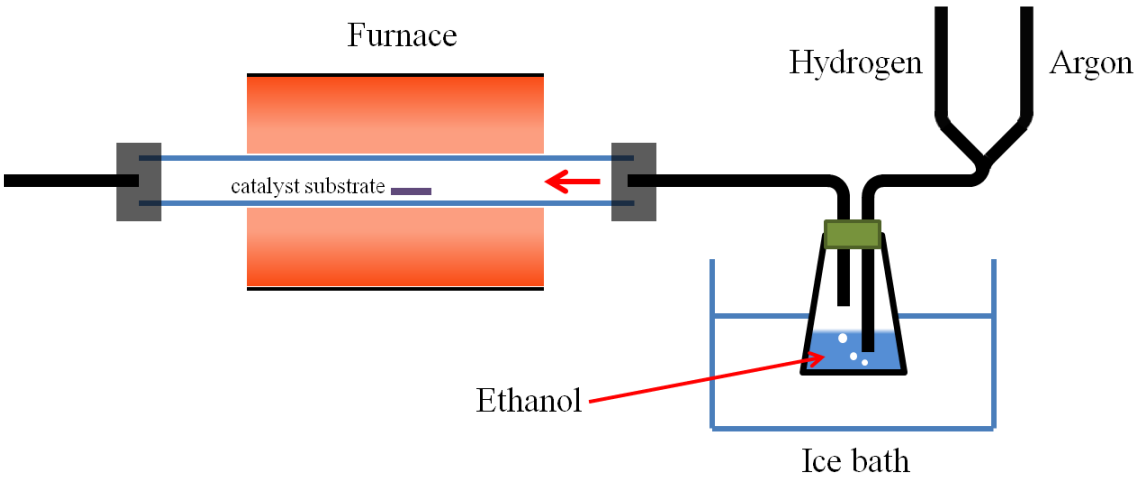

Figure 3.9: Schematic of synthesis setup for the cobalt-catalyst carbon nanotube growth. Ice bath is added to prevent the vaporization of ethanol. A flow of hydrogen and argon is bubbled through the ethanol.

3.2.3 Growth of single-walled carbon nanotubes

Compared to a network of carbon nanotubes, more sophisticated growth technique is required to grow individual single-walled carbon nanotubes [62, 63]. A mixture of molybdenum and cobalt is used as a catalyst [64], and a strip of the catalyst past is applied on a substrate [65]. Figure 3.10 shows the catalyst paste and the synthesis setup. The substrate is placed in the middle of the furnace and baked in the air at 400 °C for 30 minutes. Once it is cooled down, the air inside the quartz tube is evacuated with a mechanical pump for 30 minutes. After the evacuation, 200 sccm of Argon is flown through the tube at 1 atm to remove residual gases inside the tube.

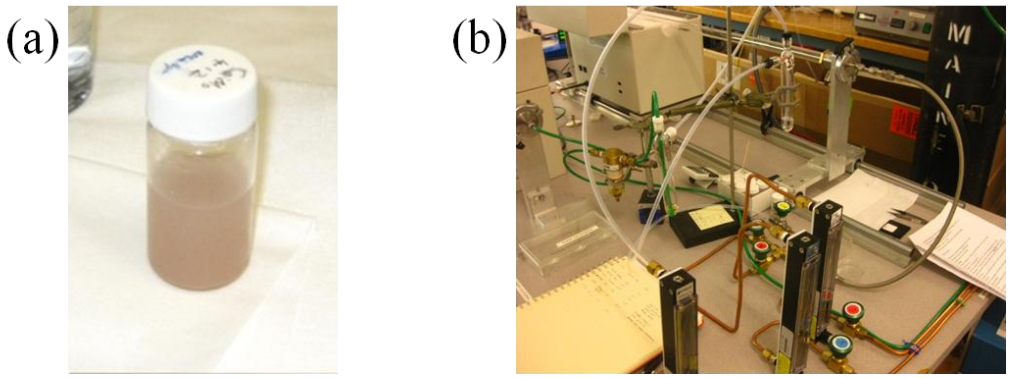

Figure 3.10: Single-walled carbon nanotube synthesis. (a) Catalyst solution/paste. (b) Synthesis setup.

A flow of 200-sccm hydrogen and 85-sccm argon mixture is then bubbled through ethanol and added to the first 200-sccm Argon flow. The furnace is slid away from the substrate to the downstream of the gas flow, and the temperature is set to 1000 °C. Once the temperature becomes stable at 1000 °C, the furnace is slid back quickly to the substrate position, and the furnace temperature is set to 900 °C. After 2–5 minutes, the ethanol supply is stopped while

hydrogen and argon are kept flowing to cool down the system to room temperature. In this method, carbon nanotubes grow in the direction of the gas flow, and it yields small diameter carbon nanotubes due to the small size of the nanoparticles.

Carbon nanotubes can also be grown suspended over a slit with this method. The suspension of carbon nanotubes makes it easier to identify the chirality of individual carbon nanotubes later by Rayleigh scattering spectroscopy (section 3.3.5). It also enables us to transfer the nanotubes to any substrate (section 4.3.1). The slit is made by a directional etching of <100> silicon with potassium hydroxide (KOH). Figure 3.11 shows optical images of growth chips. A silicon wafer is first passivated with a silicon nitride layer on both sides. Photolithography is performed to make small widows, and the passivation layer of silicon nitride is dry-etched, exposing the underlying silicon through the small windows. The silicon is then wet-etched through to the other side of the wafer with KOH. In order to make the transfer process easy, a raised platform is made. A protection layer is patterned over the etched side, and the surroundings are dry-etched by 20 μm. The whole silicon nitride passivation layer is then dry-etched. At the final step, a silicon oxide layer is thermally grown. The final chip has a raised platform in the middle of the chip with a slit in the center of the platform. This raised platform structure is important for a successful transfer of carbon nanotubes.

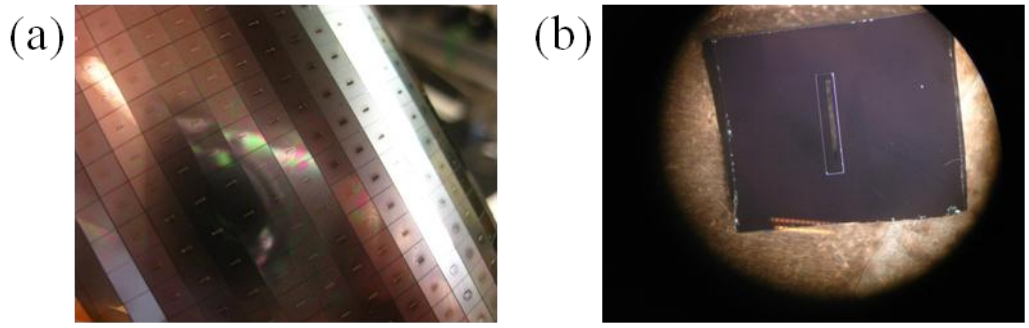

Figure 3.11: Optical images of growth chips with raised platforms. (a) Platform substrates made on a large-scale wafer. (b) An individual platform substrate. The open slit is located in the middle in the platform.

3.3 Optical characterization of graphene and single-walled carbon nanotubes

Even though monolayer graphene can be distinguished from bilayer graphene by the color, a scientific method to identify monolayer graphene is essential. Atomic force microscopy provides a way to measure thickness, but the step height from the thermally grown oxide to monolayer graphene is of questionable accuracy and consistency. In the case of single-walled carbon nanotubes, the identification of the chirality is important to know the exact band structure of the nanotubes. Optical spectroscopy probes to the intrinsic properties of a material and can be used to characterize the material. In this section, Raman spectroscopy and Rayleigh scattering spectroscopy are discussed for the identification of monolayer graphene and the chirality assignment of single-walled carbon nanotubes.

3.3.1 Rayleigh scattering and Raman scattering

Rayleigh scattering spectroscopy and Raman spectroscopy both measure the intensity of light scattering. When monochromatic light is incident on a material, it interacts with electrons in the material and induces dipole oscillations. If the dipole oscillations radiate back monochromatic light without loss of energy, the process is called Rayleigh scattering or elastic scattering. The process is called Raman scattering or inelastic scattering if the dipole oscillations interact with the vibration of atoms in the material (phonon) and radiate back monochromatic light with different energy from that of the incident light. Raman scattering is called Stoke (anti-Stoke) process when the inelastically scattered light has smaller (larger) energy. The term Raman scattering is specifically used for the inelastic scattering of light with optical phonons. The inelastic scattering involving acoustic phonons is termed Brillouin scattering. Rayleigh and Raman scattering both emit light, but this process is different from photoluminescence (Figure 3.12). In photoluminescence, electrons absorb the incident monochromatic light or photon and transit to different energy levels before the emission of light. Contrarily, the interacting electrons in the scattering process rather transit to virtual states, without absorption of photons. This intermediate virtual state does not need to be a real state, and Rayleigh and Raman scattering occurs at any wavelength of light. According to the perturbation theory, the virtual state is represented by a linear combination of eigenstates, and the energy uncertainty is large. Therefore, the life-time in the virtual state is very short, unless the virtual states are actual states (described in section 3.3.3). In Rayleigh scattering, the scattering process only goes through two steps: (1) the transition from the initial state to virtual states and (2) the transition from the virtual states to the initial state. Thus, the intensity of Rayleigh scattering is calculated by the

second-order perturbation. Raman scattering involves the extra interaction with phonon, and the intensity of Raman scattering is obtained from the third or fourth-order perturbation, leading to much smaller intensity in Raman than in Rayleigh scattering.

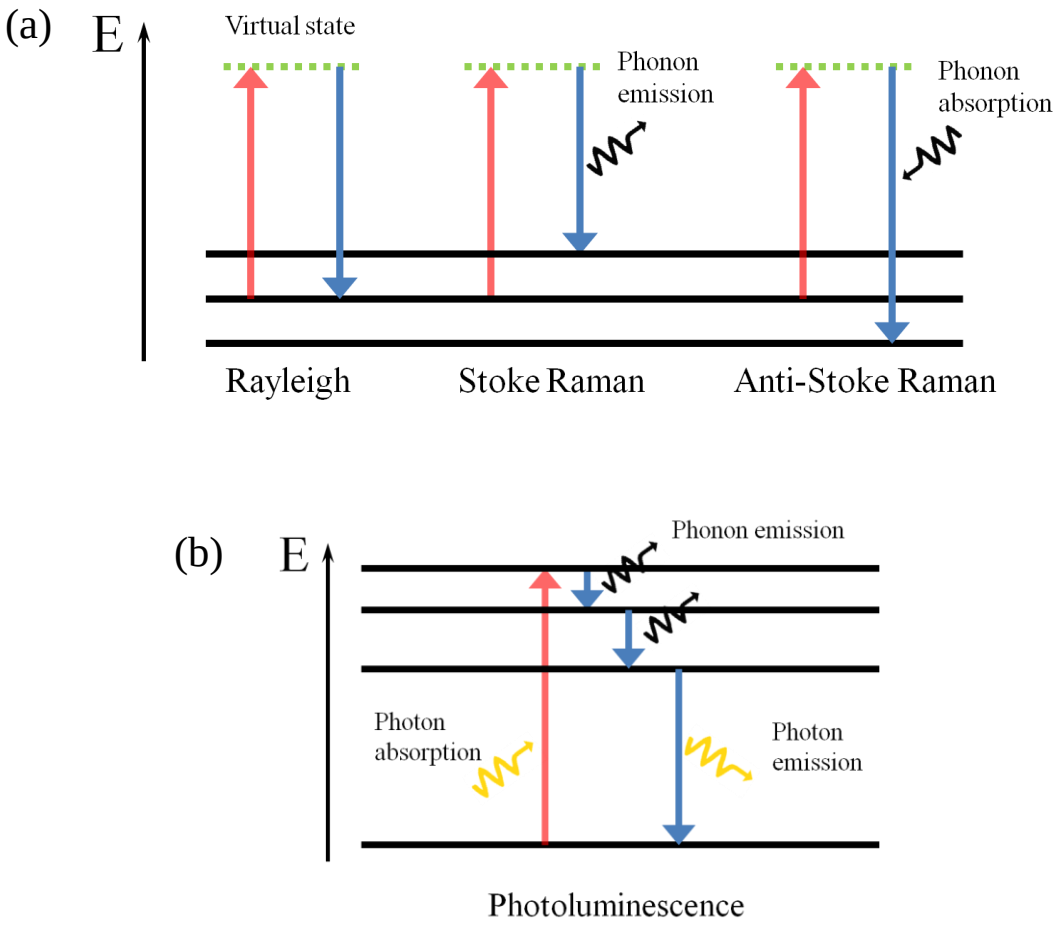

Figure 3.12: (a) Rayleigh scattering and Raman scattering. Both transit to a virtual state. (b) Photoluminescence. Absorbed light transits to an excited state. The excited electron loses its energy to lower energy states through interaction with phonons, and photon is emitted.

Rayleigh and Raman scattering are associated with the dielectric property or polarizability of constituting atoms in a material. The dipole moment is written as $P = \alpha E$, where α is polarizability and is expressed as

$$\alpha = \alpha_0 + \alpha_1 u \tag{3.1}$$

where u is the displacement of the core atom in a harmonic potential. The second term describes the strain-dependence of the polarizability. Describing the vibration of an atom as $u = \sin \omega_q t$, then the dipole moment is written as

$$\begin{aligned} \boldsymbol{P} &= \boldsymbol{E}_0(\alpha_0 + \alpha_1 \sin \omega_q t) \sin \omega_i t \\ &= \boldsymbol{E}_0 \left[\alpha_0 \sin(\omega_i t) + \frac{1}{2}\alpha_1 \cos(\omega_i - \omega_q)t - \frac{1}{2}\alpha_1 \cos(\omega_i + \omega_q)t\right] \end{aligned} \tag{3.2}$$

The first term, which comes from the zero-th order of polarizability is responsible for energy conserving Rayleigh scattering, and the last two terms are Stoke and anti-Stoke processes.

3.3.2 Gross selection rule

The energy and momentum must be conserved in the scattering process, and these conditions serve as a gross selection rule. The energy conservation is

$$E_{\text{i electron}} = E_{\text{f electron}} + E_{\text{photon/phonon}} \tag{3.3}$$

The momentum conservation with photon has a special condition: in Rayleigh and Raman spectroscopy, visible light is usually used, and the wavevector of visible light is much smaller than the size of Brillouin zone, satisfying the condition, $\boldsymbol{k}_{\text{photon}} << \boldsymbol{k}_{\text{BZ}}$. This leads to the momentum conservation,

$$\boldsymbol{k}_{\text{i electron}} = \boldsymbol{k}_{\text{f electron}} + \boldsymbol{k}_{\text{photon}} \approx \boldsymbol{k}_{\text{f electron}} \tag{3.4}$$

and the wavevector of electrons remains virtually the same after the photo-excitation. This condition, however, does not apply to the momentum conservation with phonons.

The momentum conservation is always satisfied in Rayleigh scattering because it does not exchange momentum with phonons. In Raman scattering, however, the conservation of momentum sets a restriction on the possible processes of Raman scattering. If one scattering event happens during Raman process (first-order Raman), the intermediate virtual state has momentum $\boldsymbol{k} \pm \boldsymbol{q}$ after the interaction with the phonon, where q is a phonon momentum. Since there is only one scattering event in the first-order Raman, there is no other momentum exchange to bring the momentum back to its original state. The only way to satisfy the momentum conservation in $\boldsymbol{k} = \boldsymbol{k} \pm \boldsymbol{q}$ is to set $\boldsymbol{q} = 0$. For this reason, the first-order Raman is associated with zone center phonons.

On the other hand, it is possible to have non-zero $\boldsymbol{q}$ if two scattering events occur (second-order Raman). The second-order Raman involves one phonon and another scattering process that has the opposite momentum $-\boldsymbol{q}$. The other scattering process can be either another phonon (two-

phonon, second-order Raman) or elastic scattering from defects (one-phonon, second-order Raman). The second-order process gives useful information about the phonon with non-zero momentum.

3.3.3 Resonance scattering

When virtual states correspond to real electronic states, resonance scattering occurs. The intensity of resonance scattering is much greater than non-resonance one. If the initial transition state is real, it is called incident resonance, and if the final transition state is real, it is called scattered resonance. In the second-order process, the resonance is called double resonance if the second transition state meets the resonance condition $E_{\text{gap}} = E_{\text{scattered photon}} + \hbar\omega_{\boldsymbol{q}}$. The double resonance has even stronger intensity than the single resonance. The resonance Rayleigh and Raman scatterings are responsible for the large-intensity signals from a nano-structured material like graphene and single-walled carbon nanotubes.

3.3.4 Raman spectroscopy on graphene

Figure 3.13 shows the Raman spectra of monolayer and bilayer graphene. The incident light wavelength is 514 nm (green). The two characteristic peaks in monolayer and bilayer graphene are G peak (1590 cm^{-1}) and 2D peak (2690 cm^{-1}). The G peak is the first-order resonance Raman with the zone center phonon. The 2D peak is the double resonance Raman scattering with two phonon exchanges over two valleys at $\boldsymbol{K}$ and $\boldsymbol{K}$'.

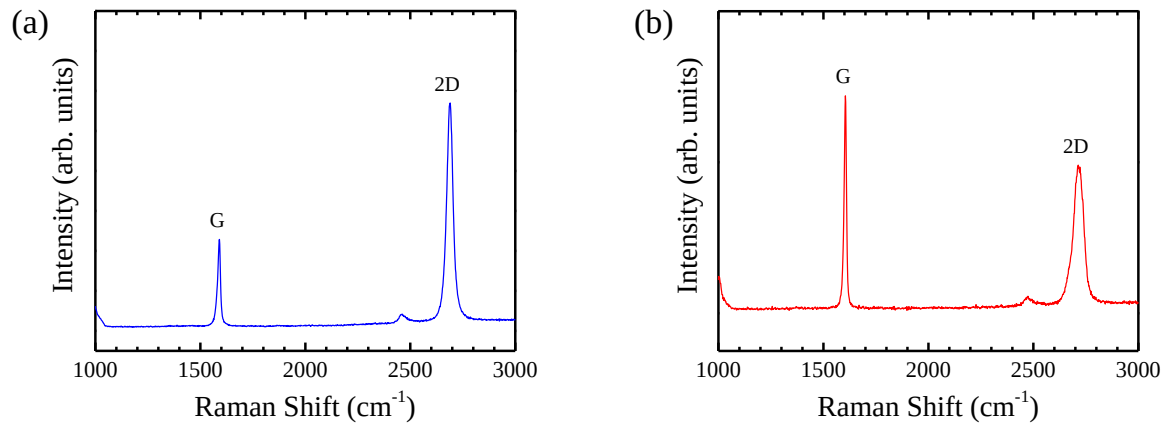

Figure 3.13: (a) Raman spectrum of monolayer graphene. The FWHM of the 2D peak is 32cm^{-1}. (b) Raman spectrum of bilayer graphene. The FWHM of 2D peak is 54cm^{-1}. The intensity ratio of 2D and G peaks changes depending on the number of graphene layers.

The number of the layers is determined by the spectral linewidth of the 2D peak [66]. The 2D peak of monolayer graphene has the FWHM of 25−30 cm^{-1}, while bilayer graphene has the FWHM of about 50 cm^{-1}. This 2D peak broadening in bilayer graphene is related to the electronic band structure of bilayer graphene: due to the interaction between layers, the electronic band splits in bilayer graphene, and phonon scattering with slightly different momentum occurs near the ***K*** and ***K***' point. The 2D peak broadening is large enough to distinguish monolayer graphene from bilayer graphene. The intensity ratio of 2D peak and G peak is also informative. The 2D peak intensity is larger than the G peak intensity in monolayer graphene, while in bilayer graphene, both 2D and G peaks have similar intensity.

Figure 3.14 shows the Raman spectra of CVD graphene. The FWHM is 54 cm^{-1}, and the intensity of 2D peak is smaller than that of G peak, indicating that the graphene is mostly bilayer.

Besides the 2D and G peak, D peak at 1373 cm^{-1}appears. The 2D peak is actually an overtone of this D peak, which is associated with the one-phonon, second-order double resonance Raman scattering. Instead of the two-phonon process as in the 2D overtone, the D peak involves elastic scattering from defects to bring the momentum back to the initial state (Figure 3.15). The D peak does not appear in defect-free, pristine graphene. The intensity of the D peak increases as the defect density increases. Thus, the presence of the D peak is a signature of defects in graphene.

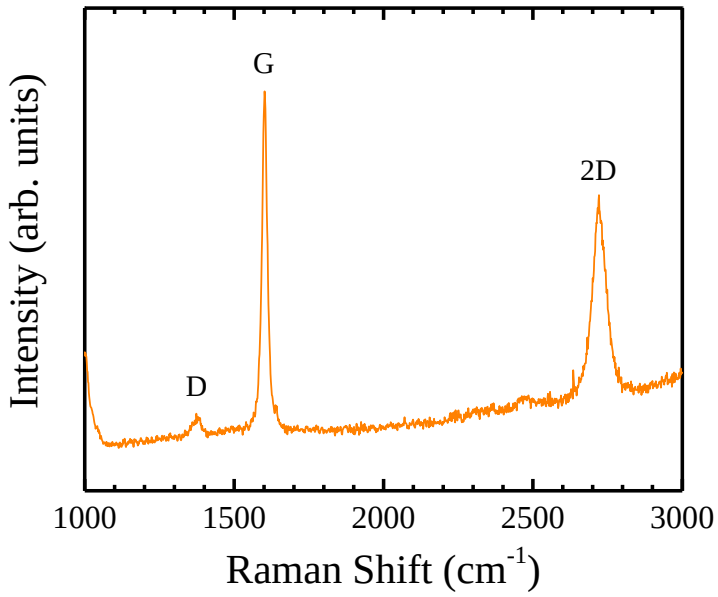

Figure 3.14: Raman spectrum of CVD graphene. It show an emerging D peak, which means there are defects in the graphene.

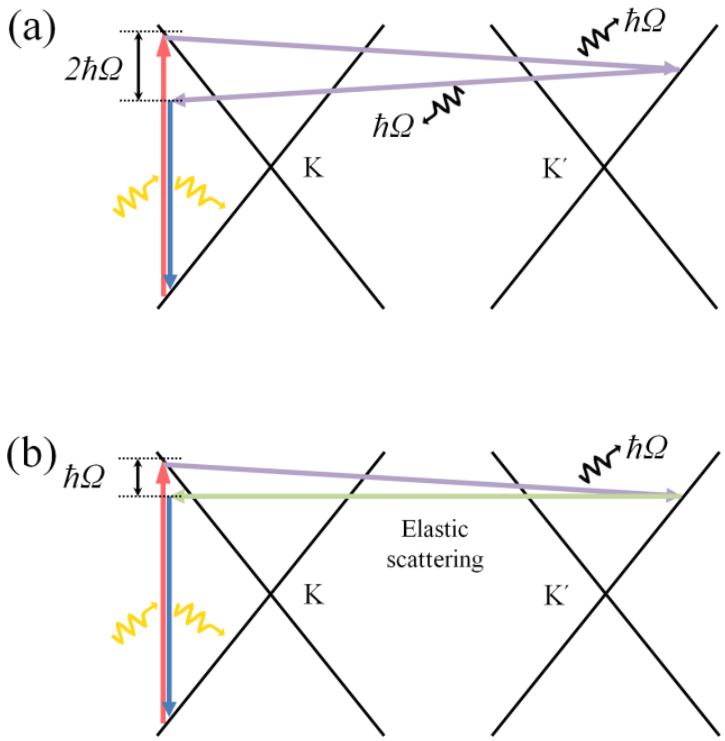

Figure 3.15: The mechanism of the double resonance Raman scattering responsible for (a) the 2D peak and (b) the D peak in graphene Raman spectra. The 2D peak involves the two-phonon process, and the D peak involves one phonon and one defect scattering. The energy loss of the two-phonon process is twice as large as that of the one-phonon process. The D peak does not show up in the Raman spectra without defects in graphene.

3.3.5 Rayleigh scattering spectroscopy of single-walled carbon nanotubes

The chirality assignment of single-walled carbon nanotubes with Raman spectroscopy is not as easy as the identification of monolayer graphene. Raman spectroscopy probes to the radial breathing mode (RBM) of phonon that is related to the diameter of carbon nanotubes, but it is difficult to completely indentify the chirality (n,m) with the information on phonon. The resonance Rayleigh scattering spectroscopy, which probes to electronic transition energy [67, 68], is more advantageous over Raman spectroscopy because the chirality of nanotubes uniquely

defines the electronic band structure. Rayleigh scattering occurs in a broad range of wavelength, but it shows prominent peaks when incident photon energy is in resonance with the electronic transition energy in carbon nanotubes. Applying Rayleigh scattering spectroscopy to carbon nanotubes is, however, challenging when the nanotubes are on a substrate. The signal intensity is weak due to the size of the nanotube, and the noise from the substrate makes it harder to accurately determine the spectra. This problem is solved by suspending carbon nanotubes as described in section 3.2.3.

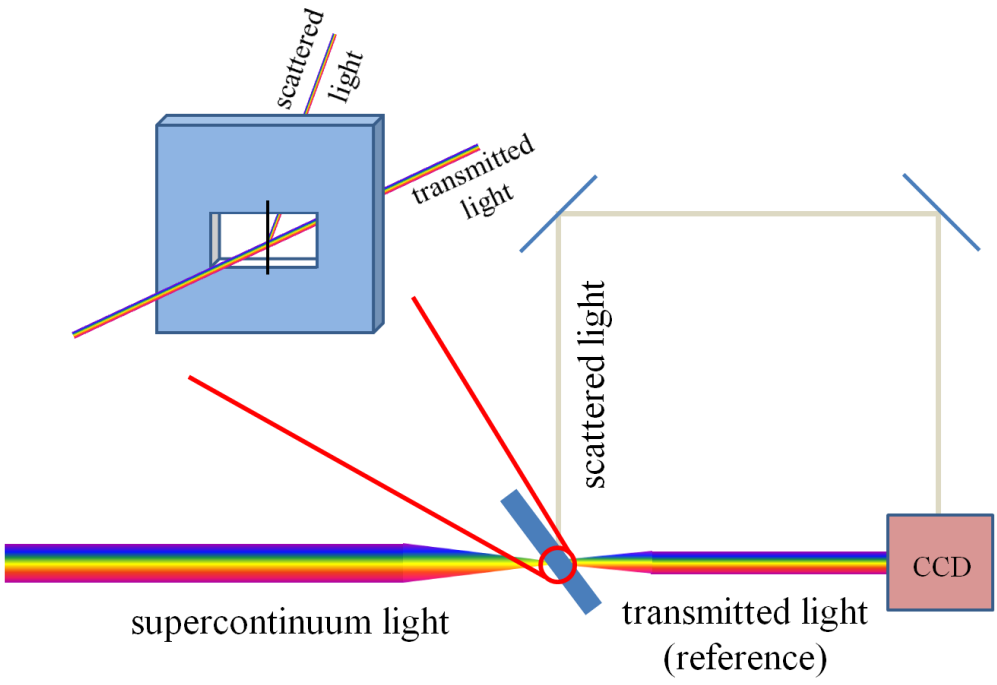

Figure 3.16: The schematic of Rayleigh scattering spectroscopy of suspended single-walled carbon nanotubes. Incident light is supercontinuum light. Most of the light transmits without scattering, which is used as a reference for the spectra. The scattered light is collected in a different optical path, and it is compared to the reference.

The principle setup of Rayleigh scattering spectroscopy is shown in Figure 3.16. For the fast data collection in broad band, a supercontinuum light source is used for the incident light, and the scattered light is detected in the direction off the line of transmitting light [67]. The suspended nanotubes are easily spotted with an optical lens as the incident light scatters off the nanotube. The location of the nanotube is recorded with the position reading on the micromanipulator.

Figure 3.17 shows a spectrum of Rayleigh scattering spectroscopy of a single-walled carbon nanotube. These energy peaks correspond to the electronic transition energy of a carbon nanotube. One can refer to Kataura plot to assign a chirality (n,m) [69]. If the spectrum shows multiple peaks, it is likely to be bundled nanotubes (Figure 3.18).

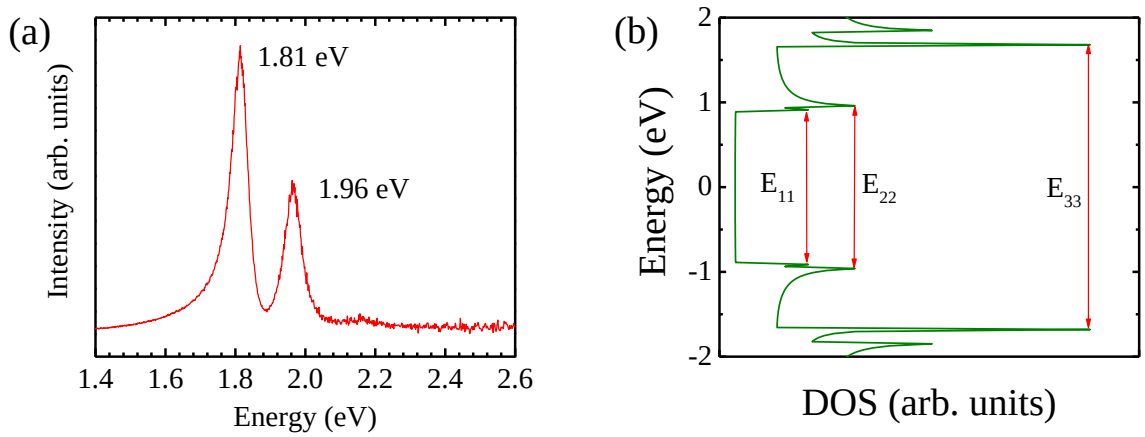

Figure 3.17: (a) A Rayleigh scattering spectrum of a (13,7) metallic nanotube. (b) DOS of a (13,7) nanotube obtained from the equation (2.21) with γ = 3.0 eV. E_{11} = 1.82 eV, E_{22} = 1.92 eV, and E_{33} = 3.36 eV.

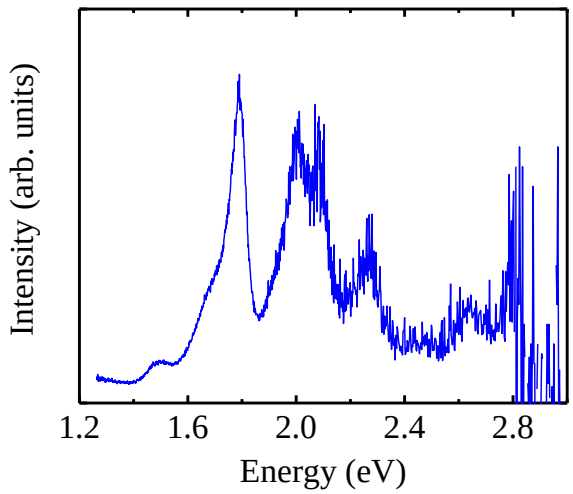

Figure 3.18: A Rayleigh scattering spectrum of bundled carbon nanotubes. Multiple peaks are present in the spectrum.

CHAPTER 4: DEVICE FABRICATION

4.1 Graphene electronic device fabrication

Graphene devices are usually fabricated in a four-probe configuration, in which, constant current is passed from a source electrode to drain electrode, and the voltage drop across the other two probes is measured (Figure 4.1). The four-probe configuration is often used for materials with small resistance, like graphene, and is advantageous over the source-drain, two-probe configuration because the contact resistance does not interfere with the measurement, and the extra probes can also be used to measure Hall effect. In this section, the device fabrication process of graphene on SiO_2 and strontium titanate is discussed.

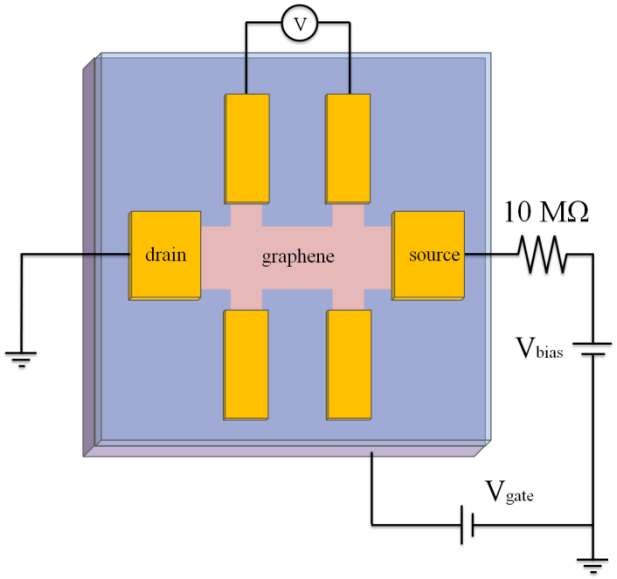

Figure 4.1: A four-probe configuration for a graphene device. A resistor with large resistance is connected in series with graphene so that virtually constant current passes through the graphene. The extra probes measure the voltage drop in the graphene channel.

4.1.1 Graphene device on SiO_2

Once graphene is found on a SiO_2/Si substrate, as described in section 3.1, an undercut layer of MMA is spin-coated at 6000 rpm and baked at 180 °C for 5 minutes. PMMA A4 is spin-coated on the top of MMA layer at 6000 rpm and also baked at 180 °C for 5 minutes. Graphene may be lost or rolled up during the spin-coating process if it is not adhered well to the oxide layer. Electron beam lithography is performed with an electron dosage of 350 $\mu C/cm^2$ for small features (a few microns in width) and 400 $\mu C/cm^2$ for larger features. These values may need to be adjusted depending on the type and thickness of PMMA and MMA layers. The device design requires extra caution so that no electrodes go across scratches on the surface of the substrate. These scratches form a short circuit between the electrode and backgate (the doped silicon underneath the oxide layer).

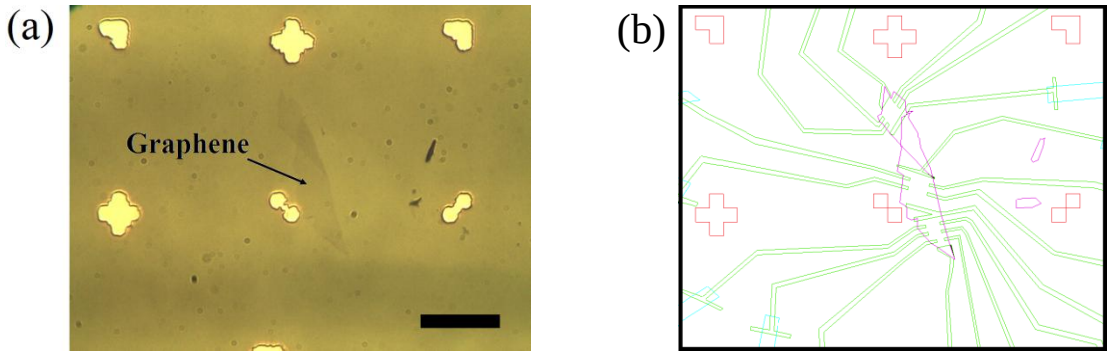

Figure 4.2: Graphene and device design. (a) Mechanically exfoliated graphene on a SiO_2/Si substrate. The scale bar is 30 μm. (b) A device design. Gold markers are used for the alignment of the design to the graphene during the electron beam lithography.

The pattern is developed in a mixture of MIBK and IPA solution with 1 to 3 volume ratio for 1 minute at room temperature after the electron beam lithography. Then, 3 nm of chromium and 80

nm of gold are deposited in a thermal evaporation chamber. Chromium is used as an adhesion layer to the oxide since gold does not readily stick to SiO_2. The excess Cr/Au film is lifted-off in Remover PG or acetone. This lift-off process needs to be gentle enough not to roll up the graphene. Another electron beam lithography patterning may be needed to selectively etch off excess pieces of graphene with oxygen plasma.

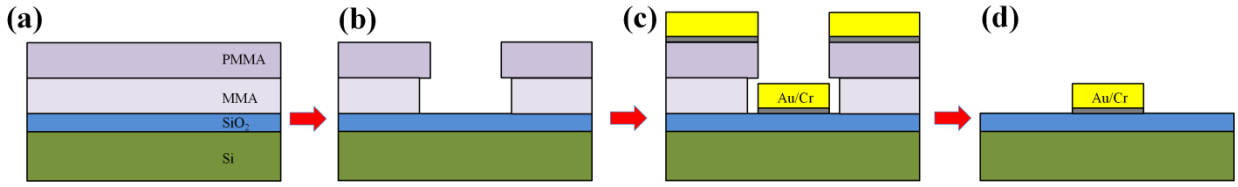

Figure 4.3: Schematic of Electron beam lithography. (a) Layers of PMMA and MMA are spin-coated on a SiO_2/Si substrate. (b) Pattern is made with electron beam lithography and subsequent development in MIBK/ IPA solution. (c) Cr and Au are deposited. (d) Polymer layer and its attached excess metal film are removed in Remover PG or acetone.

The graphene device after the lift-off process has some polymer residue left on it. Annealing under a flow of Ar (800 sccm) and H_2 (900 sccm) at 400 °C for 3 hours removes the residue effectively and leads to atomically clean graphene devices.

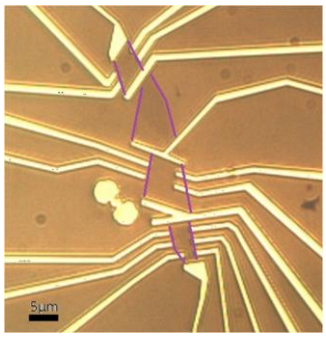

Figure 4.4: An optical image of a graphene device.

4.1.2 Graphene device on strontium titanate

Graphene devices can be made on different substrates by following the same device fabrication procedure described in the previous section. A substrate with large dielectric constant is of particular interest due to its gating efficiency and dielectric screening of charged impurities. Strontium titanate (STO) has a dielectric constant of 330 at room temperature, roughly 80 times larger than that of SiO_2, and it increases to >20,000 at 10K [70]. However, monolayer graphene has poor optical contrast on STO substrates, and it is a formidable task to search for monolayer graphene on STO. Instead of finding monolayer graphene, graphene can be *transferred* from a SiO_2 substrate onto a STO substrate.

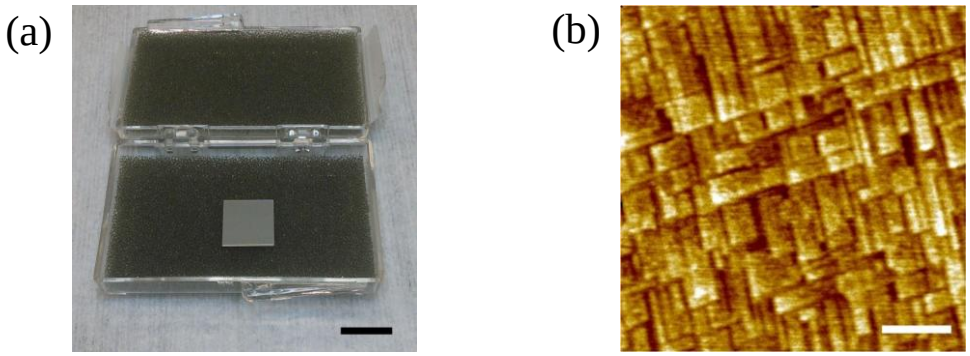

Figure 4.5: (a) An STO crystal. The crystal orientation is <100>. The scale bar is 1 cm. (b) An AFM image of the surface of a STO crystal. The scale bar is 200 nm.

The transfer process begins with finding monolayer graphene on a SiO_2/Si substrate, as described in section 3.1.1 or 3.1.2. After the number of layers is confirmed with Raman spectroscopy, the substrate is spin-coated with PMMA A4 at 6000 rpm and baked at 170 °C for 5 minutes. Optical images of the graphene and surrounding features (graphite flakes, etc.) are captured after the

spin-coating process. These images are used later as a reference to locate graphene on a STO substrate. One of the corners on the PMMA film is scratched to expose the SiO_2 so as to quicken the etching process. The substrate is then submerged into a hydrogen fluoride (HF) solution and begins to etch off the silicon oxide layer underneath the PMMA film. This etching process may take up to one day to complete. Once the etching is complete, the PMMA film detaches and floats on the HF solution with graphene stuck to the underside of the film. The floating film is transferred to DI water to dilute the residual HF solution on the film, and then scooped out onto the target substrate. This target substrate can be another SiO_2/Si substrate, STO or any other substrates of interest. The target substrate and transferred film are then baked at 90 °C on a hot plate to dry the film. Finally, the PMMA film is dissolved in acetone.

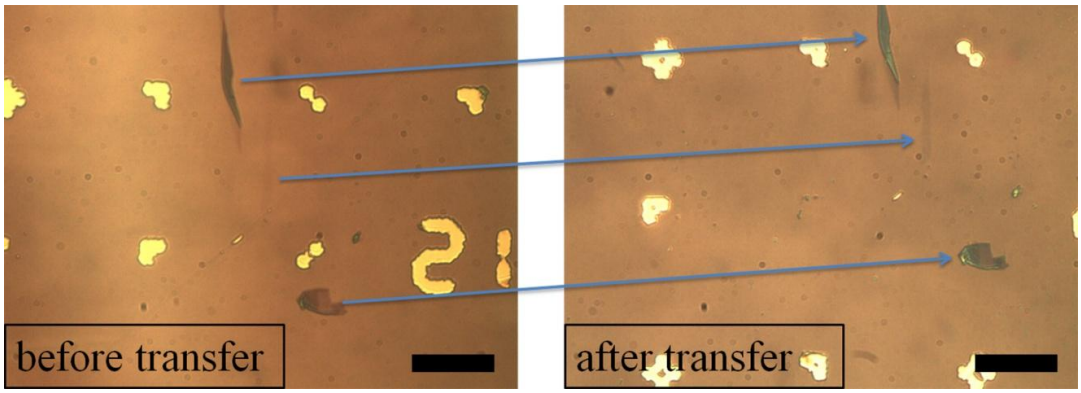

Figure 4.6: Graphene transferred onto another SiO_2/Si substrate. The scale bar is 30 μm.

Other graphite flakes around the graphene are also transferred during this process, and they maintain their relative distance to one another, as shown in Figure 4.6 (the target substrate here being SiO_2/Si). These thicker graphite flakes are visible on a STO substrate and can be used as a reference to locate graphene, though it is very hard to see on STO. Optical filters may help make

graphene visible. The presence of the transferred graphene can be further confirmed by AFM if necessary.

The STO substrate is annealed in air at 1100 °C for 4 hours prior to the transfer. This annealing treatment changes the surface morphology of STO, and it becomes more ordered as shown in Figure 4.7. The annealing needs to be done with the presence of oxygen, otherwise oxygen atoms would be removed from the crystal during the annealing process. STO cannot be cleaned with a piranha solution as in the case of graphene on a SiO_2/Si substrate as the piranha solution etches the surface of STO as shown in Figure 4.8. This selective etching of the surface happens because of dislocations of the crystal on the surface.

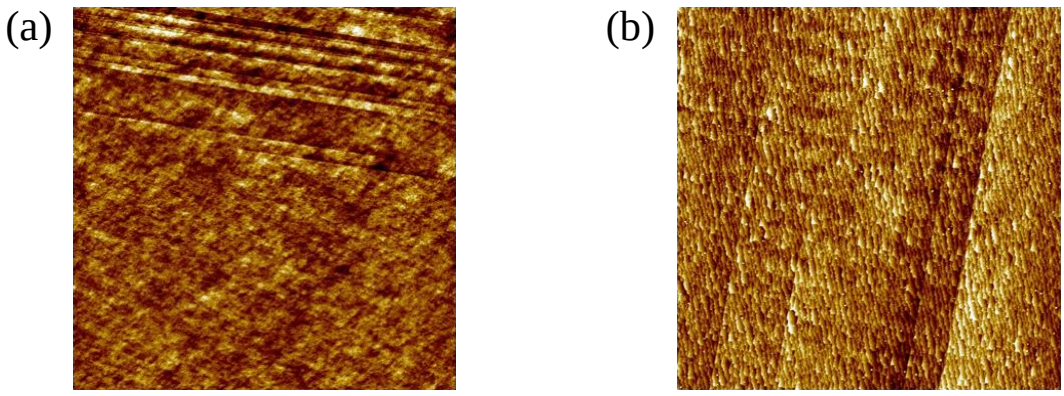

Figure 4.7: Morphology change of a STO crystal. (a) Before annealing. (b) After annealing. The size of the images is 5 μm × 5 μm.

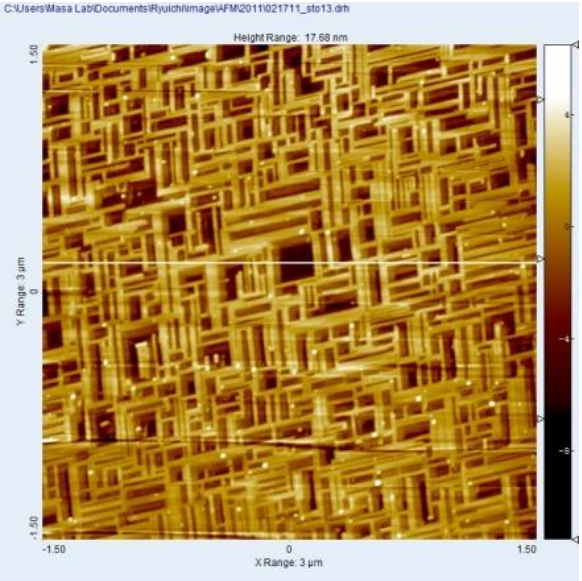

Figure 4.8: An STO crystal etched by a piranha solution.

Once monolayer graphene is located on STO, the same MMA and PMMA A4 polymers are spin-coated on STO as in section 4.1.1 for electron beam lithography. However, an extra layer of metal (25 nm of chromium) is thermally deposited on the top of MMA/PMMA film. In general, a conducting metal layer is necessary for electron beam lithography on electrically insulating substrates in order to discharge electrons from the surface during the lithography process. The electron dosage is the same as in the previous section for this thickness of chromium. The dosage value may need to be adjusted depending on the thickness of the metal film. Alignment markers (Au/Cr) are first deposited in the neighborhood of the graphene. The electrodes are fabricated by electron beam lithography using these markers to align the device design to the graphene. STO is not compatible with the plasma etching. The plasma takes away oxygen atoms from the STO crystal and makes STO electrically conducting. Thus, it is necessary to transfer an isolated piece

of graphene so that there is no need for etching. Finally, Chromium (10 nm) and gold (100 nm) are deposited on the backside of the STO crystal to be used as a backgate electrode.

Figure 4.9: An AFM image of a graphene device on STO. The scale bar is 1 μm.

4.2 Nanotube network device fabrication

For device fabrication on a network of carbon nanotubes covering an entire substrate surface, photolithography is advantageous as the process is much faster than electron beam lithography. However, it is limited in that it cannot fabricate sub-micron size device features. Figure 4.10 shows the device fabrication process using photolithography. First, a substrate with carbon nanotubes is spin-coated with an adhesive layer of HMDS at 4000 rpm for 40 seconds. The undercut layer of LOR is then spin-coated at 3000 rpm for 30 seconds and baked at 170 °C for 5 minutes. On top of the LOR layer, Shipley S1811 is spin-coated at 5000 rpm for 30 seconds and

is baked at 120 °C for 2 minutes. The photoresist-coated substrate is brought into contact with a photomask and exposed to UV light for 6 seconds (Process b in Figure 4.10). After exposure, the substrate is placed in a developing solution, CD-26, for 35 seconds, and then rinsed in DI water for 5 minutes (process c). Chromium (10 nm) and gold (80 nm) are deposited in the thermal evaporation chamber, and the excess metal film is lifted-off in acetone (process d).

In the second lithography step, only HMDS and Shipley are spin-coated, using the same procedure described above. The square pattern in the photomask blocks the UV light so that only the nanotubes between the two electrodes are covered with the photoresist after the development (process e and f). This photoresist acts as a protective layer for the desired carbon nanotubes during the plasma etching process. The exposed carbon nanotubes are then etched away by oxygen plasma (process g). Finally, the device is annealed under a flow of Ar (800 sccm) and H_2 (900 sccm) at 400 °C for 3 hours. The nanotube network device can be cleaned using a UV lamp in UHV as well [71]. Figure 4.11 shows optical and SEM device images. Carbon nanotubes are not visible with an optical microscope, but they can be imaged with SEM.

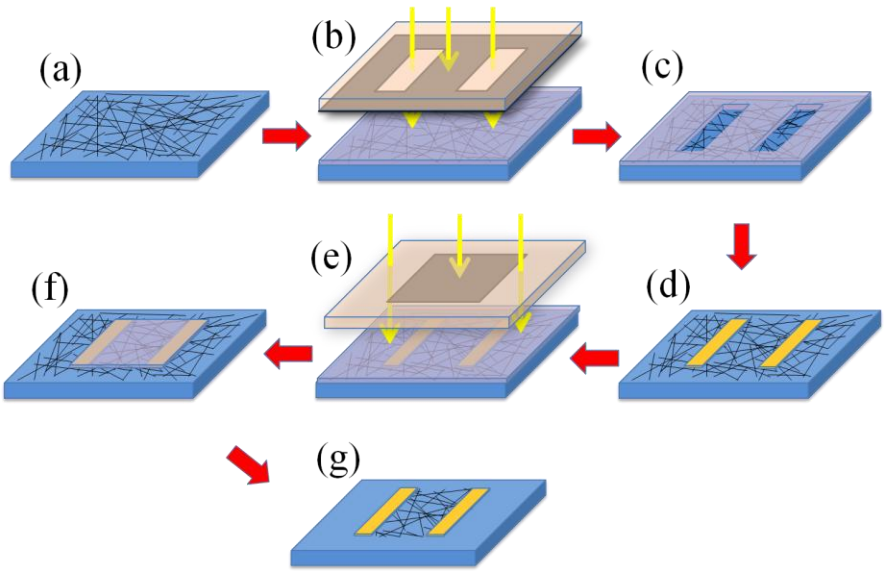

Figure 4.10: Schematic of the photolithography process. (a) A network of carbon nanotubes on a substrate. (b) UV light exposure through a photomask; part of the UV light is blocked. The photoresist becomes selectively soluble in the developing solution after exposure to the UV light. (c) Development washes away the exposed photoresist, exposing the sample beneath. (d) Deposition and lift-off of Cr and Au. (e) The process is repeated with a different photomask to make a protective layer over the device region. (f) Development to expose the nanotubes around the device. (g) Plasma etching of the excess nanotubes.

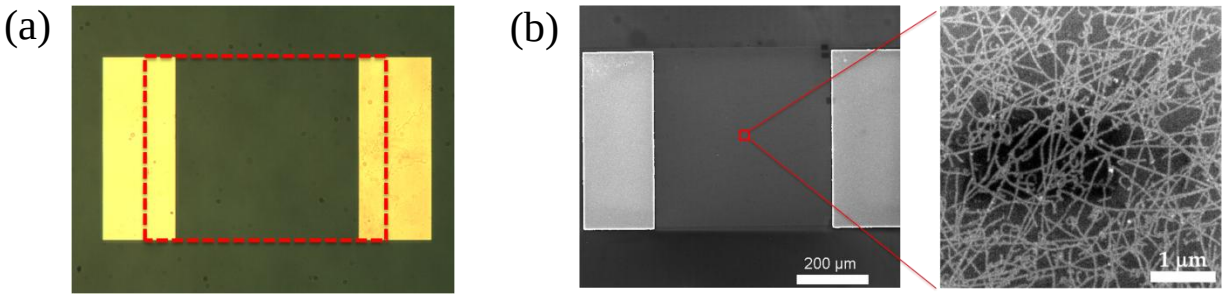

Figure 4.11: (a) An optical image of a nanotube network device. Carbon nanotubes are not visible. (b) SEM images of the network device. The nanotubes outside the device area are etched away.

4.3 Single-walled carbon nanotube device fabrication

The device fabrication process of single-walled carbon nanotubes with known chirality involves multiple, delicate steps in order to ensure the device quality. The device fabrication starts with transferring a suspended carbon nanotube to a target substrate. The deposition of electrodes is achieved by two steps of electron beam lithography in order to optimize electrical contact to the carbon nanotubes.

4.3.1 Carbon nanotube transfer

Once the chirality of a suspended carbon nanotube is identified, as described in section 3.3.5, the nanotube is ready to be transferred onto a substrate. Figure 4.12 shows one such target substrate. It has pre-patterned markers which are separated by 50 μm apart from each other. These markers aid in accurately transferring a suspended nanotube to a specific location. The target substrate is first spin-coated with 60 nm of PMMA A2, and a small rectangular window is made over the markers by electron beam lithography. The surrounding PMMA serves as an anchor to hold the nanotube during the transfer process.

(a) (b)

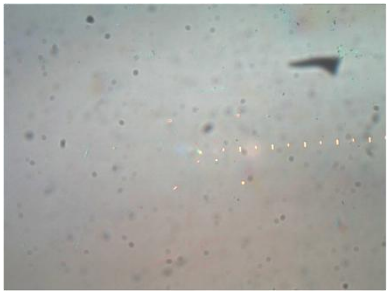

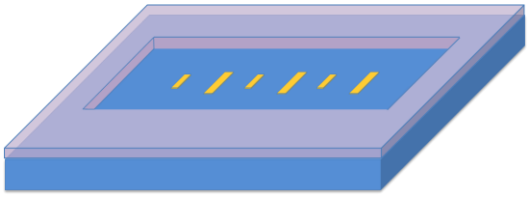

Figure 4.12: (a) An optical image of the target substrate with markers. (b) Schematic of a transfer window.

Figure 4.13 shows the carbon nanotube transfer station. The target substrate is held by vacuum on a stage that can be heated. A small piece of PDMS is placed on a glass slide, and a carbon nanotube chip is placed on the PDMS. The target substrate on the stage is moved to align the nanotube and the transfer window through the microscope. The coordinate of the nanotube from the edge of the window is recorded during the chirality determination process. The coordinate is then used, in conjunction with deposited markers, to align the target substrate to the carbon nanotube. Once the nanotube and the transfer window are aligned, the stage temperature is gradually increased to 180 °C as the target substrate is raised close to the carbon nanotube chip. The PDMS softens during this heating process, and frequent adjustment of the alignment is needed. When the temperature reaches 180 °C, the suspended part of the nanotube is pressed against the target substrate for 5 minutes. Then, the system is allowed to cool, and the target substrate stage is lowered when the temperature falls below 50 °C.

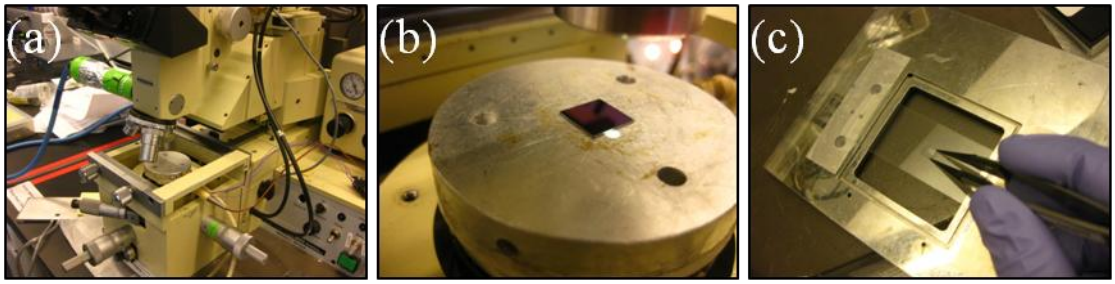

Figure 4.13: (a) Carbon nanotube transfer station. (b) Transfer stage, with cartridge heaters inside to raise the temperature of the stage during the transfer process. (c) PDMS on a glass slide. A suspended nanotube chip will be attached to the PDMS.

4.3.2 Contact resistance issue with single-walled carbon nanotube devices

When an electrode is directly placed on a single-walled carbon nanotube, the electronic transport through the nanotube is inevitably affected by the presence of the electrode. This prevents us from performing the four-probe measurement on nanotubes, and the contact resistance becomes an important issue [72]. The detrimental effects of the electrodes' presence on the nanotubes can be minimized if the contact is ohmic and the contact area is small. However, the charge carriers may not be completely transferred from nanotubes due to the small contact [73]. When two-probe measurements are performed on carbon nanotubes, the experimentally measured resistance is the sum of the nanotube resistance and the contact resistance,

$$R_{measure} = R_{CNT} + R_{contact} \tag{4.1}$$

For ohmic contact, the contact resistance is

$$R_{contact} = \frac{h}{2e^2 M} \tag{4.2}$$

where h is planck constant, e is electron charge, and M is the number of conduction channels (excluding the spin degeneracy). In carbon nanotubes, there are two different conduction channels in the first sub-band at $\boldsymbol{K}$ and $\boldsymbol{K}$' point (M = 2). The ohmic contact resistance is 6.5 kΩ for M = 2. The contact resistance value will be larger than this ideal ohmic contact if a Schottky barrier is formed between the metal contact and semiconducting nanotubes [74-76]. The size of the Schottky barrier is determined by the difference in the work function of metal and semiconducting nanotubes. The larger the work function difference is, the larger the barrier becomes, and the work function of the metal contact needs to be close to that of the semiconducting nanotubes so as to minimize the contact resistance arising from Schottky barrier.

As stated before, gold contacts generally require a sticking layer in order to remain attached to device chips due to the gold's poor adhesion to SiO_2. However, the chromium sticking layer previously used in the graphene devices is not suitable for single-walled carbon nanotubes as the work functions of chromium and carbon nanotubes are 4.5 eV and 5 eV, respectively [77-79]. This difference in work function is large enough that the conduction through the device is dominated by the Schottky barrier. As an alternative, palladium is a typical choice of sticking layer that retains good electrical contact to carbon nanotubes because it has a similar work function and adheres well to SiO_2. However, palladium is not compatible with our hydrogen cleaning process; palladium inflates when it absorbs hydrogen, degrading the contact quality. Therefore, we have chosen to use gold alone to make the electrical contact to carbon nanotubes

because it is compatible with our hydrogen cleaning process and it has a similar work function to that of the carbon nanotubes in question. The solution to the problem of poor adhesion is to develop a two-step electron beam lithography process outlined in the next section.

4.3.3 Two-step electron beam lithography

This two-step electron beam lithography technique is useful when the metal does not adhere to the oxide layer of a target substrate. Figure 4.14 outlines the process. The first lithography step is designed to create breaks in the electrodes so as not to touch the nanotube. These electrodes are deposited following the same electron beam lithography steps as in graphene, and the chromium layer (10 nm) ensures the adhesion of the electrodes. In the second lithography step, the break in each electrode is bridged with only gold. The overlapping gold layers adhere well to one another, preventing the issue of delamination while preserving the desired electrical contact.

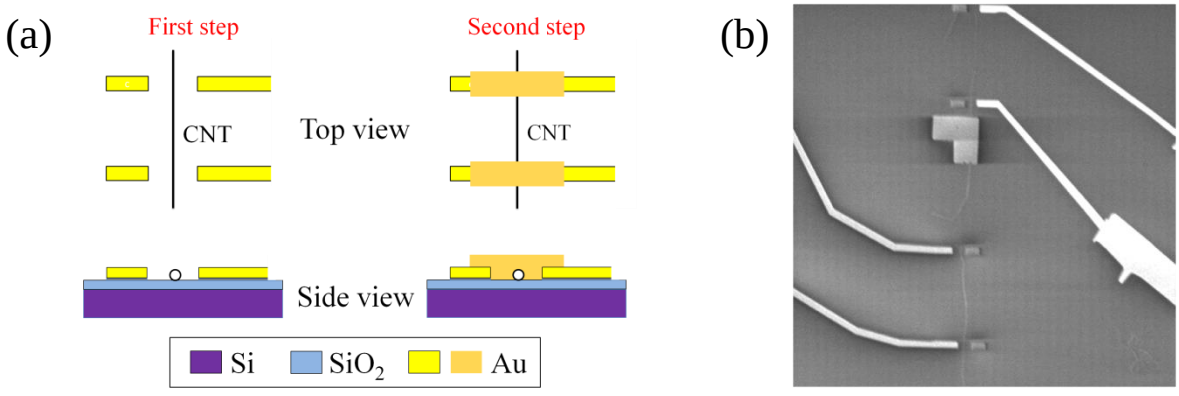

Figure 4.14: Two-step electron beam lithography. (a) Schematic of two-step lithography. (b) An SEM image of a device before the deposition of the gold bridge.

The second lithography procedure is different from the first lithography in order to improve the contact quality by minimizing the incidence of resist residues adhering to the nanotube surface. 300 nm of PMMA 495 is spin-coated first, instead of MMA, and PMMA 950 is spin-coated on top of it. The layer of PMMA is used as an undercut layer due to its improved performance over MMA. The typical agent for development is the mixture of MIBK and IPA, but we found that polymer residues cannot be removed completely using this solution. To resolve this issue and effect a cleaner development, a mixture of IPA and DI water in a 3:1 volume ratio - chilled at 7 °C - is used. The electron beam dosage has to be increased to 550 $\mu C/cm^2$ accordingly to compensate for the chilled developer. The bridge patterns are developed in this chilled solution for 1 minute and 20 seconds. Figure 4.15 shows the clear difference of MIBK/IPA development and chilled IPA/DI water development. 100 nm of gold is deposited after the development, and the devices are hydrogen annealed at 350 °C for 3 hours to remove polymer residue. Extra care is required not to overshoot the temperature as the thin film of gold begins to deform and eventually evaporate around 400 °C.

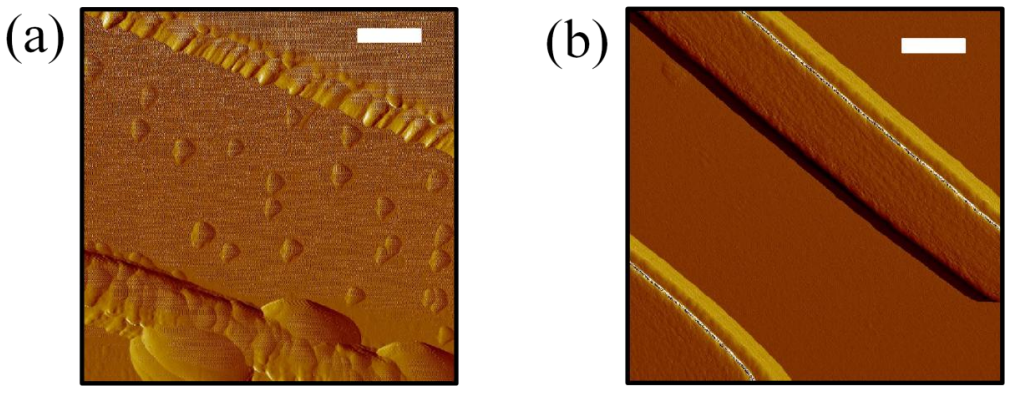

Figure 4.15: AFM images of residues after the development. (a) MIBK/IPA development. (b) DI water/IPA development. The scales bars are 0.5 μm.

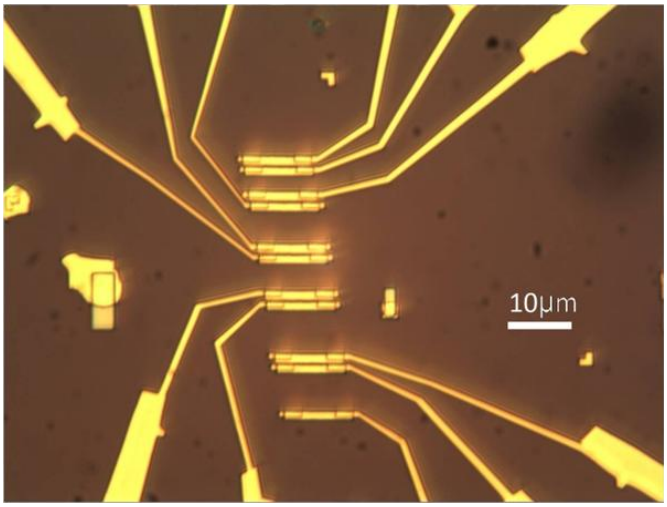

Figure 4.16: An optical image of a single-walled carbon nanotube device.

CHAPTER 5: MEASUREMENT ON GRAPHENE AND NANOTUBE NETWORK

It is of great physical and technological interest to find the effect of an impurity on graphene and carbon nanotubes. The high surface to volume ratio of graphene and carbon nanotubes makes them susceptible to impurities on them. In this chapter, the effect of different kinds of impurities are investigated on graphene and on a network of carbon nanotubes; namely, hydrogen atoms on graphene with silicon dioxide (SiO_2) and strontium titanate (STO) substrates, hydrogen and cesium atoms on a network of carbon nanotubes, and dye aggregates on a network of carbon nanotubes. The effect of atomic potassium on metallic and semiconducting carbon nanotubes is intensively studied and is discussed in the next chapter.

5.1 Measurement of graphene on SiO_2

If graphene is atomically clean and devoid of lattice defects, the theoretical charge carrier mobility limit of 200,000 cm^2/Vs can be achieved at room temperature [80]. When graphene is on SiO_2/Si substrates, the experimental value of the mobility is limited to approximately 10,000 cm^2/Vs. The mobility of charge carriers in suspended graphene approaches the theoretical limit [81], indicating that substrate plays an important role in the reduction of the mobility. In fact, the surface of a thermally grown oxide on Si substrates has electron-hole charge puddles that are tens of nanometers in size which affect the charge carrier mobility of graphene [82]. Placing graphene on clean hexagonal boron nitride (hBN) increases the mobility to 80,000 cm^2/Vs [83].

In order to quantify the relation between extrinsic impurities and mobility, we have measured the change in the electronic transport as atomic hydrogen is introduced on graphene.

5.1.1 Experimental setup

Figure 5.1 shows the schematic of the experimental setup. The device is placed in UHV in order to reduce the interference of other molecules outside of atomic hydrogen. The device is annealed in UHV at 450 K prior to the measurement so as to remove residual gases from the surface of the graphene. The copper block extends outside the UHV chamber, and the device attached to the block is cooled down to 10 – 20 K by extracting heat with a flow of liquid helium. Atomic hydrogen is introduced to graphene via a hydrogen cracker (Omicron Nanotechnology). Hydrogen molecules are cracked into atomic hydrogen as it passes through a tungsten capillary heated to 2300 °C by an electron beam. The amount of hydrogen is controlled by the shutter immediately below the device.

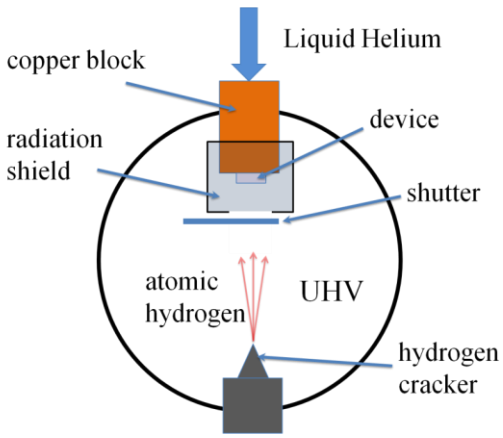

Figure 5.1: Schematic of hydrogen dosing on graphene devices.

5.1.2 Measurement setup

The conductance of graphene is measured with a four-probe configuration. Figure 5.2 shows the experimental schematic. A constant current of 100 nA_{rms} is passed through the source and drain electrodes by connecting a 10 MΩ resistor in series. The resistance of graphene is small (< 1kΩ), and applying $1V_{rms}$ of bias voltage from a lock-in amplifier results in 100 nA_{rms} of constant current. The resistance of graphene is found by measuring the voltage drop between the other two probes, and the sheet conductivity is calculated using the simple ohm's law $R = V/I$ and the area of graphene between the two-probe electrodes. The gate electrode (doped silicon) forms a capacitive coupling to the graphene, and the charge carrier density is continuously varied from electrons (positive gate voltage) to holes (negative gate voltage).

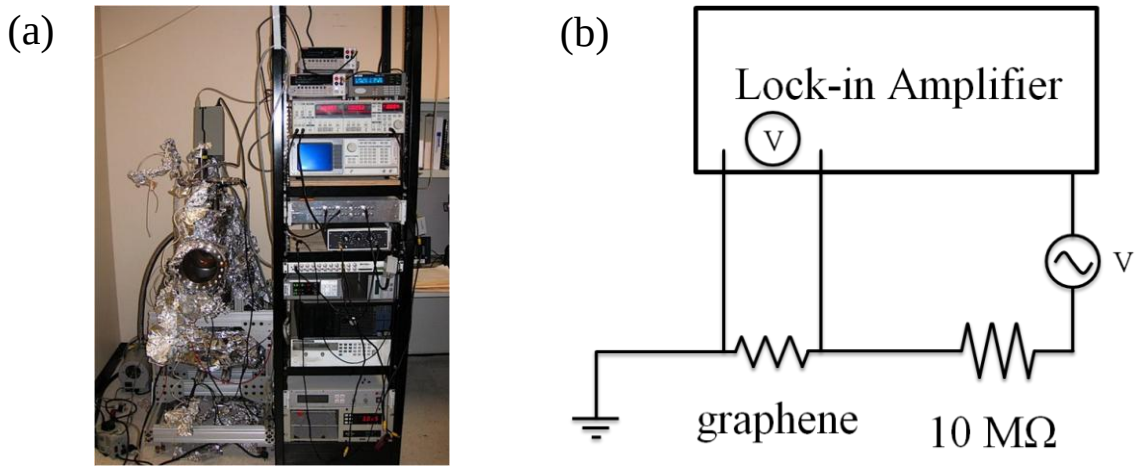

Figure 5.2: The electronic transport measurement setup. (a) An image of the UHV chamber and electronics. (b) Schematic of graphene four-probe measurement.

5.1.3 Hydrogen dosing experiment

Figure 5.3 shows the conductance of graphene at different atomic hydrogen concentrations as a function of gate voltage at T = 12 K. The conductance of graphene before the addition of hydrogen (purple) shows ambipolar conductance. The gate voltage at the minimum conductance point corresponds to the charge neutrality point, where Fermi energy is located at the Dirac point. This minimum conductance point should be located at V_g = 0V without any extrinsic doping. Having the minimum point at around V_g = 4V for our pristine graphene indicates that there is extrinsic doping effect.

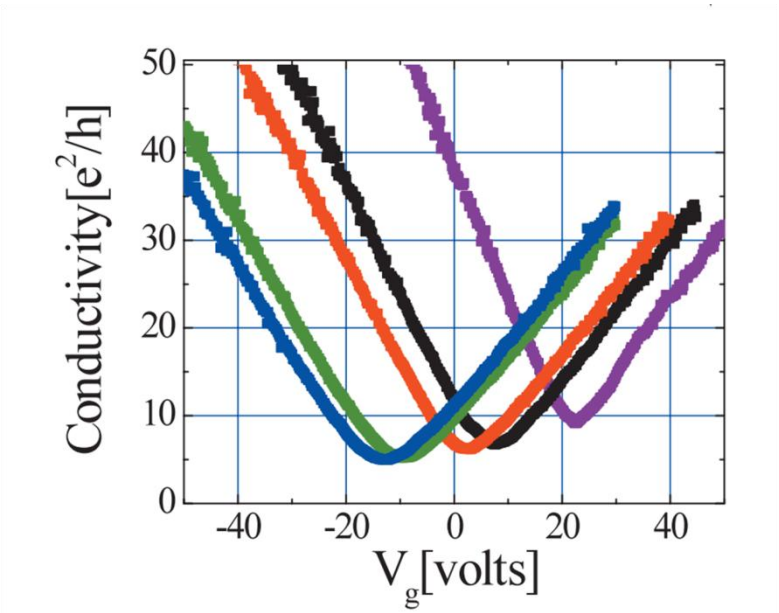

Figure 5.3: Conductance as a function of gate voltage with different amount of atomic hydrogen dosage. The areal densities, the number of impinging hydrogen (which may not be necessarily adsorbed on graphene) are, purple: clean, black: $1 \times 10^{15}/cm^2$, red: $1.6 \times 10^{15}/cm^2$, green: $4 \times 10^{15}/cm^2$, and blue: $5.4 \times 10^{15}/cm^2$.

The field effect mobility of graphene is calculated by

$$\mu = \frac{\sigma}{c_g V_g} \tag{5.1}$$

The slope of the conductivity becomes smaller (mobility decreases) as the concentration of atomic hydrogen increases on the surface of graphene, showing that hydrogen atoms serve as charge carrier scatterers. The conductivity curves also shift to the left with increasing concentration of hydrogen atoms. This is consistent with that hydrogen atoms partially donate electron to graphene.

Figure 5.4a shows the resistivity change from the pristine graphene at different hydrogen dosage levels. The curves with different hydrogen concentration is shifted and aligned at the minimum conductance point (V_{min}) with the new horizontal axis label, $V_g - V_{min}$. The alignment of curves is essentially the same as aligning Fermi energy. According to Matthiesen's rule, the total resistivity is the sum of the resistivity arising from different scattering mechanisms, such as crystal defect, phonon, and extrinsic impurity, assuming that each scattering mechanism is independent of each other.

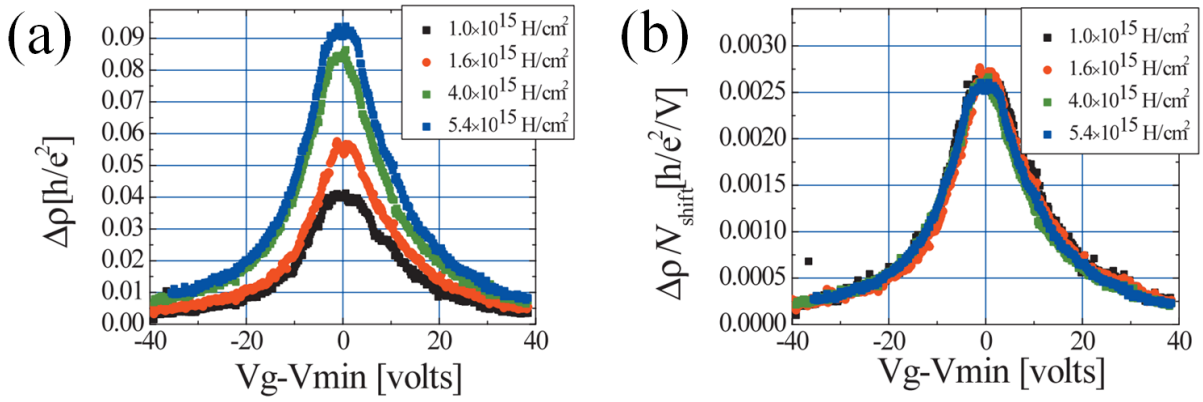

Figure 5.4: (a) Resistivity added by hydrogen as a function of $V_g - V_{min}$ at different areal dosage density. (b) Added resistivity as a function of the areal dosage density normalized to V_{shift}.

$$\rho_{total} = \rho_{defect} + \rho_{phonon} + \rho_{adsorbate} \tag{5.2}$$

In our experiment, $\rho_{adsorbate}$ is the dominant contribution to the change in resistivity since the number of atomic defect is small and constant and the scattering due to phonon is suppressed at the low temperature. This is verified when the change in resistivity is divided by V_{shift}, the gate voltage offset imposed by the electron doping from hydrogen atoms (Figure 5.4b). Since V_{shift} is proportional to the number of atomic hydrogen attached on graphene, the fact that all the curves collapse onto each other when divided by V_{shift} shows that the change in resistivity is indeed proportional to the number of hydrogen. Interestingly, as the concentration of hydrogen atoms increases, V_{shift} approaches to the saturation point (V_{sat}), where the curve does not shift anymore (Figure 5.5a).

We have performed the same measurement with multiple graphene devices, and V_{sat} for each device is recorded. In Figure 5.5b, the inverse initial mobility, which is proportional to resistivity of pristine graphene, is plotted against V_{sat} for each device, and they show a linear correlation. The (inverse) initial mobility shows different values because the number of atomic defects is different in each graphene device. Thus, this correlation indicates that hydrogen atoms preferentially attach to these native atomic defects and saturate once the defect sites are exhausted. The pristine limit of graphene mobility on thermally grown SiO_2 is deduced to be 1.5 $\pm$ 0.3 $\times$ 10^4 cm^2/Vs. This is the upper limit of graphene mobility imposed by the presence of the electron-hole charge puddles on SiO_2. The mobility is reduced by an order of magnitude from the theoretical value of 200,000 cm^2/Vs, and it concludes that the substrate on which graphene is placed on needs to be free of electron-hole charge puddles in order to achieve the high mobility of graphene.

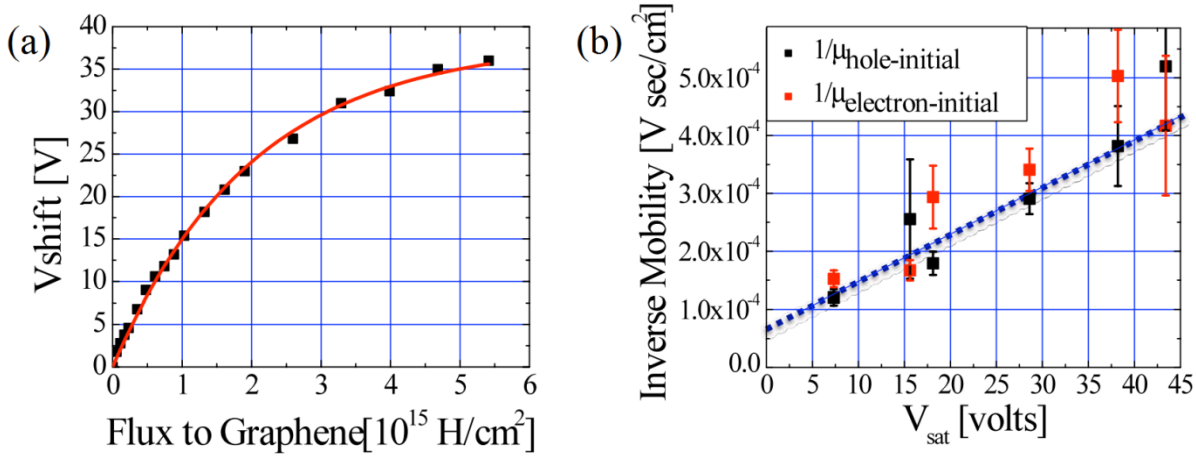

Figure 5.5: (a) V_{shift} as a function of the increasing areal dosage density. (b) Initial maximum electron and hole mobility as a function of the saturation voltage shift, V_{sat}, for different samples.

5.2 Measurement of graphene on Strontium titanate

Placing graphene on a material with a high dielectric constant is of particular interest. According to the simple parallel plate capacitor model, a high dielectric constant leads to a larger capacitance. Strontium titanate, which has a dielectric constant of 330 at room temperature, has a capability to induce more charges in graphene. The high charge density and high dielectric constant increase an effective screening of impurity charges, and the mobility of graphene is expected to increase on STO. In this section, mobility measurement of graphene on STO is discussed.

5.2.1 Gate dependence of conductance in graphene on STO

A graphene device fabricated on STO as described in section 4.1.2 is placed in a helium-3 cryostat to measure conductivity of graphene with the four-probe configuration. The thickness of the STO crystal is 200 μm. Figure 5.6 shows the conductivity as a function of gate voltage at T = 4.6 K. The ambipolar behavior of the conductivity is consistent with that of graphene on SiO_2. The conductivity over the small gate scan range (Figure 5.6a) shows only a minimal amount of hysteresis. The minimum conductivity point is located in the positive gate voltage side, which indicates that the graphene is electron-doped by impurity charges on the STO crystal. However, it is not clear if the doping is coming from impurities introduced during the device fabrication process or from bound charges at the edges of the crystal terraces on the surface of STO. The AFM image of the device does not show a significant amount of residue on or underneath the graphene, and charged impurities are expected to be effectively screened. This indicates that the

native surface impurities on the STO are causing the doping. The fact that the surface of STO is not atomically flat but consists of many terraces also supports this scenario. The precise nature of the doping may be revealed by Kelvin probe measurement, which is not discussed here.

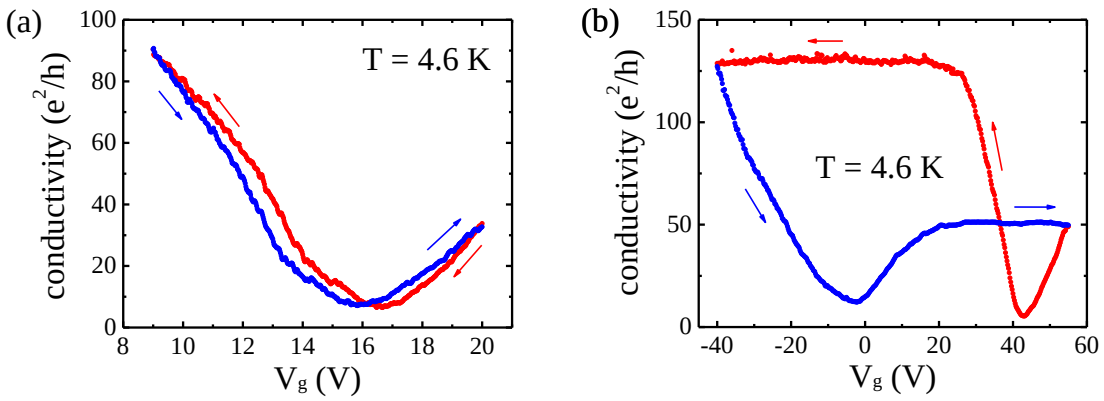

Figure 5.6: Conductivity as a function of gate voltage. (a) The conductivity over small gate scan range. It shows minimal hysteresis. (b) The conductivity over large gate scan range. The hysteresis is prominent. The minimum conductivity value is smaller when the gate voltage is swept down to the negative gate voltage side. In both plots, arrows represent the direction of the gate voltage sweep.

Another interesting aspect of the conductivity curves is that the minimum conductivity value is lower when the gate voltage is swept toward the negative voltage. This difference becomes clear when the gate scan range is increased, as in Figure 5.6b. In this plot, the degree of the hysteresis becomes prominent as well. The difference in the minimum conductivity values may be related to the ferroelectric modulation of the surface state on the STO.

For the large gate scan range, it is clearly seen that the conductivity plateaus out at the higher gate voltage. This saturation of conductivity is not intrinsic to the graphene but is coming from

that the dielectric constant of STO has dependence on the applied electric field: the dielectric constant decreases as the applied electric field increases. This effect limits the maximum charge density in the graphene to be 1.1×10^{13} cm^{-2} for the 200 μm thick STO. This number can be attainable with graphene on SiO_2. However, thinning the STO crystal down to 0.2 μm will increase the charge density by three orders of magnitude to be in the range of 10^{16} cm^{-2}. Thin STO crystals can be epitaxially grown, and it provides a way to induce a large charge density in graphene. On the other hand, the gate dependence of the dielectric constant of STO makes it difficult to calculate the mobility of the graphene from the conductivity vs. gate voltage plot. In order to find the mobility, Hall effect is measured at low temperature.

5.2.2 Hall Mobility measurement of graphene on STO

Hall effect measurement is another avenue to find the charge density in the graphene. The charge density, n , is related to Hall voltage, V_{Hall}, by

$$n = \frac{IB}{eV_{Hall}} \tag{5.3}$$

where I is electric current, B magnetic field, and e electron charge. Figure 5.7 is the measured Hall voltage at 4.8 K with 1.0 T of constant magnetic field applied perpendicular to the graphene. As the gate voltage is varied, the charge density changes in the graphene and as a result, Hall voltage changes. In the gate voltage range between 9 V and 15 V, Hall voltage is positive and increases (in this case, it corresponds to charge carriers being holes). However, it

starts decreasing around V_g = 15 V, and the sign changes to negative (corresponds to electrons as charge carriers) at V_g = 16.5 V. According to the equation, Hall voltage diverges as the charge carrier is continuously varied from holes to electrons in graphene, a zero gap semiconductor. However, the surface charges become dominant near the charge neutrality point ($V_g \approx$ 16.5 V), and the charge density in graphene is affected by them. Figure 5.7b shows the conversion of the gate voltage into the charge density. Away from the charge neutrality point, the charge density shows a linear dependence on the gate voltage.

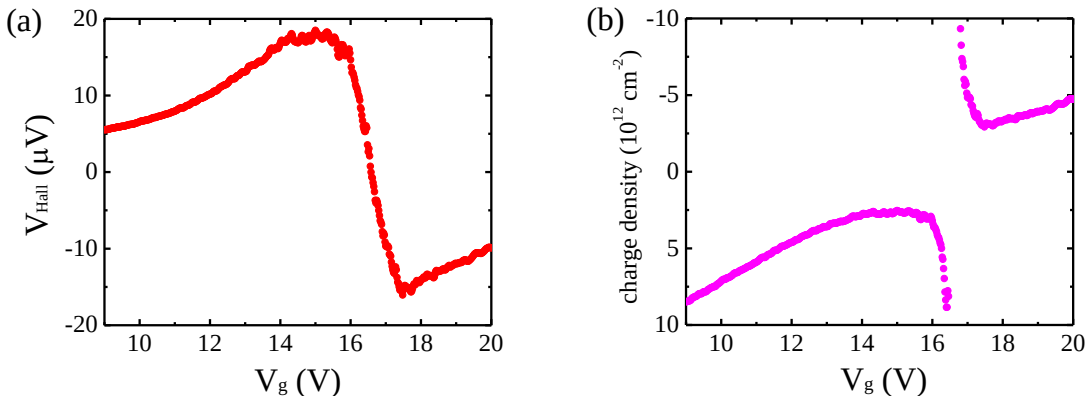

Figure 5.7: Hall measurement. (a) Hall voltage as a function of gate voltage. (b) The conversion from the gate voltage to charge density in the graphene. The positive (negative) charge density represents holes (electrons).

When large gate voltage is applied (Figure 5.8a), it is clearly seen that the charge density saturates. The charge saturation for holes (~1.5 × 10^{13} cm^{-2}) is about three times larger than that of electrons (~0.5 × 10^{13} cm^{-2}). From the theoretical limit of charge density 1.1 × 10^{13} cm^{-2}, it is estimated that there are net *negative* charges of density 0.5 × 10^{13} cm^{-2} on the STO. It is negative charges since the presence of negative charge near the surface of graphene induces positive

charges. This is consistent with the fact that the minimum conductivity point is shifted to the positive gate voltage side (hole doped) as in Figure 5.6a.

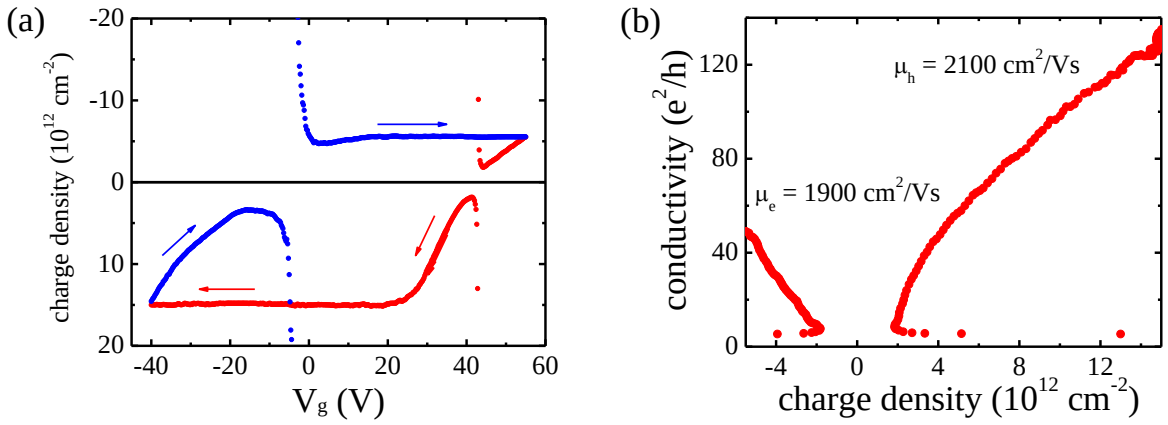

Figure 5.8: (a) The conversion of the gate voltage to the charge density in the graphene for the large gate scan range. It exhibits a strong hysteresis effect and shows the (asymmetric) saturation of charge density for holes and electrons. The positive (negative) charge density represents holes (electrons). Arrows represent the direction of the gate voltage sweep. (b) The conductivity as a function of the charge density induced in the graphene. The gate voltage is converted to the charge density according to the Hall measurement.

Once the conductivity is plotted against the charge density, the Hall mobility is calculated (Figure 5.8b). From the slop of the conductivity curve, the mobility is found to be 2100 cm^2/Vs for hole conduction and 1900 cm^2/Vs for electron conduction. The mobility does not show a significant improvement for the graphene on STO. This may be caused by the inhomogeneity of the STO surface, i.e., the STO crystal itself has a significant amount of surface bound charges, which results in the reduction of the mobility. In this experiment, the induced charge density is comparable to that of graphene on SiO_2, and the charge screening effect is not as strong as

expected. This situation may change when the thickness of the STO crystal is reduced to 0.2 μm to induce more charges in the graphene.

5.3 Measurement on a network of carbon nanotubes

A network of carbon nanotubes has a potential use for sensing application as described in section 1.2. In order to fully utilize the carbon nanotube as a sensor, it is important to understand how a network of carbon nanotubes responses to extrinsic impurities. We have measured the effect of hydrogen and cesium atoms on the electronic transport through a network of carbon nanotubes. Functionalization of a network of carbon nanotubes with dye molecules is also discussed in this section.

5.3.1 Network of nanotubes as a percolation system

A network of carbon nanotubes consists of a mixture of metallic and semiconducting carbon nanotubes. Charge carriers transport from one nanotube to another through the mesh of carbon nanotubes. The electronic transport properties are largely determined by the ratio of metallic nanotubes to semiconducting nanotubes, the average length of each nanotube, and the number density of nanotubes. Regarding the ratio, one third of the nanotubes are assumed to be metallic for simplicity according to the condition for the metallic nanotubes ($n - m = 3l$).

The length and number density are two key parameters that describe the characteristics of the network. The electronic transport from source to drain electrode is only possible when there are paths of nanotubes connecting these two electrodes. For example, if the number density is small, each carbon nanotube needs to be long enough to create a path connecting two electrodes. If the nanotube length is short, the number density needs to be large. The network of carbon nanotubes is considered as a percolation system. The threshold of percolation is determined by the relation [84], $L_{ave} > \rho^{-1/2}$, where L_{ave} is the average length of nanotube and ρ is the number density. The length and number density can be found using SEM images. Figure 5.9 is an SEM image of part of a carbon nanotube network device. 147 nanotubes are counted in 53 μm × 53 μm area (number density ρ = 0.052 μm^{-2}) with the average nanotube length of L_{ave} = 11.3 μm. This is dense enough to be above the percolation threshold.

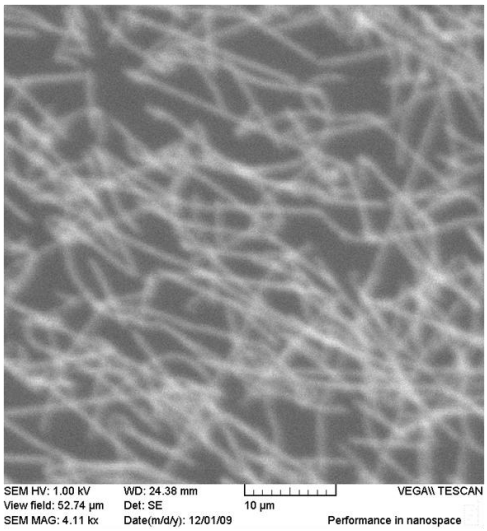

Figure 5.9: A network of carbon nanotubes. The number of nanotubes is counted one by one, along with the measurement of the nanotube length.

5.3.2 Hydrogen and cesium dosing experiment

Figure 5.10 is the conductance of a nanotube network device as a function of gate voltage in ultra high vacuum (UHV) at room temperature. It shows ambipolar, almost symmetric conductance. The ambipolar transport is the characteristics of metallic and semiconducting carbon nanotubes [85]. At the conductance minimum, semiconducting nanotubes become non-conductive, and the transport is only carried by the network of metallic nanotubes [84, 86]. The transport is still above the percolation threshold at this point, assuming that one third of nanotubes are metallic. Hence, we only consider non-percolative transport from this point on.

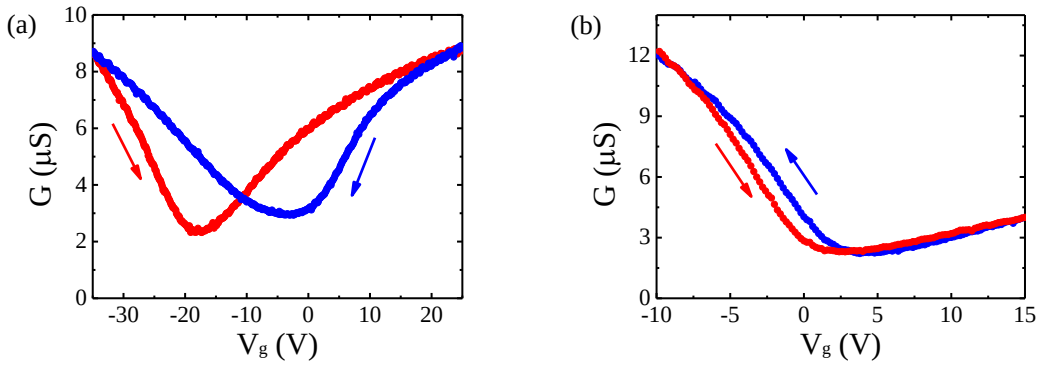

Figure 5.10: The conductance vs. gate voltage. Arrows represent the direction of the gate voltage sweep. (a) The conductance measured in UHV at room temperature. (b) The conductance measured in the air at room temperature. The electron conduction side (positive gate voltage side) is suppressed as compared to that in UHV.

The device conductance in UHV is slightly different from the one in the air (Figure 5.10b). The hole conduction (toward the negative gate voltage) is suppressed in UHV while the electron conduction (toward the positive gate voltage) is enhanced. The suppression and enhancement of conductance are attributed to the modulation of the Schottky barrier formed at the cross junctions

of metallic and semiconducting nanotubes: the depletion of oxygen from the junctions in UHV changes the Schottky barrier height [74, 87]. The Schottky barrier is also formed at the interface of nanotubes and metal electrodes, but this has a minimal contribution to the total device conductance since the metal contact is 750 μm wide [86, 88].

At the conductance minimum, the effect of the Schottky barrier should be negligible since only metallic nanotubes are responsible for the electronic transport (semiconducting nanotubes turn off). The transport around the minimum conductance point is governed by the resistance of metallic nanotubes and the resistance arising from the metallic nanotube junctions. The resistivity of a single metallic nanotube at its conductance minimum can be estimated to be approximately from 120 to 160 kΩ/μm from the work of *Kong et. al* and *Purewal et. al* [89, 90]. The density of metallic nanotubes $\rho_{metal} = 1/3\rho = 0.017\ \mu m^{-2}$ corresponds to the average of 1 nanotube in 5 μm × 5 μm area. One metallic carbon nanotube crosses another metallic carbon nanotube about every 5 μm, leading to 600 to 800 kΩ of a metallic nanotube without crossing another metallic nanotube. This is comparable with the resistance arising from a metallic nanotube cross junction of 259 kΩ [91]. Thus, the contribution of junction resistance cannot be ignored at the conductance minimum.

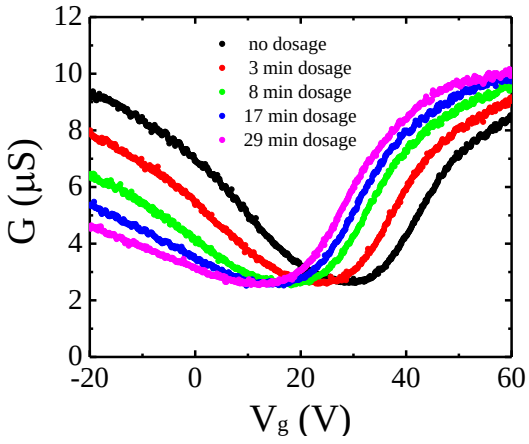

Figure 5.11: The conductance of the network of carbon nanotubes as a function of gate voltage with hydrogenation. The conductance curves start shifting toward the negative gate voltage side due to electron doping from hydrogen atoms. The hole conduction side is suppressed because of the presence of hydrogen, but the minimum conductance is not affected.

In order to investigate the response of the nanotube network device to hydrogen atoms, the same hydrogen cracker is used as in the graphene hydrogenation experiment described in section 5.1. When the nanotubes are hydrogenated in UHV at room temperature, the whole conductance curve is shifted toward the negative gate voltage side (Figure 5.11) as a result of electron doping from hydrogen atoms. We aligned each conductance curve from different hydrogen dosage at the minimum conductance point for comparison (Figure 5.12).

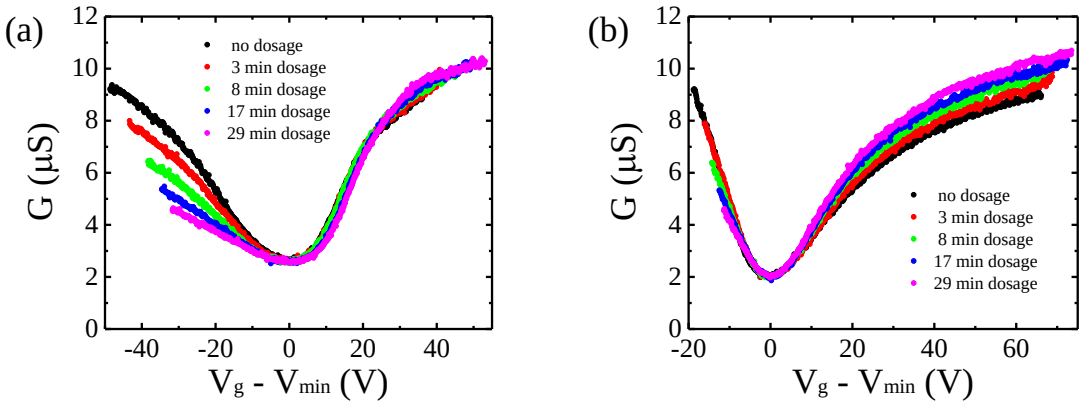

Figure 5.12: The conductance curves are aligned to the minimum conductance point. (a) The gate voltage is swept toward the negative gate voltage. (b) The gate voltage is swept toward the positive gate voltage. The enhancement of the conductance on the electron conduction side is more visible.

The minimum conductance point, does not show a significant change with hydrogenation, indicating that metallic nanotubes and metallic nanotube junctions are resilient to hydrogen atoms [92]. Away from the metallic nanotube conduction around the minimum point, it is clear that the hole conduction becomes increasingly suppressed with the hydrogen dosage (Figure 5.12a), whereas the electron conduction is enhanced (Figure 5.12b). This behavior is consistent with the conductance change due to a modulation of the Schottky barrier. In this case, the observed conductance change is dominated by the Schottky barrier formed at the junction of metallic and semiconducting carbon nanotubes.

The nanotube network devices are effectively cleaned after the experiment by annealing in UHV at 450 K. The adsorbed atoms are thermally removed during the annealing process so that the direct comparison of the effect of different adsorbed atoms becomes possible. Figure 5.13 is the

result of cesium dosing on the same nanotube network device in UHV at room temperature. Cesium atoms are introduced onto carbon nanotubes with a cesium atom dispenser (SAES). The detail of the operation of alkali metal dispensers is discussed in section 6.2.4. As seen in the hydrogen case, the conductance on the hole side is suppressed, while the electron side is enhanced. However, the minimum conductance increased with cesium dosage. It is counterintuitive that the addition of impurities results in the increased conductance.

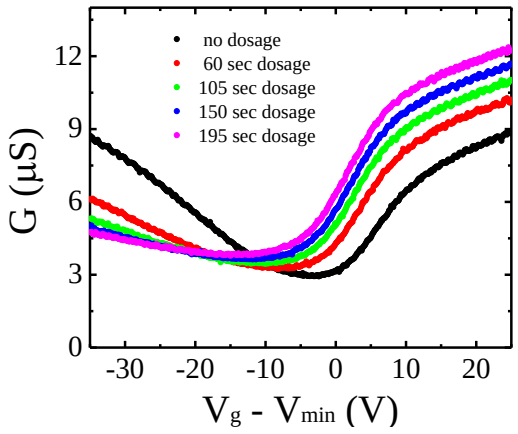

Figure 5.13: The conductance of the network of carbon nanotubes as a function of gate voltage with the addition of cesium atoms. The curves shifts to the negative gate voltage side due to the electron doping from the cesium atoms. Interestingly, the minimum conductance increases.

The enhancement of the minimum conductance can be clearly seen once the minimum points from each conductance curved are aligned, as shown in Figure 5.14. Since only metallic nanotubes are conducting at the minimum conductance point, this behavior can be explained by the reduction of the resistance at metallic nanotube junctions. The metallic nanotubes themselves are resilient to the presence of cesium atoms, but the junction resistance may be reduced by

cesium atoms, leading to the enhancement of the conductance. This is one possible scenario since the junction resistance makes a considerable contribution to the resistance as discussed above. The difference between hydrogen and cesium atoms may be explained by hydrogen's preferential attachment to defect sites, as discussed in section 5.1.

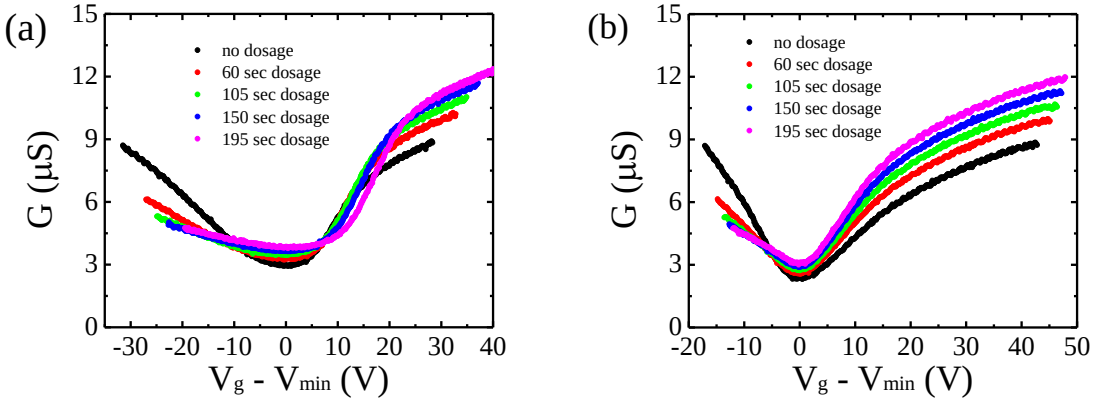

Figure 5.14: The conductance curves are aligned to the minimum conductance point from the cesium dosing experiment. The hole and electron conduction side behaves in the same way as in the hydrogenation case. However, the minimum conductance value increases as cesium atoms are introduced on the nanotube network device.

Another possible scenario is a modulation of the Schottky barrier at the metallic and semiconducting nanotube junctions. Potassium atoms are known to modulate Schottky barrier in semiconducting carbon nanotube devices [74], and cesium is assumed to have the same effect. Reduction of the Schottky barrier leads to opening more conduction channels through semiconducting nanotubes in the network. Even though the precise mechanism of the conductance enhancement is not clear, it is demonstrated that a network of carbon nanotubes can be used to detect different type of atoms. Further understanding on the mechanism of the

modulation of the Schottky barrier by different atomic species is needed to have an accurate control of carbon nanotube sensors.

5.3.3 Dye aggregates

In the previous section, the electronic response of the nanotube network devices to different kinds of atomic impurity is studied. Such modulation of conductance with extrinsic agents suggests that the performance of the nanotube network devices may be improved by intentionally adding molecules on nanotubes. Squaraine dye molecules (SQ dyes) have a specific optical absorbance as monomers. π–π interaction between SQ dye molecules, however, transforms the dye molecules into an aggregate and changes the optical response. We expect a unique π–π interaction between nanotubes and SQ dyes due to the π–bond of the nanotubes, and this motivates us to measure the optical response of the nanotube network devices with SQ dye molecules. When SQ dyes are stacked into supramolecular structures, the strong intermolecular π–π interaction known as J (Jelley)-aggregates and H (Hypsochromic)-aggregates are formed. Molecules are stacked side-by-side in J-aggregates, while stacked face-to-face in H-aggregates. As compared to the absorption band of dye monomers, J (H)-aggregates have red (blue)-shifted absorption bands, called J (H)-bands. The specific SQ dye we used is (Z)-2-(4-(dibutylamino)-2-hydroxyphenyl)-4-(4-(dibutylaminio)-2-hydroxycyclohexa-2,5-dienylidene)-3-oxocylcobut-1-enolate (SQ44OH), and it has molecular structure as shown in Figure 5.15. SQ44OH is dissolved in 1,2-dichloroethane (DCE) with concentration of 1 wt%. Dye molecules in DCE have a single peak in the optical adsorption spectrum at 650 nm with a full width at half maximum of 29 nm,

indicating that SQ44OH molecules are in the form of isolated monomers in the DCE solution.

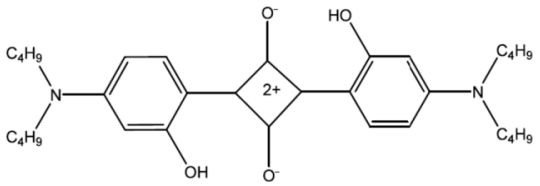

Figure 5.15: Structure of an SQ44OH dye molecule.

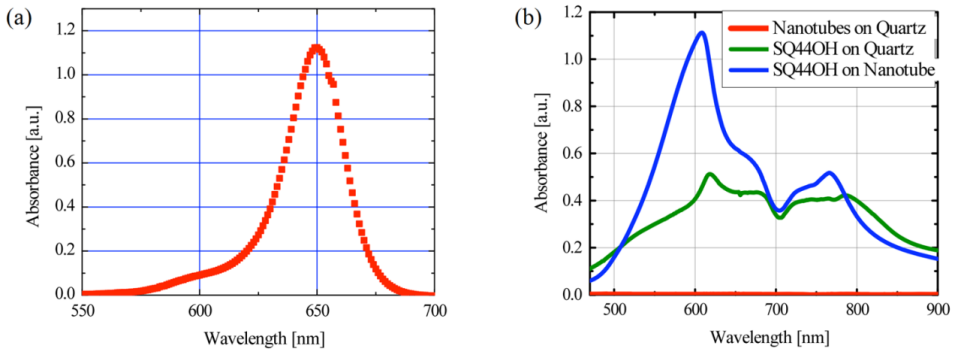

Figure 5.16: Optical absorption spectra of SQ44OH. (a) The absorbance of SQ44OH in DCE. The single peak at 650 nm is a signature of monomers. (b) The absorbance of SQ44OH spin-coated on quartz or nanotubes.

When a thin film of SQ44OH is spin-coated on a quartz substrate, new peaks emerge in the absorbance at 618 nm and 785 nm due to the formation of aggregates, each with broad shoulders tending toward 700 nm (Figure 5.16). These peaks correspond to the blue-shifted and red-shifted absorption band of H-aggregates and J-aggregates. With the absence of the network of carbon nanotubes, SQ44OH molecules exist as a mixture of H- and J-aggregates on quartz substrates. When the same SQ44OH is spin-coated on the carbon nanotubes grown on a quartz substrate, the

two peaks have blue-shifted to 608 nm and 766 nm. The blue-shifting of H- and J-bands is possibly caused by the interaction of dye aggregates with nanotubes. The absorbance increased by 115% at the H-band, while increased by 20% at the J-band. The H-band is significantly enhanced with the presence of carbon nanotubes.

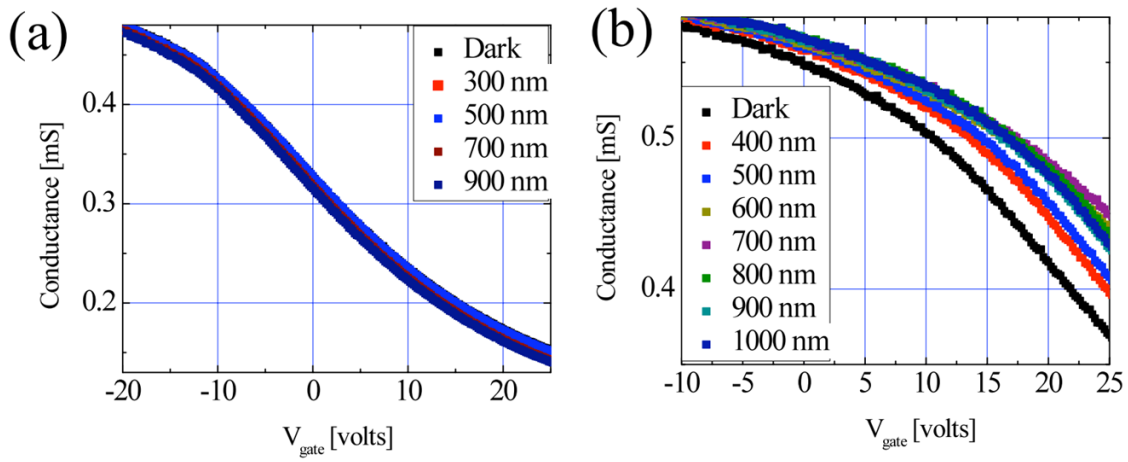

Figure 5.17: Optoelectronic response of the nanotube-dye system. (a) Without SQ44OH. (b) With SQ44OH.

Figure 5.17 shows the optoelectronic response of the nanotube/dye system as a function of gate voltage, comparing the optical response of bare and SQ44OH-coated nanotube network devices. The bare nanotubes have only a small optical response and are not correlated with wavelength of the incident light. This is likely to be caused by the gate oxide stress induced by the applied gate voltage [93]. On the other hand, SQ44OH hole-dopes the nanotubes and shifts the curves to the positive gate voltage side. The curves shifts even more in response to light due to optical gating [94-97]. This optically induced change in conductance has wavelength dependence, and it matches with the optical absorbance peaks of the nanotube/dye system. Assuming that the optical

response is linear with the intensity of the incident light, the device sensitivity is estimated to be 20 μW cm^{-2} in the optical window of 620 to 760 nm with 25 V of gate voltage. The photosensitivity is improved by the combination of the SQ dye and nanotubes. This result is better than dye monomer [95, 97] or photoactive polymer-sensitized [98] devices by an order of magnitude.

CHAPTER 6: MEASUREMENT OF SINGLE-WALLED CARBON NANOTUBES

While studies of electronic transport in carbon nanotubes have been carried out for over two decades, still little is understood about the impact of extrinsic charged impurities. The lack of research may be due to the complexity arising from the contact resistance as discussed in section 4.3. As a consequence, no previous experiment has been able to determine the scattering induced by Coulomb potential on carbon nanotubes. Metallic carbon nanotubes have fundamentally different electronic properties which come from the extra degree of freedom, pseudospin, as described in chapter 2. Pseudospin conservation does not allow backscattering in metallic carbon nanotubes within the same valley. The effect of pseudospin conservation will be manifested when a long-ranged, Coulomb potential is imposed on carbon nanotubes, i.e., the Coulomb potential is not an effective charge-carrier scatterer on metallic carbon nanotubes. However, semiconducting carbon nanotubes will exhibit an increase in resistance with the addition of such a potential. This difference can be observed experimentally by introducing charged impurities on carbon nanotubes. In this chapter, the experiment to determine the scattering strength of a *single* potassium atom on carbon nanotubes of known chirality is discussed in detail. The experimental results are compared with theoretical simulations by a recursive Green's Function method in the tight-binding model.

6.1 Pseudospin conservation conjecture

Theoretically, the intravalley scattering in metallic carbon nanotubes is forbidden because of the pseudospin conservation [92, 99, 100]. This restriction is derived from calculating transition amplitude. In graphene the transition amplitude due to a scattering potential is treated with perturbation theory

$$\langle \theta_{\boldsymbol{k}'} | V_{\boldsymbol{k}'-\boldsymbol{k}} | \theta_{\boldsymbol{k}} \rangle \tag{6.1}$$

For a long-range impurity potential, the Fourier component of the impurity potential is considered to be constant because the wavevector is small, and this leads to

$$|\langle \theta_{\boldsymbol{k}'} | V_{\boldsymbol{k}'\boldsymbol{k}} | \theta_{\boldsymbol{k}} \rangle|^2 = V_{\boldsymbol{k}'\boldsymbol{k}}^2 \cos^2 \frac{\theta_{\boldsymbol{k}'\boldsymbol{k}}}{2} \tag{6.2}$$

where $\frac{\theta_{\boldsymbol{k}'\boldsymbol{k}}}{2}$ is the angle between $\theta_{\boldsymbol{k}'}$ and $\theta_{\boldsymbol{k}}$. The amplitude decreases as the overlap between pseudospin decreases, and it reaches zero when the angle becomes π. In metallic nanotubes, backscattering happens from $\boldsymbol{k}$ to $-\boldsymbol{k}$ (angle π) because the quantized states pass through the Dirac point and the transition amplitude becomes zero, forbidding backscattering within the same valley. It leads to the pseudospin conservation since the pseudospin cannot flip. Backscattering may happen over different valleys at $\boldsymbol{K}$ and $\boldsymbol{K}$', but the intervalley scattering is rare since it requires a large momentum transfer. This restriction claims that Coulomb potential imposed by potassium atoms will not backscatter charge carriers in metallic nanotubes. However, this is not the case with semiconducting carbon nanotubes. The forward and backward

wavevector (***k*** and –***k***) have appreciable overlap of pseudospins (mixed state), and this leads to finite scattering probability. If the scatterer is short-ranged, the Fourier component with $q \sim K$ is not taken to be constant, and the forward state will be coupled with backward state in metallic carbon nanotubes, resulting in backscattering.

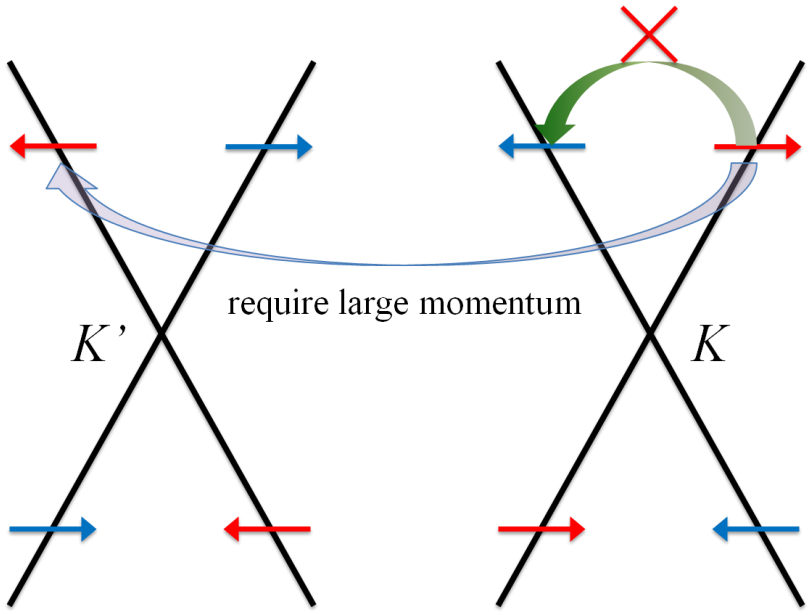

Figure 6.1: Schematic of backscattering in metallic carbon nanotubes.

6.2 Measurement setup

6.2.1 The concept of the experiment

In this experiment, we introduce potassium atoms on atomically-clean metallic and semiconducting carbon nanotubes. A flux of potassium atoms is generated with the same alkali

metal dispenser (SAES) as in section 5.3. Potassium atoms donate a partial electron to the nanotubes and become positively charged. This positive Coulomb potential on nanotubes serves as a charge-carrier scatterer. We measure the resistance change induced by the presence of these positively-charged potassium atoms on nanotubes. The scattering strength (resistance coming from a single potassium atom) is deduced from the change in resistivity (kΩ/μm) and the number density of potassium (atom/μm). As previously mentioned, due to the pseudospin conservation, the scattering strength of a potassium atom is expected to be much smaller in metallic carbon nanotubes than in semiconducting carbon nanotubes.

6.2.2 Ultra-high vacuum and low temperature

Ultra-high vacuum (UHV) and low temperature are two important prerequisites for an accurate measurement of the scattering strength. For this experiment, the surface of the carbon nanotubes needs to be atomically clean before the introduction of the potassium adsorbates in order to isolate their effect on resistivity. To this end, a hydrogen annealing process removes polymer residue, as described in section 4.3.3. However, carbon nanotubes readily adsorb molecules from the air, and these adsorbed molecules interfere with the potassium atoms. UHV minimizes the adsorption of molecules and is also important in maintaining a constant flux of potassium from the alkali metal dispenser.

The temperature of carbon nanotubes needs to be less than 20 K during the experiment for two reasons. The first is to prevent potassium atoms from diffusing along or off of the carbon

nanotubes as this makes the number of potassium atoms on the nanotubes uncertain. The binding energy of a potassium atom on graphite is 30 meV [101], and the same value is adopted to estimate the temperature needed to freeze potassium atoms. The other reason is to minimize the phonon contribution to the resistance of the carbon nanotubes. However, the temperature of nanotubes may increases due to Joule self-heating if a large current is passed through nanotubes. The method to identify the impact of Joule self-heating is discussed in Appendix.

Some issues arise when measurement is performed in UHV at low temperature. Carbon nanotube devices show suppression or enhancement of conductance in UHV: the same effect as in the measurement of the network of nanotubes in section 5.3. The depletion of oxygen molecules from the device in UHV is responsible for this effect. Oxygen creates an extra dipole layer that modifies the height of the Schottky barrier. When oxygen is depleted in vacuum, the change in the barrier height leads to a change in the contact resistance. The Schottky barrier at contacts is also known to be affected by charged adsorbates such as potassium [72, 74, 76, 87, 102]. This change in conductance stops when the adsorption and desorption of oxygen molecules are in equilibrium. When nanotube devices are annealed at elevated temperature in UHV, more oxygen is desorbed, and the hole conduction is eventually completely suppressed with large enhancement of electron conduction. This polarity change is employed to measure the scattering strength of a potassium atom for both holes and electrons.

At room temperature, the device current has an ohmic, linear dependence on the bias voltage (linear I-V). However, the I-V curve becomes non-linear at low temperature, forming a transport

gap. Sufficiently large bias voltage needs to be applied to overcome the transport gap. The simple Ohm's law is not applicable to find conductance in this case since I-V curves are not linear. The technique to measure the conductance of non-linear I-V dependence is discussed in the next section.

6.2.3 Measurement technique

The conductance, which is a slope of I-V curves, is not constant when I-V curves are non-linear. As such, a differential conductance, *dI/dV*, needs to be measured. It is performed by adding a small AC bias voltage (*dV*) on a DC bias voltage and reading only an AC current signal (*dI*). Figure 6.2 shows the method to add a small AC voltage to a DC voltage. The AC bias voltage is divided into a small AC bias (*dV*) through 100 kΩ and 100 Ω resistors (1000 to 1), and the DC bias is divided through 10 kΩ and 100 Ω resistors (100 to 1). Since these two voltage dividers share the same 100 Ω resistor, the divided voltages add up on the 100 Ω resistor. The resistor is chosen to be much smaller than the resistance of nanotubes (typically > 10 kΩ) in order to reduce the interference with the measurement. A lock-in amplifier is used to apply an AC voltage and measure an AC current. However, the lock-in amplifier has 1 kΩ of input impedance, which is comparable with the nanotube resistance. As such, the current signal is first amplified with a preamplifier with small input impedance (< 200 Ω). Only the AC current signal (*dI*) is then picked up by the lock-in amplifier. The source *dV* and the measured *dI* are used to calculate the differential conductance *dI/dV*.

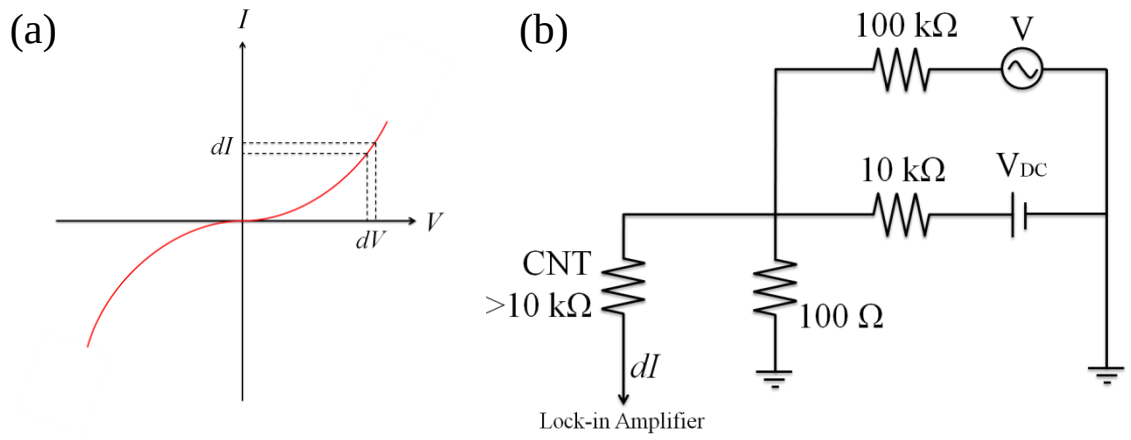

Figure 6.2: (a) The measurement of the differential conductance with a non-linear I-V curve. (b) Schematic of the voltage addition.

6.2.4 Potassium flux measurement with QCM

Potassium atoms are deposited using alkali metal dispensers (SAES). An electric current larger than 6 A is passed to thermally activate the dispensers with Joule heating. A flux of potassium atoms is released from the dispensers by reducing potassium salt to potassium atoms during the heating process. The number of potassium atoms coming onto carbon nanotubes can be calculated if the flux of potassium atoms is known; multiply the flux by the exposure time and the area of a carbon nanotube. The exposure time is controlled by the shutter immediately below a device, and the effective area of carbon nanotubes is their diameter × length. The diameter is calculated with equation (2.18). Alkali metal dispensers release a different amount of flux each time they are activated, and the flux is also far from being isotropic. As such, a flux of potassium is measured by quartz crystal microbalance (QCM).

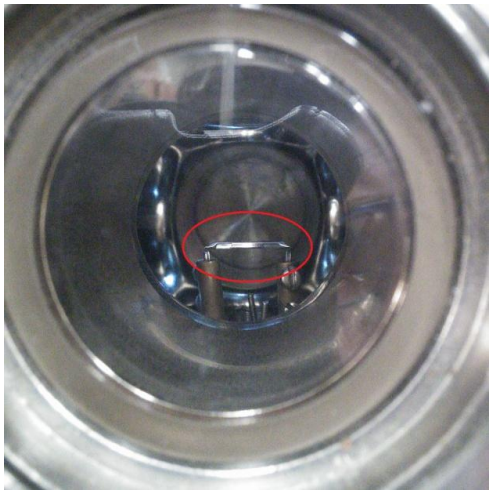

Figure 6.3: An alkali metal dispenser in an UHV chamber. The electrodes extend outside of the chamber to pass current through the dispenser.

QCM is widely used in metal deposition chambers to monitor the thickness of evaporants. QCM is driven to oscillate at a resonant frequency. This frequency changes once mass is added on the surface of the crystal, and the frequency change has dependence on the amount of the mass added. This relation is described by Sauerbrey equation,

$$\Delta f_0 = -2.26 \times 10^{-6} n t f_0^2 \qquad (6.3)$$

where f_0: the characteristic frequency of quartz crystal (6 MHz), n: density(g/cm^3) of the material added on QCM, and t: thickness (cm) of the material. The density of potassium, 0.862 g/cm^3, is used. The thickness of a film of potassium on the QCM is then calculated by measuring the change in the characteristic frequency as a film of an evaporant is formed on QCM. The frequency change of at least 1 Hz is needed to reliably measure the thickness. In the case of

potassium, this corresponds to the thickness of 1.42 Å, which is attainable with alkali metal dispensers.

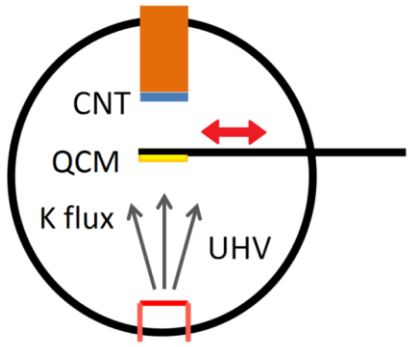

Figure 6.4: Schematic of the QCM measurement. The QCM is placed between the device and the alkali metal dispenser.

However, QCM is sensitive to temperature change, and it causes a frequency to drift. Even a temperature difference of 0.1 °C corresponds to the frequency change comparable with 1 Hz, and it obscures interpretation of the frequency change into a flux of potassium. In fact, the radiation from the dispenser heats up the QCM to cause the thermal frequency drift. The thermal drift can be reduced within ± 0.01 Hz of change when water cooling is incorporated into a QCM system. A flow of water keeps the QCM in thermal equilibrium (the equilibrium temperature varies depending on the power of thermal radiation from the dispenser). The temperature of the cooling water itself may vary over time depending on the condition of a building water system, but it is possible to stabilize the frequency by controlling the flow rate of the cooling water.

The flux of potassium is determined immediately before exposing a device to the flux. Figure 6.5 shows a typical frequency change during the measurement of a potassium flux. Initially the current through the dispenser is kept at 2.0 A, well below the activation current of the dispenser. The current is increased to 5.0 A at t = 300 seconds. The frequency increases immediately after the current is increased because of the radiation heating from the dispenser.

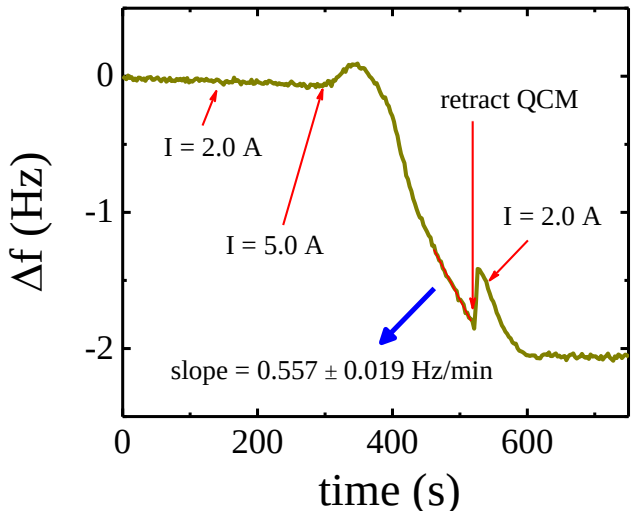

Figure 6.5: Frequency change of QCM as a function of time.

When it reaches thermal equilibrium, the frequency starts decreasing due to the flux of potassium atoms coming onto the surface of the QCM. The QCM is mechanically retracted once the rate of change in the frequency becomes constant. In this particular case, the rate of change immediately before retracting the QCM is 0.557 ± 0.0019 Hz/min, and it is converted to the flux using the equation (6.3), molar mass of potassium, and the Avogadro constant;

$$J[atom/cm^2 \cdot s] = \frac{N_A \cdot \Delta f_0[Hz/min]}{60M \cdot 2.26 \times 10^{-6} \cdot f_0^2} = 1.23 \times 10^{14} \cdot \frac{\Delta f_0[Hz/min]}{M} \qquad (6.4)$$

calculated from the slope of a linear fit immediately before retracting the QCM. The shutter is opened for the period of time needed to have a specific number of potassium atoms.

In our measurement system, the QCM is positioned half way between a device and the dispenser. The geometric factor which is required to calculate the density of potassium at the device position is separately measured using the same QCM. Simple geometric conversion based on the distance is not applicable since the flux is not isotropic. We have found the empirical geometric factor by using the position manipulator and changing the distance of the dispenser and the QCM. We found that the geometric factor is 0.11 ± 0.02.

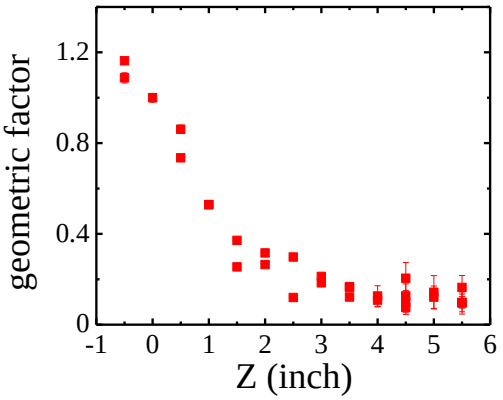

Figure 6.6: Measurement of the geometric factor.

6.3 Potassium dosing experiment on a (7,6) nanotube

6.3.1 The comparison of conductance in the air and in vacuum at room temperature

Semiconducting carbon nanotubes usually display conductance in the air only when the gate voltage induces holes in nanotubes. In vacuum, however, the conductance can also be carried by electrons and shows an ambipolar behavior. This change is clearly observed for the conductance measurement of a (7,6) semiconducting carbon nanotube at room temperature, as shown in Figure 6.7. In the air, the device turns on when the gate voltage is in the negative voltage side (hole conduction). Only up to ±10 V of gate voltage is applied in order to avoid shorting the gate electrode to the nanotube. The device has a hysteresis effect which depends on the direction of the gate voltage sweep. The red (blue) curve is the conductance when the gate voltage is swept up (down). The hysteresis comes from a charge trap within the oxide layer as the gate voltage is varied. When the device is placed in UHV, finite conductance also appears in the positive voltage side (electron conduction).The hysteresis effect is pronounced with the larger gate voltage applied, and either hole or electron conduction is displayed more in detail, depending on the direction of the gate voltage sweep. The hole conduction in UHV becomes suppressed as the electron conduction increases. This enhancement and suppression of conductance is discussed in section 6.2.2.

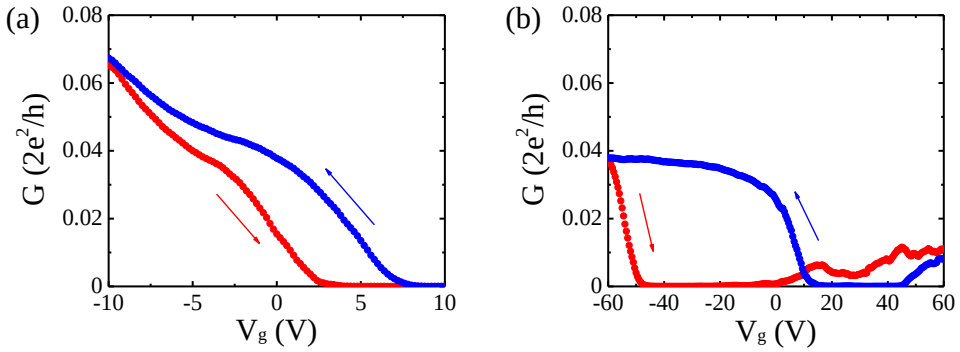

Figure 6.7: Conductance as a function of gate voltage (a) in the air and (b) in UHV.

6.3.2 Low temperature potassium dosing experiment for hole conduction

The conductance of the same (7,6) nanotube is measured in UHV at 10 K (Figure 6.8). I-V curves are non-linear at low temperature, and the conductance is measured at sufficiently high source-drain bias voltage where the device current is linearly dependent on the bias voltage. The hole conduction is increased as temperature is lowed. The electron conduction is, on the other hand, slightly reduced because of the increase in the transport gap. We define V_{onset} as the gate voltage at which the conductance starts increasing when plotted in a log scale, as in Figure 6.8b. This onset voltage corresponds to the beginning of the valence band conduction in semiconducting nanotubes. Since the electron conduction is much more resistive than the hole conduction, we focus our attention on the conductance obtained when the gate voltage is swept down.

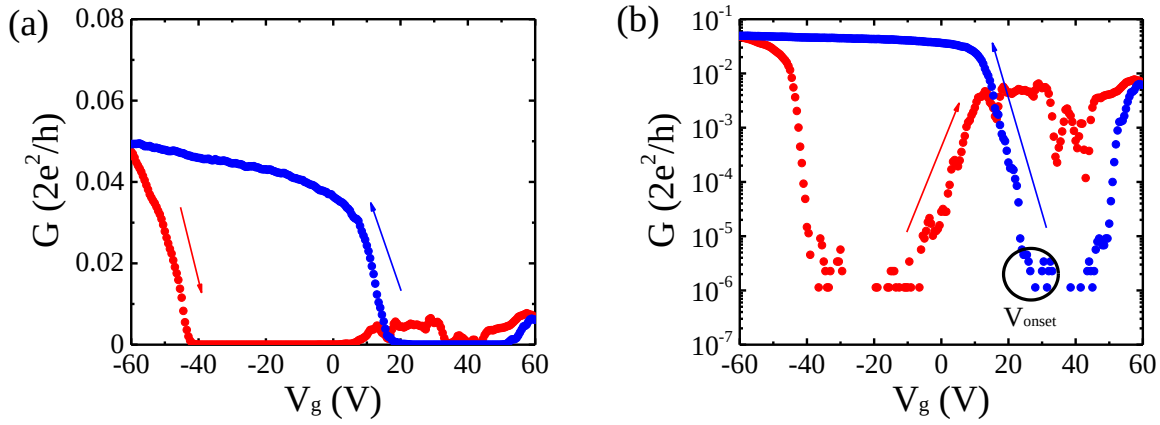

Figure 6.8: Conductance as a function of gate voltage in UHV at T = 10 K. The y-axis scale is (a) linear and (b) log10.

In Figure 6.9, the conductance is plotted for different segment length. Before introduction of potassium atoms, all the segments show ambipolar conductance with enhanced hole conduction and the onset voltage from each segment is located close to one another. When potassium atoms are added on the nanotube, the hole conduction suppresses for all the segments, and the electron conduction is slightly enhanced for some segments. The number of potassium atoms is determined using QCM as discussed in section 6.2.4.

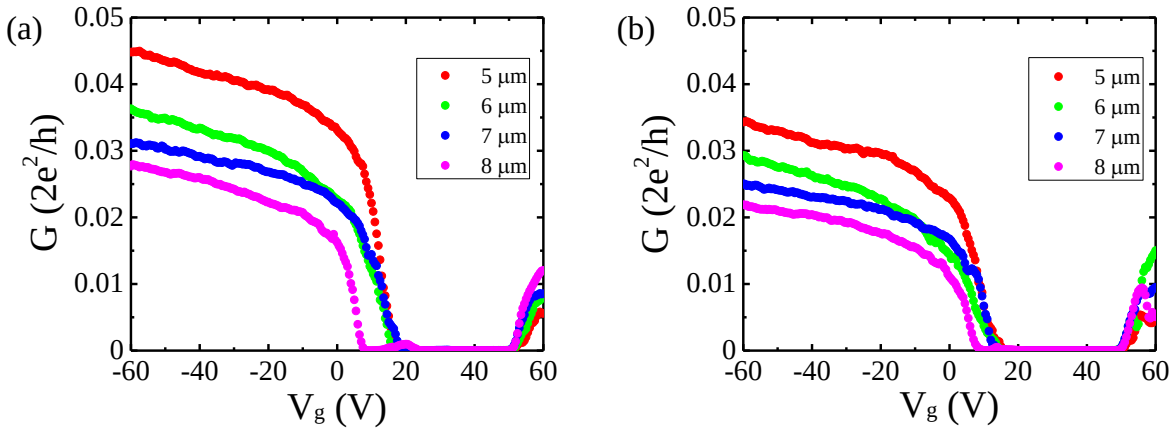

Figure 6.9: Conductance as a function of gate voltage for the (7,6) semiconducting carbon nanotube in UHV at 10 K (a) before the introduction of potassium and (b) after the introduction of potassium. It shows ambipolar conductance. The hole conduction (negative gate voltage side) is much larger than the electron conduction (positive gate voltage side).

The impact of potassium atoms on the resistivity of the (7,6) nanotube is determined by plotting the resistance as a function of nanotube length. Figure 6.10 shows the length dependence of resistance –60 V away from the onset gate voltage ($V_g - V_{onset}$ = –60 V). From the density of states (DOS) of a (7,6) carbon nanotube, $V_g - V_{onset}$ = –60 V corresponds to E = –1.5 eV of the nanotube, which is in the second sub-band. The conversion from the gate voltage to energy is done by

$$\frac{\mu}{e} + \frac{q}{c_g} = V_g \qquad (6.5)$$

where the first term is quantum capacitance, and the second term is geometric capacitance. From a linear fit analysis, the resistivity before the addition of potassium is ρ_0 = 57.7 ± 2.0 kΩ/µm, and

it changes to ρ = 79.6 ± 1.6 kΩ/μm, with $\Delta\rho$ = 21.9 ± 2.9 kΩ/μm. This leads to the scattering strength of 10.0 ± 1.4 kΩ/atom with 2.2 ± 0.1 atom/μm of potassium atoms.

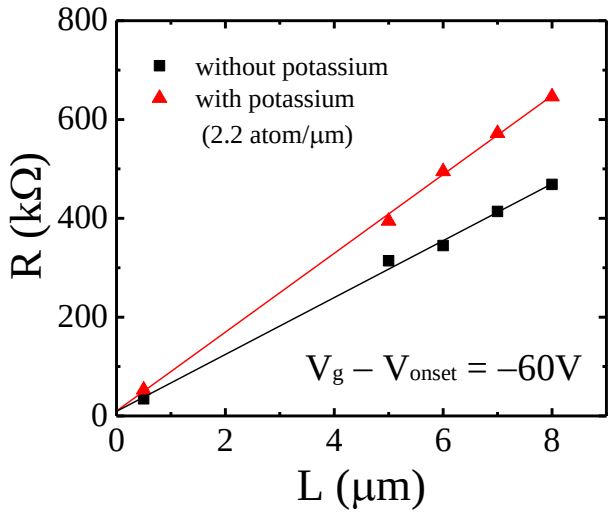

Figure 6.10: Resistance as a function of carbon nanotube length. The slope corresponds to the resistivity of the nanotube itself.

6.3.3 Low temperature potassium dosing experiment for electron conduction

Once the potassium dosing experiment is completed for the hole conduction, the device is annealed in UHV at 460 K for a couple of days. This effectively removes potassium atoms from the nanotube surface [103]. Furthermore, the annealing also depletes oxygen from the contact-nanotube interface, and the device now shows finite conductance when gate voltage is in the positive side (electron conduction), as shown in Figure 6.11. Potassium now suppresses the electron conduction rather than enhancing it, showing that the channel resistance is dominating the change in the contact resistance. These measurements show that two-probe conductance

measurements are insufficient for revealing the impact of potassium on the resistivity of nanotubes.

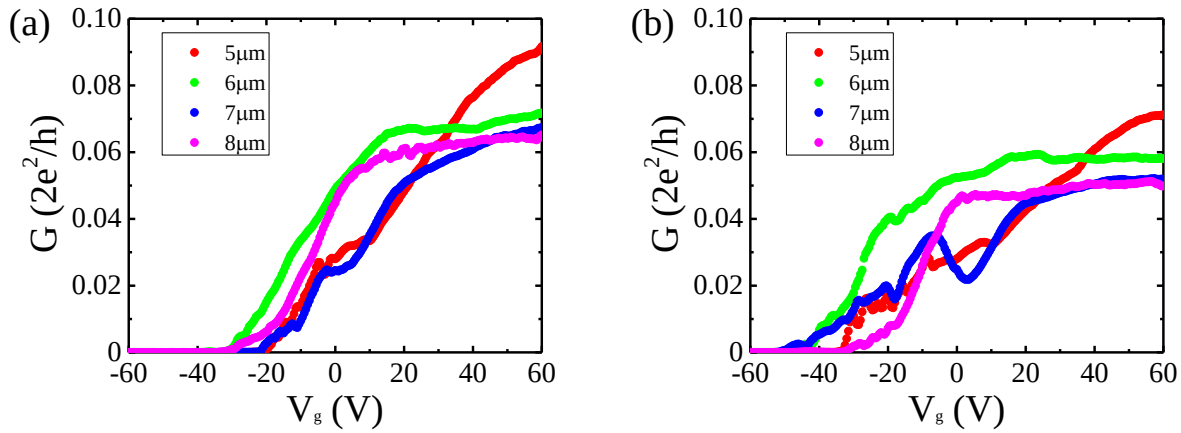

Figure 6.11: Conductance as a function of gate voltage in UHV at T = 12 K. (a) Before addition of potassium. (b) After addition of potassium.

The impact of potassium on the resistivity of the nanotube for electron conduction can be determined in the same way as in the case of holes. Figure 6.12 shows the length dependence of resistance at $V_g - V_{onset}$ = +60 V. The contact resistance shows almost no change. The resistivity before addition of potassium is ρ_0 = 17.0 ± 1.6 kΩ/μm, and, ρ = 23.5 ± 1.7 kΩ/μm after adding 29.6 ± 0.4 atom/μm of potassium atoms, with $\Delta\rho$ = 6.5 ± 2.3 kΩ/μm. This leads to the scattering strength is 0.22 ± 0.08 kΩ/atom.

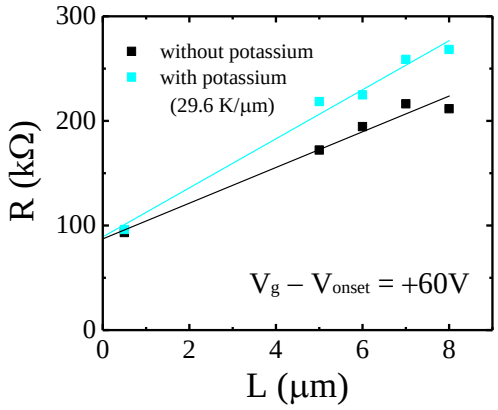

Figure 6.12: Resistance as a function of nanotube length for electron conduction.

6.3.4 Determination of the scattering strength for holes and electrons

The resistivity increases linearly with the density of potassium, showing that potassium behaves as diffusive and uncorrelated scatterers even at maximum density of 3 atoms/μm for the hole conduction and 30 atoms/μm for the electron conduction (Figure 6.13). Such adherence of the observation to diffusive, semi-classical picture is consistent with the phase coherence length of nanotubes being less than 100 nm for temperature above 10 K. Furthermore, the linear dependence on the deposited density also indicates that increased concentration of potassium does not lead to clustering. From the linear fit, the scattering strength of potassium is found to be 8.2 ± 1.3 kΩ/atom for holes and 0.22 ± 0.03 kΩ/atom for electrons. Interestingly, a potassium atom scatters holes 37 times more than electrons.

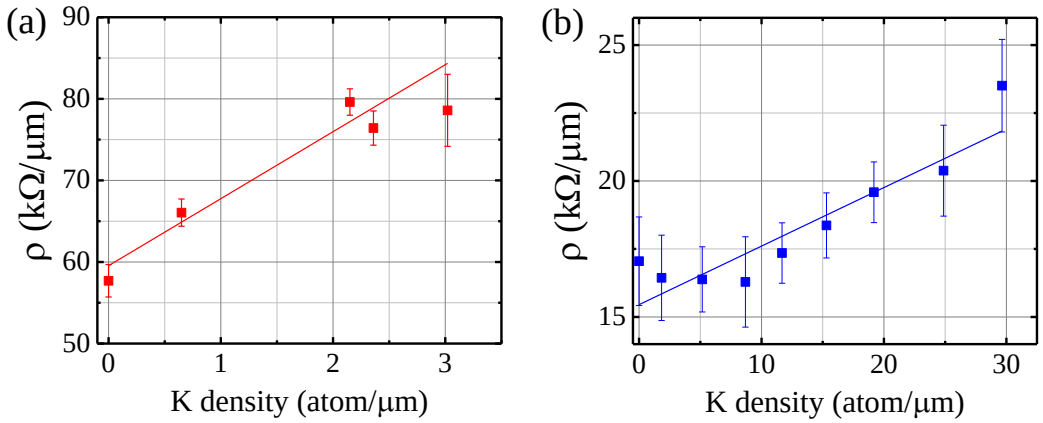

Figure 6.13: Resistivity change as a function of potassium atom density for (a) holes and (b) electrons.

6.3.5 Numerical simulation

The electron-hole asymmetry of the scattering strength observed in the experiments is consistent with numerical transport calculations performed on a (7,6) nanotube, using a recursive Green's function method. Starting from a clean, single-band, tight-binding model, we randomly added Gaussian scattering potentials of the form $V_i(\boldsymbol{R}) = V_0 \exp[-|\boldsymbol{R}-\boldsymbol{R}_i|^2/\xi^2]$, where $\boldsymbol{R}_i$ denotes the scatterer's lattice location, V_0 is the (positive) scatterer strength, and ξ represents the scattering potential range. The zero-temperature linear conductance is then evaluated using the Landauer-Büttiker formula and averaged over 200 random samples to wash away fluctuations due to phase-coherent interference. For large scatterer concentrations, short nanotubes are used to keep carriers in the diffusive regime and avoid Anderson localization.

Figure 6.14 shows the result of the analysis of numerical data similar to that presented in Figure 6.10 and 6.12 for the experimental data, with the Fermi energy fixed at $E = \pm 1.5$ eV and impurity potential parameters ξ = 20 Å and V_0 = 1.1 eV. These parameter values are found to produce the closest results to those obtained in the experiments. In particular, the asymmetry between the hole and electron resistivities depends on ξ and on the Fermi energy E and is maximal for the values we adopted. The resulting strength of each scatterer, as measured by their effect on the nanotube resistivity is 7.7 ± 0.2 kΩ/scatterer for holes and 0.28 ± 0.01 kΩ/scatterer for electrons.

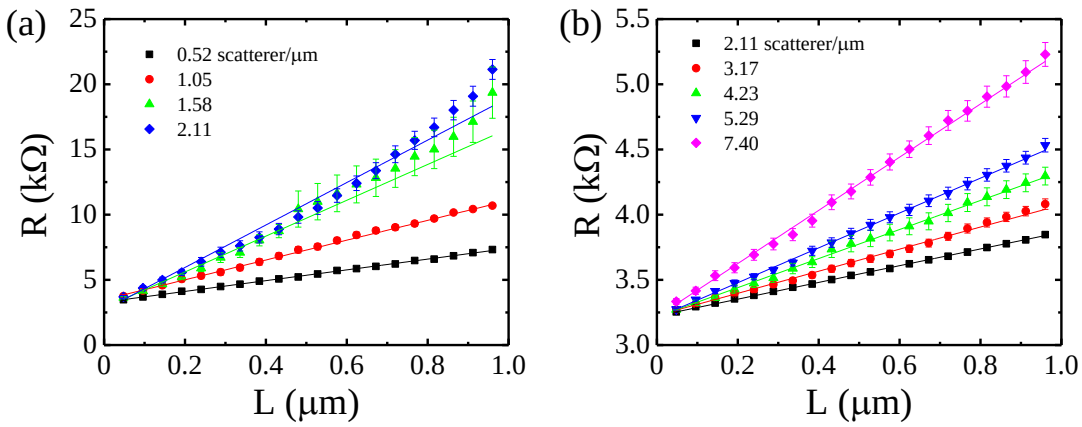

Figure 6.14: Simulation of resistance as a function of nanotube length with different impurity density for (a) holes and (b) electrons.

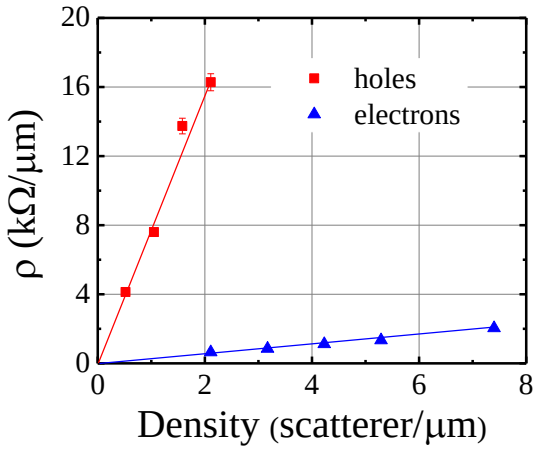

Figure 6.15: Simulation of the scattering strength for holes and electrons.

The experimental electron-hole asymmetry with holes being scattered more efficiently than electrons is reproduced by our theoretical calculation with atomic scale fidelity to the experiment. The simplest explanation of the origin of the asymmetry is the difference in the potential landscape for electrons and holes. Our result is the first measurement of the scattering strength of an individual adsorbate on semiconducting nanotubes.

6.4 Low temperature measurement on (22,4) metallic nanotube

The scattering strength of a potassium atom on metallic carbon nanotubes is determined in the same way as in the (7,6) semiconducting nanotube. Most of our metallic nanotubes display anomalous conductance suppression as a function of the gate voltage, which makes the analysis of resistivity difficult. A similar conductance behavior is reproduced by our numerical simulation with the recursive Green's function method, and it provides an interpretation of the conductance

suppression in our metallic carbon nanotubes. The scattering strength of a potassium atom in the experiment is found by a comparison with this theoretical simulation.

6.4.1 Anomalous conductance suppression in metallic carbon nanotubes

Atomically clean, metallic carbon nanotubes usually have ambipolar conductance with a finite suppression of conductance, as shown in Figure 6.16a. Most of the metallic carbon nanotubes are so-called quasi-metallic nanotubes because of a curvature-induced band gap (< 100 meV), and the zero-gap metallic nanotubes are realized only for armchair nanotubes [104]. The finite suppression of conductance has been naively attributed to the curvature-induced band gap, though some studies suggest that the conduction dip is a manifestation of Mott insulating state [105] or a substrate induced inhomogeneity of Fermi energy [106].

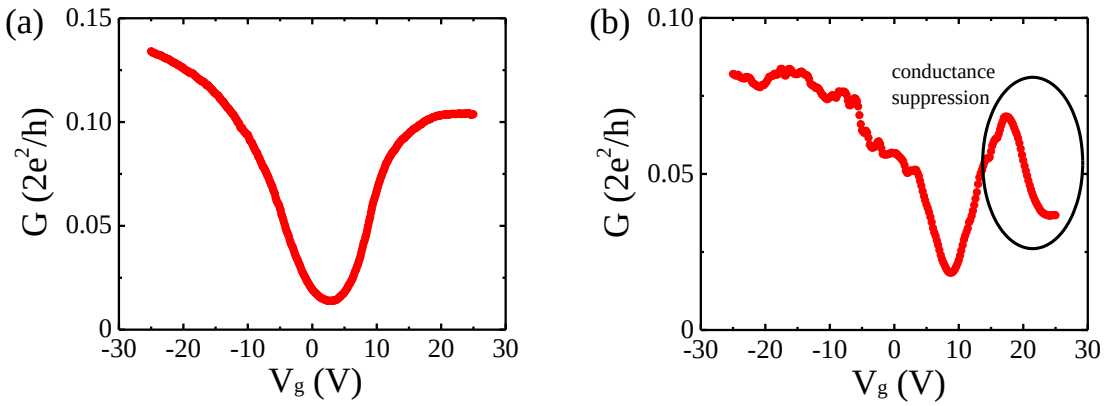

Figure 6.16: Comparison of (a) a normal metallic nanotube and (b) the one with anomalous conductance suppression.

In our experiment, extra conductance suppression has been observed when a large gate voltage is applied. The conductance normally increases monotonically from the minimum conduction point and tends to saturate toward a larger gate voltage side. However, the conductance in our metallic nanotube devices starts decreasing to form a hump shape as the gate voltage is increased. Figure 6.17 shows the conductance of a (22,4) metallic carbon nanotube at room temperature. The anomalous conductance suppression on the positive gate voltage side is present regardless of the nanotube length. I-V curves are linear in all segments, showing that a contact effect is not responsible for the suppression of conductance. This is further confirmed when the conductivity of the nanotube is calculated from the linear fit to a resistance vs. length plot (Figure 6.18).

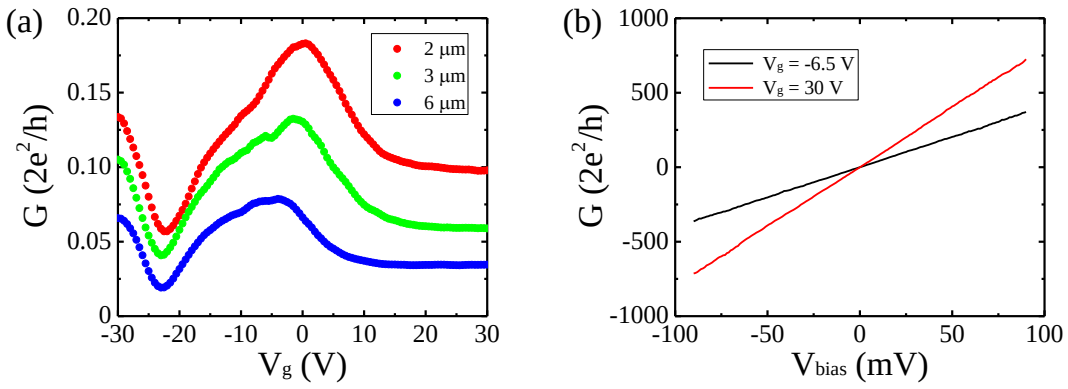

Figure 6.17: The electronic transport measurement of the (22,4) metallic carbon nanotube in UHV at room temperature measurement. (a) Conductance vs. gate voltage shows the hump shape in all segments. (b) I-V curves of each segment measured at V_g = 30 V. All the segments show linear dependence.

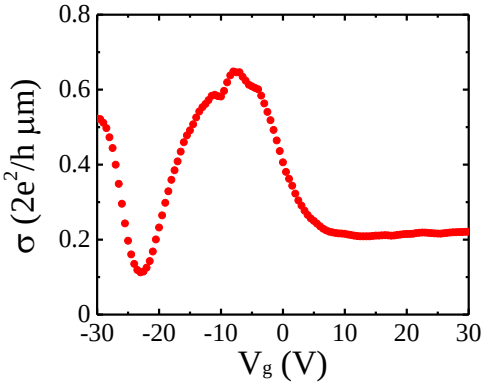

Figure 6.18: Conductivity of the (22,4) nanotube calculated from linear fit to resistance vs. length plots. The hump shape is still present.

In order to find the cause for the formation of the hump, we convert the gate voltage into chemical potential in the same way as in the (7,6) semiconducting nanotube case. Using the same parameters, we find ±12.3 V of the gate voltage corresponds to the first van Hove singularities of a (22,4) nanotube and $|V_g| < 30$V corresponds to $|E| < 0.8$ eV, which includes up to the third sub-band. The quantum capacitance is negligible because the band gap is 11 meV [104]. The conductance of a (22,4) metallic carbon nanotube is compared with our numerical simulation with varying impurity density in the same energy rage as in the experiment.

Figure 6.19 shows how the conductance is affected by the presence of impurities. In this simulation, positive local potentials of amplitude 1.1 eV and range 18 Å are used. The DOS of the (22,4) nanotube is superimposed on the same plot to show the location of van Hove singularities. The conductance is $G = 4e^2/h$ in the first sub-band if no impurity is present. However, the conductance is smaller than $G = 4e^2/h$ due to the scattering caused by the positive

impurity potentials. The conductance shows its peak at the edge of the first sub-band (E = –0.61 eV) and decreases toward the positive energy side within the first sub-band. The conductance minimum occurs in the vicinity of the van Hove singularity at E = 0.61 eV regardless of the impurity density. The hole charge carriers (negative energy) is more resilient to positive scatterers than electron charge carriers (positive energy), and the contrast of the conductance at van Hove singularities (E = ±0.61 eV) is striking. The conductance also shows opposite trends beyond the first sub-band (E > |0.61| eV). Interestingly, the conduction at energy above van Hove singularities becomes smaller than that of first sub-band even though charge carriers also start conducting in the second sub-band. This indicates that extra scattering events from the first to the second sub-bands reduce the conductance in the first sub-band, and the conservation of pseudospin is no longer effective.

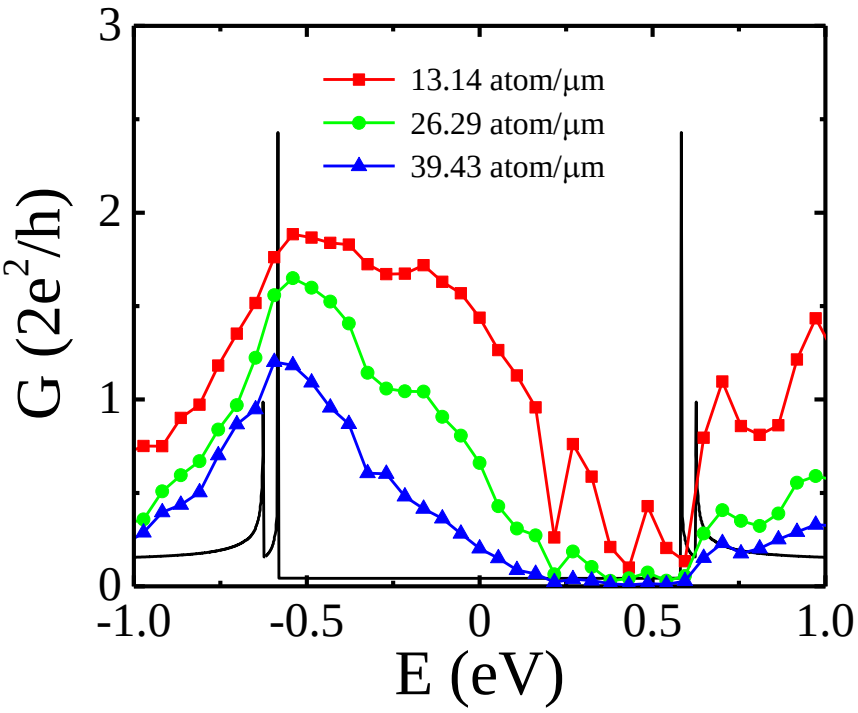

Figure 6.19: Simulation of the conductance of a (22,4) metallic nanotube. DOS is superimposed for the aid. As the density of impurities increases the suppression of conductance occurs.

The position of the conductance peak will be shifted toward the middle of the first sub-band if there is a mixture of positive and negative charged impurities, as negative impurities reduce the conductance on the negative energy side. The suppression of the conductance on the electron conduction is qualitatively similar to the experiment. This similarity suggests that the conductance suppression occur due to positively charged impurities and the hump top be located in the first sub-band. This picture is supported by the fact that the hole resistivity of the (7,6) nanotube is greater than that of electrons, i.e., there are more positively charged impurities on the

surface of the substrate. If the hump top is in the first sub-band, the change in the conductance is expected to be smaller at the hump top upon introduction of potassium atom.

6.4.2 Low temperature measurement

Figure 6.20 shows the conductance of 2 μm, 3 μm, and 6 μm segments as a function of gate voltage in UHV at T = 12 K. The hump shape is still present at low temperature. Though I-V curves are non-linear at this temperature, the source-drain bias voltage is large enough to be in the linear regime of the I-V curves (80 mV for 2 μm segment, 90 mV for 3 μm and 6 μm segments). Once potassium atoms are introduced, the curves shift to the negative gate voltage side, as potassium atoms donate partial electrons to the nanotube. The number density is 1.8 ± 0.1 atom/μm. The width of the hump becomes smaller for each segment with potassium being present. The impact of potassium atoms on the conductivity is shown in Figure 6.21. The maximum conductance shows only a slight decrease, but the conductance is suppressed away from the hump top upon the addition of positively charged potassium, which is consistent with our theoretical simulation. The emerging local minimum around V_g = –3 V indicates that a van Hove singularity is located in this region. The energy dependence of the scattering strength is revealed when the resistivity is plotted instead of conductivity (Figure 6.21b). The resistivity change at the hump top is $\Delta\rho$ = 2.7 ± 3.7 kΩ, leading to the scattering strength of 1.5 ± 2.1 kΩ/atom. This is approximately 5 times smaller than the scattering strength of 8.2 ± 1.3 kΩ/atom for the hole conduction in the (7,6) semiconducting nanotube.

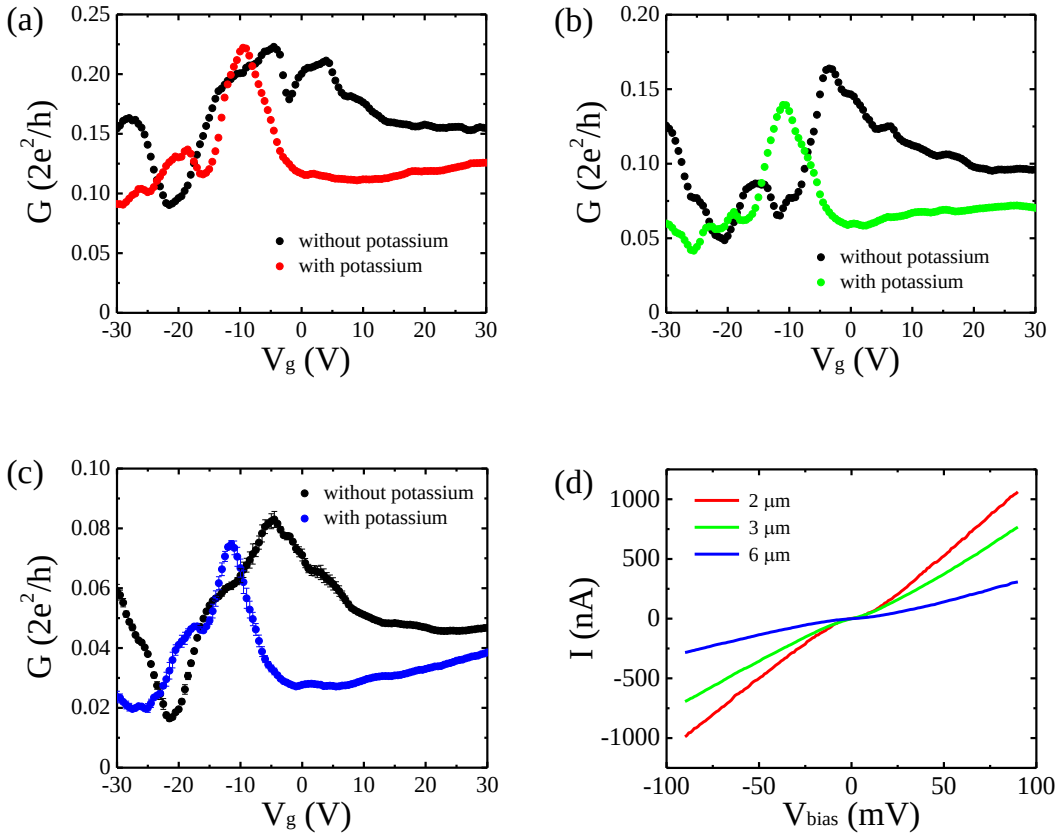

Figure 6.20: Conductance of the (22,4) metallic carbon nanotube in UHV at T = 12 K. (a) 2 μm, (b) 3 μm, (c) 6 μm, and (d) I-V curves.

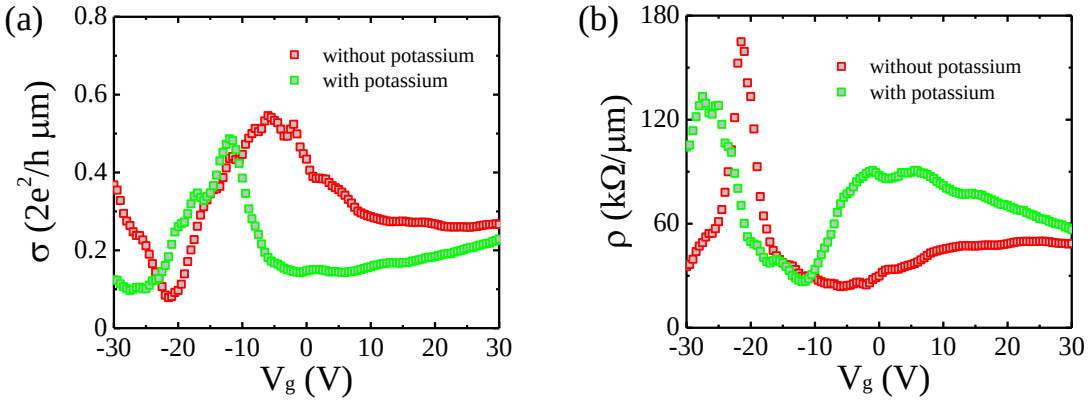

Figure 6.21: (a) Conductivity and (b) resistivity of the (22,4) nanotube.

Metallic nanotube being resilient to long-range impurities is consistent with the pseudospin conservation conjecture. The error on the scattering strength for the metallic nanotube is large, and further experiment to confirm the value is necessary. Nevertheless, it shows that the impact of a single potassium atom on the metallic nanotube is small. This is the first direct experimental observation of the pseudospin conservation in metallic carbon nanotubes. Though scattering strength is expected be smaller in metal in general because of a charge screening effect, the charge screening in one dimensional conductors is not effective. Furthermore, the large increase of the resistivity immediately away from the hump top is contradictory with the screening effect.

6.5 Conclusion on the pseudospin conjecture

We have measured the scattering strength of a potassium atom on (7,6) metallic and (22,4) semiconducting carbon nanotubes. The (7,6) semiconducting carbon nanotube has an asymmetric scattering strength depending on the charge carrier types, holes being scattered more than electrons. This asymmetry is explained by the transmission probability of a simple square potential barrier or potential well. The (22,4) metallic nanotube displays anomalous conductance suppression, and the comparison to our theoretical simulation with the recursive Green's function method in the tight-binding model shows that the suppression of the conductance is related to van Hove singularities and the hump top is located in the first sub-band, in which the suppression of backscattering is effective due to the conservation of pseudospin. It is found that metallic carbon nanotubes are approximately 5 times more resilient to a Coulomb potential than

semiconducting carbon nanotubes, showing the effect of pseudospin conservation in metallic carbon nanotubes.

Table 6.1: The scattering strength of a single potassium atom on carbon nanotubes

Chirality	Type	Scattering strength (kΩ/μm)
(7,6)	semiconducting (holes)	8.2 ± 1.3
(7,6)	semiconducting (electrons)	0.22 ± 0.03
(22,4)	metallic	1.5 ± 2.1

APPENDIX: TEMPERATURE REQUIRED TO LOCK POTASSIUM ATOMS ON NANOTUBES

Devices are cooled down by extracting heat from the devices with a flow of liquid helium. The temperature can be as low as 10 K when the devices are in thermal equilibrium. However, the temperature of the devices may increase by Joule self-heating when a large current is passed through the devices. It is necessary to keep the temperature of the devices lower than 20 K in order to prevent potassium atoms from diffusing. The thermal conductivity of carbon nanotubes depends on the temperature, and it becomes small below 20 K; the heat dissipation along nanotubes into contact is not efficient (citation). Fortunately, heat can be dissipated directly into the substrate on which nanotubes are placed (citation). The effect of Joule self-heating on the temperature of nanotube is experimentally measured for semiconducting nanotubes. Owing to a finite energy gap, I-V curves of semiconducting nanotubes reveal a non-linear relation at low temperature, forming a transport gap. The size of the transport gap has temperature dependence, and it is used as a measure of temperature.

First the threshold gap size at 20 K is needed to be determined as a reference to the temperature. This can be tested by scan in a small range of bias voltage. Figure B.1 shows I-V curves of a 5 μm segment at 20 K. The current is measured 5 cycles (1 cycle is from 0 mV to –50 mV, –50mV to +50 mV, and +50 mV down to 0 mV), and the I-V curves from 5 cycles do not deviate from each other, meaning Joule heat (average of 0.9 nW) is completely dissipated within a cycle; if the heat dissipation is not enough and the temperature starts going up, it should be observable as the change in the gap size over multiple scans. When the bias voltage is applied up to ±100 mV twice as slow rate (average of 4.67 nW), the shape of the curve is still the same as in the case of the ±50 mV. Thus, the difference of 3.77 nW or 0.75 nW/μm sets a lower limit of the heat

dissipation from the nanotube. This limit is larger than the Joule heat generated when ±50 mV is applied, i.e., the shape of the I-V curve can be used as a reference to T = 20 K. If the temperature of nanotube increases above 20 K, the gap should become smaller than this reference gap. If the temperature is below the reference gap, then, the temperature of the nanotube is below 20 K.

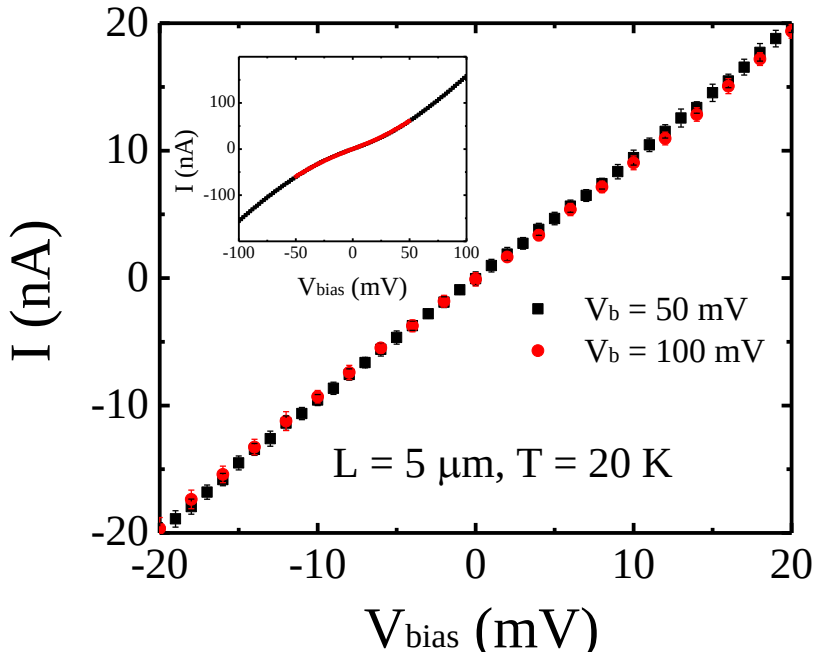

Figure A.1: I-V curve of carbon nanotube at low temperature

The same test is also carried out at T = 10 K. A large bias voltage (> 100 mV) needs to be applied at low temperature in order to measure the differential conductance in the linear I-V regime. This results in large Joule heating. Figure B.2 shows the comparison of I-V curves at T = 10 K and 20 K. The gap size is larger at T = 10 K, regardless of the scan rate, and the

accumulation of heat is not observed, concluding that the temperature remains at T = 10 K for the entire time during the measurement.

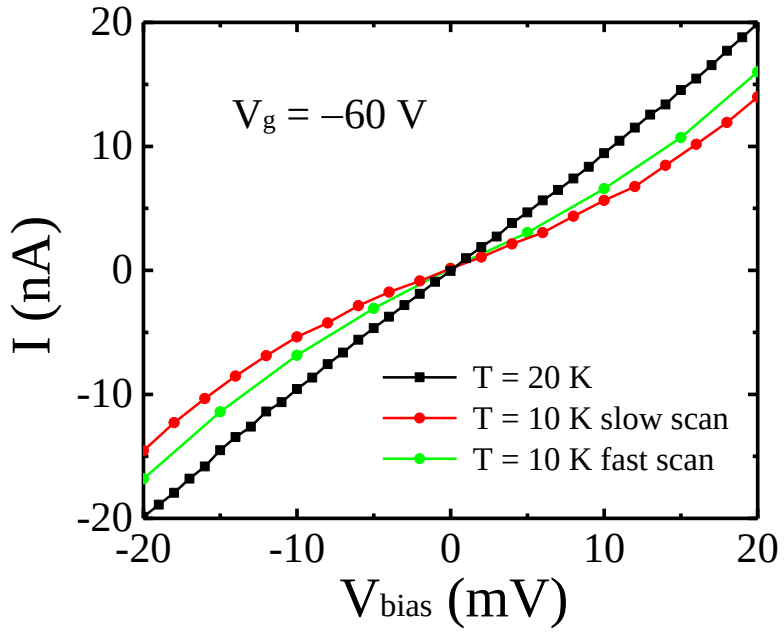

Figure A.2: Temperature dependence of the transport gap size at V_g = –60V.

LIST OF REFERENCES

[1] S. Iijima, Helical Microtubules of Graphitic Carbon, Nature, 354 (1991) 56-58.

[2] H.W. Kroto, J.R. Heath, S.C. Obrien, R.F. Curl, R.E. Smalley, C-60 - Buckminsterfullerene, Nature, 318 (1985) 162-163.

[3] K.S. Novoselov, A.K. Geim, S.V. Morozov, D. Jiang, Y. Zhang, S.V. Dubonos, I.V. Grigorieva, A.A. Firsov, Electric field effect in atomically thin carbon films, Science, 306 (2004) 666-669.

[4] M.F.L. De Volder, S.H. Tawfick, R.H. Baughman, A.J. Hart, Carbon Nanotubes: Present and Future Commercial Applications, Science, 339 (2013) 535-539.

[5] S. Berber, Y.K. Kwon, D. Tomanek, Unusually high thermal conductivity of carbon nanotubes, Phys Rev Lett, 84 (2000) 4613-4616.

[6] P. Kim, L. Shi, A. Majumdar, P.L. McEuen, Thermal transport measurements of individual multiwalled nanotubes, Phys Rev Lett, 87 (2001).

[7] A. Javey, J. Guo, Q. Wang, M. Lundstrom, H.J. Dai, Ballistic carbon nanotube field-effect transistors, Nature, 424 (2003) 654-657.

[8] M.F. Yu, O. Lourie, M.J. Dyer, K. Moloni, T.F. Kelly, R.S. Ruoff, Strength and breaking mechanism of multiwalled carbon nanotubes under tensile load, Science, 287 (2000) 637-640.

[9] E. Artukovic, M. Kaempgen, D.S. Hecht, S. Roth, G. GrUner, Transparent and flexible carbon nanotube transistors, Nano Lett, 5 (2005) 757-760.

[10] D.M. Sun, M.Y. Timmermans, Y. Tian, A.G. Nasibulin, E.I. Kauppinen, S. Kishimoto, T. Mizutani, Y. Ohno, Flexible high-performance carbon nanotube integrated circuits, Nat Nanotechnol, 6 (2011) 156-161.

[11] S. Jang, B. Kim, M.L. Geier, P.L. Prabhumirashi, M.C. Hersam, A. Dodabalapur, Fluoropolymer coatings for improved carbon nanotube transistor device and circuit performance, Appl Phys Lett, 105 (2014).

[12] P.C. Chen, Y. Fu, R. Aminirad, C. Wang, J.L. Zhang, K. Wang, K. Galatsis, C.W. Zhou, Fully Printed Separated Carbon Nanotube Thin Film Transistor Circuits and Its Application in Organic Light Emitting Diode Control, Nano Lett, 11 (2011) 5301-5308.

[13] M.J. Ha, Y. Xia, A.A. Green, W. Zhang, M.J. Renn, C.H. Kim, M.C. Hersam, C.D. Frisbie, Printed, Sub-3V Digital Circuits on Plastic from Aqueous Carbon Nanotube Inks, Acs Nano, 4 (2010) 4388-4395.

[14] F.N. Ishikawa, H.K. Chang, K. Ryu, P.C. Chen, A. Badmaev, L.G. De Arco, G.Z. Shen, C.W. Zhou, Transparent Electronics Based on Transfer Printed Aligned Carbon Nanotubes on Rigid and Flexible Substrates, Acs Nano, 3 (2009) 73-79.

[15] S. Kaur, N. Raravikar, B.A. Helms, R. Prasher, D.F. Ogletree, Enhanced thermal transport at covalently functionalized carbon nanotube array interfaces, Nat Commun, 5 (2014).

[16] P. Jarosz, C. Schauerman, J. Alvarenga, B. Moses, T. Mastrangelo, R. Raffaelle, R. Ridgley, B. Landi, Carbon nanotube wires and cables: Near-term applications and future perspectives, Nanoscale, 3 (2011) 4542-4553.

[17] X. Wang, N. Behabtu, C.C. Young, D.E. Tsentalovich, M. Pasquali, J. Kono, High-Ampacity Power Cables of Tightly-Packed and Aligned Carbon Nanotubes, Adv Funct Mater, 24 (2014) 3241-3249.

[18] T. Sekitani, Y. Noguchi, K. Hata, T. Fukushima, T. Aida, T. Someya, A rubberlike stretchable active matrix using elastic conductors, Science, 321 (2008) 1468-1472.

[19] X.T. Wang, N.P. Padture, H. Tanaka, Contact-damage-resistant ceramic/single-wall carbon nanotubes and ceramic/graphite composites, Nat Mater, 3 (2004) 539-544.

[20] J. Cho, A.R. Boccaccini, M.S.P. Shaffer, Ceramic matrix composites containing carbon nanotubes, J Mater Sci, 44 (2009) 1934-1951.

[21] G.Y. Li, P.M. Wang, X.H. Zhao, Mechanical behavior and microstructure of cement composites incorporating surface-treated multi-walled carbon nanotubes, Carbon, 43 (2005) 1239-1245.

[22] H. He, L.A. Pham-Huy, P. Dramou, D.L. Xiao, P.L. Zuo, C. Pham-Huy, Carbon Nanotubes: Applications in Pharmacy and Medicine, Biomed Res Int, (2013).

[23] G.S. Hong, S. Diao, J.L. Chang, A.L. Antaris, C.X. Chen, B. Zhang, S. Zhao, D.N. Atochin, P.L. Huang, K.I. Andreasson, C.J. Kuo, H.J. Dai, Through-skull fluorescence imaging of the brain in a new near-infrared window, Nat Photonics, 8 (2014) 723-730.

[24] L. Bareket, N. Waiskopf, D. Rand, G. Lubin, M. David-Pur, J. Ben-Dov, S. Roy, C. Eleftheriou, E. Sernagor, O. Cheshnovsky, U. Banin, Y. Hanein, Semiconductor Nanorod-Carbon Nanotube Biomimetic Films for Wire-Free Photostimulation of Blind Retinas, Nano Lett, 14 (2014) 6685-6692.

[25] D. Jung, M. Han, G.S. Lee, Gas sensor using a multi-walled carbon nanotube sheet to detect hydrogen molecules, Sensor Actuat a-Phys, 211 (2014) 51-54.

[26] J.H. Lee, W.S. Kang, C.K. Najeeb, B.S. Choi, S.W. Choi, H.J. Lee, S.S. Lee, J.H. Kim, A hydrogen gas sensor using single-walled carbon nanotube Langmuir-Blodgett films decorated with palladium nanoparticles, Sensor Actuat B-Chem, 188 (2013) 169-175.

[27] P.G. Collins, K. Bradley, M. Ishigami, A. Zettl, Extreme oxygen sensitivity of electronic properties of carbon nanotubes, Science, 287 (2000) 1801-1804.

[28] L.F. He, Y. Jia, F.L. Meng, M.Q. Li, J.H. Liu, Gas sensors for ammonia detection based on polyaniline-coated multi-wall carbon nanotubes, Mater Sci Eng B-Adv, 163 (2009) 76-81.

[29] J.W. Han, B. Kim, J. Li, M. Meyyappan, A carbon nanotube based ammonia sensor on cellulose paper, Rsc Adv, 4 (2014) 549-553.

[30] K.H. Lee, V. Scardaci, H.Y. Kim, T. Hallam, H. Nolan, B.E. Bolf, G.S. Maltbie, J.E. Abbott, G.S. Duesberg, Highly sensitive, transparent, and flexible gas sensors based on gold nanoparticle decorated carbon nanotubes, Sensor Actuat B-Chem, 188 (2013) 571-575.

[31] Y. Zhang, S.M. Cui, J.B. Chang, L.E. Ocola, J.H. Chen, Highly sensitive room temperature carbon monoxide detection using SnO2 nanoparticle-decorated semiconducting single-walled carbon nanotubes, Nanotechnology, 24 (2013).

[32] M. Popescu, I.D. Simandan, F. Sava, A. Velea, E. Fagadar-Cosma, Sensor of Nitrogen Dioxide Based on Single Wall Carbon Nanotubes and Manganese-Porphyrin, Dig J Nanomater Bios, 6 (2011) 1253-1256.

[33] T. Alizadeh, F. Rezaloo, A new chemiresistor sensor based on a blend of carbon nanotube, nano-sized molecularly imprinted polymer and poly methyl methacrylate for the selective and sensitive determination of ethanol vapor, Sensor Actuat B-Chem, 176 (2013) 28-37.

[34] I. Sayago, M.J. Fernandez, J.L. Fontecha, M.C. Horrillo, C. Vera, I. Obieta, I. Bustero, New sensitive layers for surface acoustic wave gas sensors based on polymer and carbon nanotube composites, Sensor Actuat B-Chem, 175 (2012) 67-72.

[35] Y.S. Chien, W.L. Tsai, I.C. Lee, J.C. Chou, H.C. Cheng, A Novel pH Sensor of Extended-Gate Field-Effect Transistors With Laser-Irradiated Carbon-Nanotube Network, Ieee Electr Device L, 33 (2012) 1622-1624.

[36] D. Jung, M.E. Han, G.S. Lee, pH-sensing characteristics of multi-walled carbon nanotube sheet, Mater Lett, 116 (2014) 57-60.

[37] Y. Chen, S.C. Mun, J. Kim, A Wide Range Conductometric pH Sensor Made With Titanium Dioxide/Multiwall Carbon Nanotube/Cellulose Hybrid Nanocomposite, Ieee Sens J, 13 (2013) 4157-4162.

[38] T. Takahashi, K. Takei, A.G. Gillies, R.S. Fearing, A. Javey, Carbon Nanotube Active-Matrix Backplanes for Conformal Electronics and Sensors, Nano Lett, 11 (2011) 5408-5413.

[39] Z.G. Zhu, L. Garcia-Gancedo, A.J. Flewitt, H.Q. Xie, F. Moussy, W.I. Milne, A Critical Review of Glucose Biosensors Based on Carbon Nanomaterials: Carbon Nanotubes and Graphene, Sensors-Basel, 12 (2012) 5996-6022.

[40] Y.H. Lin, F. Lu, Y. Tu, Z.F. Ren, Glucose biosensors based on carbon nanotube nanoelectrode ensembles, Nano Lett, 4 (2004) 191-195.

[41] J.D. Huang, X.R. Xing, X.M. Zhang, X.R. He, Q. Lin, W.J. Lian, H. Zhu, A molecularly imprinted electrochemical sensor based on multiwalled carbon nanotube-gold nanoparticle composites and chitosan for the detection of tyramine, Food Res Int, 44 (2011) 276-281.

[42] A. Star, J.C.P. Gabriel, K. Bradley, G. Gruner, Electronic detection of specific protein binding using nanotube FET devices, Nano Lett, 3 (2003) 459-463.

[43] P.A. Hu, J. Zhang, Z.Z. Wen, C. Zhang, Network single-walled carbon nanotube biosensors for fast and highly sensitive detection of proteins, Nanotechnology, 22 (2011).

[44] X.C. Dong, D.L. Fu, Y.P. Xu, J.Q. Wei, Y.M. Shi, P. Chen, L.J. Li, Label-free electronic detection of DNA using simple double-walled carbon nanotube resistors, J Phys Chem C, 112 (2008) 9891-9895.

[45] Y. Weizmann, D.M. Chenoweth, T.M. Swager, DNA-CNT Nanowire Networks for DNA Detection, J Am Chem Soc, 133 (2011) 3238-3241.

[46] L. Li, S. Wang, T. Yang, S.M. Huang, J.C. Wang, Electrochemical growth of gold nanoparticles on horizontally aligned carbon nanotubes: A new platform for ultrasensitive DNA sensing, Biosens Bioelectron, 33 (2012) 279-283.

[47] M. Bhattacharya, S. Hong, D. Lee, T. Cui, S.M. Goyal, Carbon nanotube based sensors for the detection of viruses, Sensor Actuat B-Chem, 155 (2011) 67-74.

[48] D.J. Lee, Y. Chander, S.M. Goyal, T.H. Cui, Carbon nanotube electric immunoassay for the detection of swine influenza virus H1N1, Biosens Bioelectron, 26 (2011) 3482-3487.

[49] H.S. Mandal, Z.D. Su, A. Ward, X.W. Tang, Carbon Nanotube Thin Film Biosensors for Sensitive and Reproducible Whole Virus Detection, Theranostics, 2 (2012) 251-257.

[50] S. Liu, Q. Shen, Y. Cao, L. Gan, Z.X. Wang, M.L. Steigerwald, X.F. Guo, Chemical functionalization of single-walled carbon nanotube field-effect transistors as switches and sensors, Coordin Chem Rev, 254 (2010) 1101-1116.

[51] A. Salehi-Khojin, F. Khalili-Araghi, M.A. Kuroda, K.Y. Lin, J.P. Leburton, R.I. Masel, On the Sensing Mechanism in Carbon Nanotube Chemiresistors, Acs Nano, 5 (2011) 153-158.

[52] X.F. Guo, Single-Molecule Electrical Biosensors Based on Single-Walled Carbon Nanotubes, Adv Mater, 25 (2013) 3397-3408.

[53] S. Sorgenfrei, C.Y. Chiu, M. Johnston, C. Nuckolls, K.L. Shepard, Debye Screening in Single-Molecule Carbon Nanotube Field-Effect Sensors, Nano Lett, 11 (2011) 3739-3743.

[54] A.H. Castro Neto, F. Guinea, N.M.R. Peres, K.S. Novoselov, A.K. Geim, The electronic properties of graphene, Rev Mod Phys, 81 (2009) 109-162.

[55] R. Rao, R. Podila, R. Tsuchikawa, J. Katoch, D. Tishler, A.M. Rao, M. Ishigami, Effects of Layer Stacking on the Combination Raman Modes in Graphene, Acs Nano, 5 (2011) 1594-1599.

[56] R. Podila, R. Rao, R. Tsuchikawa, M. Ishigami, A.M. Rao, Raman Spectroscopy of Folded and Scrolled Graphene, Acs Nano, 6 (2012) 5784-5790.

[57] X.S. Li, W.W. Cai, J.H. An, S. Kim, J. Nah, D.X. Yang, R. Piner, A. Velamakanni, I. Jung, E. Tutuc, S.K. Banerjee, L. Colombo, R.S. Ruoff, Large-Area Synthesis of High-Quality and Uniform Graphene Films on Copper Foils, Science, 324 (2009) 1312-1314.

[58] C. Mattevi, H. Kim, M. Chhowalla, A review of chemical vapour deposition of graphene on copper, J Mater Chem, 21 (2011) 3324-3334.

[59] Y. Zhang, L.Y. Zhang, C.W. Zhou, Review of Chemical Vapor Deposition of Graphene and Related Applications, Accounts Chem Res, 46 (2013) 2329-2339.

[60] J. Kong, H.T. Soh, A.M. Cassell, C.F. Quate, H.J. Dai, Synthesis of individual single-walled carbon nanotubes on patterned silicon wafers, Nature, 395 (1998) 878-881.

[61] L.M. Huang, B. White, M.Y. Sfeir, M.Y. Huang, H.X. Huang, S. Wind, J. Hone, S. O'Brien, Cobalt ultrathin film catalyzed ethanol chemical vapor deposition of single-walled carbon nanotubes, J Phys Chem B, 110 (2006) 11103-11109.

[62] S.M. Huang, M. Woodson, R. Smalley, J. Liu, Growth mechanism of oriented long single walled carbon nanotubes using "fast-heating" chemical vapor deposition process, Nano Lett, 4 (2004) 1025-1028.

[63] L.M. Huang, X.D. Cui, B. White, S.P. O'Brien, Long and oriented single-walled carbon nanotubes grown by ethanol chemical vapor deposition, J Phys Chem B, 108 (2004) 16451-16456.

[64] D.E. Resasco, W.E. Alvarez, F. Pompeo, L. Balzano, J.E. Herrera, B. Kitiyanan, A. Borgna, A scalable process for production of single-walled carbon nanotubes (SWNTs) by catalytic disproportionation of CO on a solid catalyst, J Nanopart Res, 4 (2002) 131-136.

[65] V.M. Irurzun, Y.Q. Tan, D.E. Resasco, Sol-Gel Synthesis and Characterization of Co-Mo/Silica Catalysts for Single-Walled Carbon Nanotube Production, Chem Mater, 21 (2009) 2238-2246.

[66] A.C. Ferrari, J.C. Meyer, V. Scardaci, C. Casiraghi, M. Lazzeri, F. Mauri, S. Piscanec, D. Jiang, K.S. Novoselov, S. Roth, A.K. Geim, Raman spectrum of graphene and graphene layers, Phys Rev Lett, 97 (2006).

[67] M.Y. Sfeir, F. Wang, L.M. Huang, C.C. Chuang, J. Hone, S.P. O'Brien, T.F. Heinz, L.E. Brus, Probing electronic transitions in individual carbon nanotubes by Rayleigh scattering, Science, 306 (2004) 1540-1543.

[68] M.Y. Sfeir, T. Beetz, F. Wang, L.M. Huang, X.M.H. Huang, M.Y. Huang, J. Hone, S. O'Brien, J.A. Misewich, T.F. Heinz, L.J. Wu, Y.M. Zhu, L.E. Brus, Optical spectroscopy of individual single-walled carbon nanotubes of defined chiral structure, Science, 312 (2006) 554-556.

[69] H. Kataura, Y. Kumazawa, Y. Maniwa, I. Umezu, S. Suzuki, Y. Ohtsuka, Y. Achiba, Optical properties of single-wall carbon nanotubes, Synthetic Met, 103 (1999) 2555-2558.

[70] R.C. Neville, C.A. Mead, Hoeneise.B, Permittivity of Strontium-Titanate, J Appl Phys, 43 (1972) 2124-&.

[71] G.G. Chen, T.M. Paronyan, E.M. Pigos, A.R. Harutyunyan, Enhanced gas sensing in pristine carbon nanotubes under continuous ultraviolet light illumination, Sci Rep-Uk, 2 (2012).

[72] F. Leonard, A.A. Talin, Electrical contacts to one- and two-dimensional nanomaterials, Nat Nanotechnol, 6 (2011) 773-783.

[73] A.D. Franklin, Z.H. Chen, Length scaling of carbon nanotube transistors, Nat Nanotechnol, 5 (2010) 858-862.

[74] S. Heinze, J. Tersoff, R. Martel, V. Derycke, J. Appenzeller, P. Avouris, Carbon nanotubes as Schottky barrier transistors, Phys Rev Lett, 89 (2002).

[75] Z.H. Chen, J. Appenzeller, J. Knoch, Y.M. Lin, P. Avouris, The role of metal-nanotube contact in the performance of carbon nanotube field-effect transistors, Nano Lett, 5 (2005) 1497-1502.

[76] M.H. Yang, K.B.K. Teo, W.I. Milne, D.G. Hasko, Carbon nanotube Schottky diode and directionally dependent field-effect transistor using asymmetrical contacts, Appl Phys Lett, 87 (2005).

[77] M. Shiraishi, M. Ata, Work function of carbon nanotubes, Carbon, 39 (2001) 1913-1917.

[78] Z. Xu, X.D. Bai, E.G. Wang, Z.L. Wang, Field emission of individual carbon nanotube with in situ tip image and real work function, Appl Phys Lett, 87 (2005).

[79] P. Liu, Q. Sun, F. Zhu, K. Liu, K. Jiang, L. Liu, Q. Li, S. Fan, Measuring the work function of carbon nanotubes with thermionic method, Nano Lett, 8 (2008) 647-651.

[80] J.H. Chen, C. Jang, S.D. Xiao, M. Ishigami, M.S. Fuhrer, Intrinsic and extrinsic performance limits of graphene devices on SiO2, Nat Nanotechnol, 3 (2008) 206-209.

[81] K.I. Bolotin, K.J. Sikes, Z. Jiang, M. Klima, G. Fudenberg, J. Hone, P. Kim, H.L. Stormer, Ultrahigh electron mobility in suspended graphene, Solid State Commun, 146 (2008) 351-355.

[82] J.M. Xue, J. Sanchez-Yamagishi, D. Bulmash, P. Jacquod, A. Deshpande, K. Watanabe, T. Taniguchi, P. Jarillo-Herrero, B.J. Leroy, Scanning tunnelling microscopy and spectroscopy of ultra-flat graphene on hexagonal boron nitride, Nat Mater, 10 (2011) 282-285.

[83] C.R. Dean, A.F. Young, I. Meric, C. Lee, L. Wang, S. Sorgenfrei, K. Watanabe, T. Taniguchi, P. Kim, K.L. Shepard, J. Hone, Boron nitride substrates for high-quality graphene electronics, Nat Nanotechnol, 5 (2010) 722-726.

[84] E.S. Snow, J.P. Novak, P.M. Campbell, D. Park, Random networks of carbon nanotubes as an electronic material, Appl Phys Lett, 82 (2003) 2145-2147.

[85] R. Martel, V. Derycke, C. Lavoie, J. Appenzeller, K.K. Chan, J. Tersoff, P. Avouris, Ambipolar electrical transport in semiconducting single-wall carbon nanotubes, Phys Rev Lett, 87 (2001).

[86] L. Hu, D.S. Hecht, G. Gruner, Percolation in transparent and conducting carbon nanotube networks, Nano Lett, 4 (2004) 2513-2517.

[87] V. Derycke, R. Martel, J. Appenzeller, P. Avouris, Controlling doping and carrier injection in carbon nanotube transistors, Appl Phys Lett, 80 (2002) 2773-2775.

[88] I. Dumitrescu, J.P. Edgeworth, P.R. Unwin, J.V. Macpherson, Ultrathin Carbon Nanotube Mat Electrodes for Enhanced Amperometric Detection, Adv Mater, 21 (2009) 3105-+.

[89] M.S. Purewal, B.H. Hong, A. Ravi, B. Chandra, J. Hone, P. Kim, Scaling of resistance and electron mean free path of single-walled carbon nanotubes, Phys Rev Lett, 98 (2007).

[90] J. Kong, E. Yenilmez, T.W. Tombler, W. Kim, H.J. Dai, R.B. Laughlin, L. Liu, C.S. Jayanthi, S.Y. Wu, Quantum interference and ballistic transmission in nanotube electron waveguides, Phys Rev Lett, 87 (2001) art. no.-106801.

[91] M.S. Fuhrer, J. Nygard, L. Shih, M. Forero, Y.G. Yoon, M.S.C. Mazzoni, H.J. Choi, J. Ihm, S.G. Louie, A. Zettl, P.L. McEuen, Crossed nanotube junctions, Science, 288 (2000) 494-497.

[92] P.L. McEuen, M. Bockrath, D.H. Cobden, Y.G. Yoon, S.G. Louie, Disorder, pseudospins, and backscattering in carbon nanotubes, Phys Rev Lett, 83 (1999) 5098-5101.

[93] M.S. Fuhrer, B.M. Kim, T. Durkop, T. Brintlinger, High-mobility nanotube transistor memory, Nano Lett, 2 (2002) 755-759.

[94] Y.M. Shi, H. Tantang, C.W. Lee, C.H. Weng, X.C. Dong, L.J. Li, P. Chen, Effects of substrates on photocurrents from photosensitive polymer coated carbon nanotube networks, Appl Phys Lett, 92 (2008).

[95] D.S. Hecht, R.J.A. Ramirez, M. Briman, E. Artukovic, K.S. Chichak, J.F. Stoddart, G. Gruner, Bioinspired detection of light using a porphyrin-sensitized single-wall nanotube field effect transistor, Nano Lett, 6 (2006) 2031-2036.

[96] J. Borghetti, V. Derycke, S. Lenfant, P. Chenevier, A. Filoramo, M. Goffman, D. Vuillaume, J.P. Bourgoin, Optoelectronic switch and memory devices based on polymer-functionalized carbon nanotube transistors, Adv Mater, 18 (2006) 2535-+.

[97] A. Star, Y. Lu, K. Bradley, G. Gruner, Nanotube optoelectronic memory devices, Nano Lett, 4 (2004) 1587-1591.

[98] Y.M. Shi, X.C. Dong, H. Tantang, C.H. Weng, F.M. Chen, C.W. Lee, K.K. Zhang, Y. Chen, J.L. Wang, L.J. Li, Photoconductivity from Carbon Nanotube Transistors Activated by Photosensitive Polymers, J Phys Chem C, 112 (2008) 18201-18206.

[99] T. Ando, T. Nakanishi, Impurity scattering in carbon nanotubes - Absence of back scattering, J Phys Soc Jpn, 67 (1998) 1704-1713.

[100] T. Nakanishi, T. Ando, Numerical study of impurity scattering in carbon nanotubes, J Phys Soc Jpn, 68 (1999) 561-566.

[101] J. Renard, M.B. Lundeberg, J.A. Folk, Y. Pennec, Real-Time Imaging of K Atoms on Graphite: Interactions and Diffusion, Phys Rev Lett, 106 (2011).

[102] J. Kong, C.W. Zhou, E. Yenilmez, H.J. Dai, Alkaline metal-doped n-type semiconducting nanotubes as quantum dots, Appl Phys Lett, 77 (2000) 3977-3979.

[103] M. Bockrath, J. Hone, A. Zettl, P.L. McEuen, A.G. Rinzler, R.E. Smalley, Chemical doping of individual semiconducting carbon-nanotube ropes, Phys Rev B, 61 (2000) 10606-10608.

[104] C.L. Kane, E.J. Mele, Size, shape, and low energy electronic structure of carbon nanotubes, Phys Rev Lett, 78 (1997) 1932-1935.

[105] V.V. Deshpande, B. Chandra, R. Caldwell, D.S. Novikov, J. Hone, M. Bockrath, Mott Insulating State in Ultraclean Carbon Nanotubes, Science, 323 (2009) 106-110.

[106] M.R. Amer, A. Bushmaker, S.B. Cronin, The Influence of Substrate in Determining the Band Gap of Metallic Carbon Nanotubes, Nano Lett, 12 (2012) 4843-4847.